Development of Hybrid Electromagnetic Dampers for Vehicle Suspension Systems

by

Babak Ebrahimi

A thesis

presented to the University of Waterloo

in fulfillment of the

thesis requirement for the degree of

Doctor of Philosophy

in

Mechanical Engineering

Waterloo, Ontario, Canada, 2009

AUTHOR'S DECLARATION

I hereby declare that I am the sole author of this thesis. This is a true copy of the thesis, including any required final revisions, as accepted by my examiners.

I understand that my thesis may be made electronically available to the public.

Babak Ebrahimi

Abstract

Vehicle suspension systems have been extensively explored in the past decades, contributing to ride comfort, handling and safety improvements. The new generation of powertrain and propulsion systems, as a new trend in modern vehicles, poses significant challenges to suspension system design. Consequently, novel suspension concepts are required, not only to improve the vehicle's dynamic performance, but also to enhance the fuel economy by utilizing regeneration functions. However, the development of new-generation suspension systems necessitates advanced suspension components, such as springs and dampers. This Ph.D. thesis, on the development of hybrid electromagnetic dampers is an Ontario Centres of Excellence (OCE) collaborative project sponsored by Mechworks Systems Inc. The ultimate goal of this project is to conduct feasibility study of the development of electromagnetic dampers for automotive suspension system applications.

With new improvements in power electronics and magnetic materials, electromagnetic dampers are forging the way as a new technology in vibration isolation systems such as vehicle suspension systems. The use of electromagnetic dampers in active vehicle suspension systems has drawn considerable attention in the recent years, attributed to the fact that active suspension systems have superior performance in terms of ride comfort and road-handling performances compared to their passive and semi-active counterparts in automotive applications. As a response to the expanding demand for superior vehicle suspension systems, this thesis describes the design and development of a new electromagnetic damper as a customized linear permanent magnet actuator to be used in active suspension systems. The proposed electromagnetic damper has energy harvesting capability. Unlike commercial passive/semi-active dampers that convert the vibration kinetic energy into heat, the dissipated energy in electromagnetic dampers can be regenerated as useful electrical energy. Electromagnetic dampers are used in active suspension systems, where the damping coefficient is controlled rapidly and reliably through electrical manipulations. Although demonstrating superb performance, active suspensions still have some issues that must be overcome. They have high energy consumption, weight, and cost, and are not fail-safe in case of a power break-down. Since the introduction of the electromagnetic dampers, the challenge was to address these drawbacks.

Hybrid electromagnetic dampers, which are proposed in this Ph.D. thesis, are potential solutions to high weight, high cost, and fail-safety issues of an active suspension system. The hybrid electromagnetic damper utilizes the high performance of an active electromagnetic damper with the

reliability of passive dampers in a single package, offering a fail-safe damper while decreasing weight and cost. Two hybrid damper designs are proposed in this thesis. The first one operates based on hydraulic damping as a source of passive damping, while the second design employs the eddy current damping effect to provide the passive damping part of the system. It is demonstrated that the introduction of the passive damping can reduce power consumption and weight in an active automotive suspension system.

The ultimate objective of this thesis is to employ existing suspension system and damper design knowledge together with new ideas from electromagnetic theories to develop new electromagnetic dampers. At the same time, the development of eddy current dampers, as a potential source for passive damping element in the final hybrid design, is considered and thoroughly studied. For the very first time, the eddy current damping effect is introduced for the automotive suspension applications. The eddy current passive damper, as a stand-alone unit, is designed, modeled, fabricated and successfully tested. The feasibility of using passive eddy current dampers for automotive suspension applications is also studied. The structure of new passive eddy current dampers is straightforward, requiring no external power supply or any other electronic devices. Proposed novel eddy current dampers are oil-free and non-contact, offering high reliability and durability with their simplified design.

To achieve the defined goals, analytical modeling, numerical simulations, and lab-based experiments are conducted. A number of experimental test-beds are prepared for various experimental analyses on the fabricated prototypes as well as off-the-shelf dampers. Various prototypes, such as eddy current and electromagnetic dampers, are manufactured, and tested in frequency/time domains for verification of the derived analytical and numerical models, and for proof of concept. In addition, fluid and heat transfer analyses are done during the process of the feasibility study to ensure the durability and practical viability of the proposed hybrid electromagnetic dampers.

The presented study is only a small portion of the growing research in this area, and it is hoped that the results obtained here will lead to the realization of a safer and more superior automotive suspension system.

Acknowledgements

I would like to thank my supervisors, Professor Behrad Khamesee and Professor Farid Golnaraghi for all their guidance, support, and constant encouragement during my research.

I would also like to express my gratitude to the examining committee members Professor Steve Lambert, Professor Mehrdad Kazerani, and Professor William Owen, whose comments and suggestions were extremely helpful in improving my manuscript. Special thanks to Professor Jean Zu, from the University of Toronto, for serving as my external referee.

Over the last three years, I have been privileged to work with and learn from my colleagues, Siamak Arzanpour, Ornag Vahid, Nima Eslaminasab, Shahab Ghafari, Hamidreza Bolandhemmat, Mohammad Biglarbegian, Caglar Elbuken, Saleh Tanabdeh, Amir Rouzrokh, Kiarash Narimani, Azad Qazi Zade, Mohsen Azimi, and Saman Hoseini. Especially, I would like to thank Anahita Ghazanfari, for her support, patience, and dedication during past years.

I wish to express thanks to all my family members, Laleh Ebrahimi, Golnaz Ebrahimi, Mehdi Mirsaeidi, and Ali Shahrokni for their constant support and love.

I am particularly indebted to my good friends Ehsan Shameli and Roozbeh Borjian for their support and true friendship.

Dedication

For Zahra Shariat and Reza Ebrahimi, my dear parents, whose steadfast support and unconditional love fuelled my drive to the end

Table of Contents

List of Figures

List of Tables

Nomenclature

A_g	lateral area of the pole
A_m	cross section area of the magnet
A_P	cross section area of the piston
A_R	cross section area of the rod
$\boldsymbol{B}$	magnetic flux density
B_g	air-gap flux density
B_r	radial flux density
B_z	axial flux density
B_{rem}	remanent flux density
C	damping coefficient
C_C	damping coefficient in compression
C_D	average damping coefficient
C_E	damping coefficient in extension
C_{FC}, C_{FE} , C_{PC} , C_{PE}	discharge coefficient
c_{max}	maximum damping force
c_p	passive damping coefficient
c_{sky}	ideal skyhook damping coefficient
D_h	hydraulic diameter
d	rod diameter
d_s	depth
E	total induced electromotive force
E_{trans}	transformer electromotive force
$E_{motional}$	motional electromotive force
$E(k)$	elliptic integral of the first kind
$\boldsymbol{F}$, F	force
F_a	active force
F_c	critical buckling force
F_d	damping force
F_f	friction force
F_H	Total hybrid damping force
F_S	static force
f	friction factor
Gr	Grashof number
g	gap between two magnets
H_c	coercive magnetic field

H_{ext}	external magnetization
h_F	forced-convection heat transfer coefficient
h_N	natural-convection heat transfer coefficient
I	electrical current
$\hat{I}$	peak current
I_m	moment of inertia
$\boldsymbol{J}$,J	current density
$\boldsymbol{J}_m$	equivalent volume current density
$\boldsymbol{j}_m$	equivalent surface current density
J_s	current density at the surface
K	thermal conductivity
K_f	thrust constant
K_{sp}	electric loading
$K(k)$	elliptic integral of the second kind
k	total suspension stiffness
k_a	air's thermal conductivity
k_c	conductor's thermal conductivity
k_m	mover's thermal conductivity
k_s	suspension stiffness
k_u	tire stiffness
L	inductance
L_k	free buckling length
l_m	magnets length
$\boldsymbol{M}$, M	magnetization
M_r	remanent magnetization
m	mass
m_s	sprung mass
m_u	unsprung mass
N	number of turns in a coil
N_c	number of coils
Nu	Nusselt number
n	factor of safety
$\hat{\boldsymbol{n}}$	unit surface normal
P	power loss
P_C	compression chamber pressure
P_E	extension chamber pressure
P_H	hydraulic pressure
P_R	foot chamber pressure

P_r	Prandtl number
p	number of poles
Q_{FC}, Q_{FE} , Q_{PC} , Q_{PE}	volumetric flow rate
R	resistance
Re	Reynolds number
R_m	permanent magnet radius
R_{gap}	equivalent reluctance of the air-gap
R_{mag}	equivalent reluctance of the magnet
r	element length
r_{in}	conductor inside radius
r_{out}	conductor outside radius
S	tensile strength
S_{cu}	stator coil's cross section area
S_e	endurance limit
s	rod radius
s_c	air-gap thickness
T	period
T_s	conductor's surface temperature
T_m	magnet temperature
t	time
$\boldsymbol{v}$	velocity
V_E	extension velocity
V_C	compression velocity
w_c	coil width
x_r	relative displacement
x_s	sprung mass displacement
$\dot{x}_s$	sprung mass velocity
$\ddot{x}_s$	sprung mass acceleration
Y	base displacement amplitude
y	base displacement
$\dot{y}$	base velocity
$\hat{\boldsymbol{z}}$	longitudinal unit vector
z	element length
z_d	distance between two current carrying loops
β	volume expansion coefficient
Γ	conductor volume
γ	displacement transmissibility
δ, l_c	conductor thickness

δ_p	depth of penetration
δ_w	stator core thickness
δ_c	cylinder thickness
ζ	damping ratio
η	acceleration transmissibility
θ	angle and phase
θ_w	winding temperature rise
λ	relative displacement transmissibility
λ_c	winding factor
λ_{PM}	flux linkage due to a magnet
μ	fluid viscosity
μ_a	absolute permeability
μ_o	permeability of free space
μ_r	relative permeability
μ_{rec}	recoil permeability
ρ	fluid density
σ	conductivity
σ_H	hoop stress
τ	pole pitch
τ_e	electrical time constant
τ_m	magnet thickness
τ_s	coil pitch
υ	kinematic viscosity
φ	phase angle
$\hat{\boldsymbol{\varphi}}$	tangential unit vector
ϕ_g	magnetic flux in the gap
ϕ_m	magnetic flux due to the magnets
ω	frequency
ω_n	natural frequency

Chapter 1

Introduction

Suspension systems, in the automotive application context, have been designed to maintain contact between a vehicle's tires and the road, and to isolate the frame of the vehicle from road disturbances. Dampers, or so-called shock absorbers, as the undeniable heart of suspension systems, reduce the effect of a sudden bump by smoothing out the shock. In most shock absorbers, the energy is converted into heat via viscous fluid. In hydraulic cylinders, the hydraulic fluid is heated up. In air cylinders, the hot air is emitted into the atmosphere. There are several common approaches for shock absorption, including material hysteresis, dry friction, fluid friction, compression of gas, and eddy currents.

In the past few years, improvements in power electronics and magnetic materials have resulted in significant improvements in electro-mechanical devices, reducing their volume, weight, and cost, and improving their overall efficiency and reliability. These developments justify an analysis and implementation of electromagnetic devices in suspension systems. In most dampers, the energy is converted into heat and dissipated without being used; in electromagnetic dampers, the dissipated energy can be stored as electrical energy and used later. The use of electromagnetic dampers in suspension systems has several benefits compared to hydraulic, pneumatic, or other mechanical dampers. Electromagnetic dampers can function simultaneously as sensors and actuators. The spring effect can be added to the system by means of electromagnets, powered by Permanent Magnets (PMs). Moreover, electromagnetic dampers can work under very low static friction. Here, the damping coefficient is controlled rapidly and reliably through electrical manipulations.

Although active suspensions have superb performance, they have high energy consumption, are not fail-safe in case of power failure, and are heavy and expensive compared to conventional variable dampers, using other technologies such as electromagnetic-valve and Magneto-Rheological (MR) fluid dampers. Hybrid electromagnetic dampers, which are proposed in this Ph.D. thesis, are potential solutions to the high weight, high cost, and fail-safety issues in an active suspension system. The hybrid electromagnetic damper combines the performance and controllability of an active

electromagnetic damper with the reliability of passive dampers in a single package, saving weight and cost, and making the damper fail-safe in case of power failure. Since the active electromagnetic damper utilizes magnetic components, one potential design for supplying the passive damping effect is the eddy current damping phenomenon.

Eddy currents are induced in a conductor either by the movement of the conductor in a static field or a change in the strength of the magnetic field. The generated eddy currents create electromagnets with magnetic fields that oppose the change in an external magnetic field, causing a repulsive force proportional to the relative velocity of the field and conductor. Consequently, the eddy current damping device acts like a viscous damper, causing the vibration energy of the moving mass to dissipate through resistive/Joule heating, generated in the conducting component. The use of the eddy current damping phenomenon is appealing, because the damper structure is simple and requires neither external power supply nor electronic devices; in addition, no fluid is involved in the damper, and the moving parts of the damper have no mechanical contact. The eddy current damping phenomenon is discussed in more detail in Chapter 3.

This Introduction chapter outlines three main subject matters. First, the vehicle suspension systems are introduced, focusing on the different suspension system types and conventional control strategies involved in these systems. Second, different vehicle suspension models as well as the vehicle suspension performance indexes are discussed. Finally, dampers as the main focus in this thesis are considered, the conventional and the novel proposed technologies are introduced, and the literature is reviewed. The Introduction chapter is finalized with a brief summary of motivation, objectives, and the thesis outline.

1.1 Vehicle Suspension System

The primary function of the vehicle suspension system is to provide a comfortable ride, through isolation of the vehicle body from road irregularities, and enhance the ride handling by producing a continuous road-wheel contact.

According to the level of controllability, suspension systems are classified as passive, active, or semi-active. Aside from the inherent advantages and disadvantages of each type, all of them utilize the spring and damper units. It is verified that the passive and semi-active suspension systems cannot provide the above-mentioned requirements satisfactorily, because of the contrasting nature of these

requirements. Active suspension in its various forms offers a means to relax those compromises (Wendel *et al.*, 1991). In active suspension systems, actuators, which are operating by external power, are used to generate the necessary force to suppress the vibrations. However, active suspensions have drawbacks regarding their size, weight, power consumption, and fail-safety issues.

Semi-active suspensions also contain spring and damping elements. The properties of these elements can be controlled externally by supplying a signal or other types of external power to the system. In addition, these characteristics can be changed so that different levels of the resisting forces are produced, according to a low-power control signal. These systems partially benefit from the advantages of active systems with the reliability of passive systems. If the control system fails, the semi-active system continues to operate in the passive mode.

There are several qualitative measures that must be considered by the suspension system designer in order to achieve the desired performance, including: ride comfort (corresponds to the acceleration felt by the passenger), road-handling, the relative motion between the vehicle body and wheels, and the body motions during critical maneuvers such as braking and cornering (Biglarbegian *et al.*, 2008). The vehicle suspension performance indexes are discussed in Section 1.2.2 in greater detail.

1.1.1 Passive Suspension Systems

Passive suspension systems are the most common systems that are used in commercial passenger cars. They are composed of conventional springs, and single or twin-tube oil dampers with constant damping properties. The designer pre-sets the fix damping properties to achieve optimum performance for the intended application. The disadvantage of passive suspension systems with constant damping characteristics is that setting the design parameters is a compromise between the ride quality and handling. Generally, softer dampers provide a more comfortable ride, while stiffer ones provide better stability and thus better road-handling. Passive suspension systems are tuned according to the expected operating conditions, but a compromise is always made between designing for the two opposing goals. Therefore, the performance in each area is limited according to this compromise (Gillespie, 2006). However, traditional passive suspension systems are low cost, and relatively simple to manufacture.

1.1.2 Semi-active Suspension Systems

Since first proposed by Crosby and Karnopp (1973), semi-active suspension systems continue to gain popularity in vehicle suspension system applications, due to their advantageous characteristics over passive suspension systems. Semi-active (also known as adaptive-passive) suspension systems are essentially passive systems in which the damping properties can be adjusted to some extent. Thus, semi-active suspension systems extend the possible range of damping characteristics obtainable from a passive damper (Carter, 1998), (Barak, 1992), and (Koo, *et al.*, 2004). The damping characteristics of a semi-active damper can be adjusted through applying a low-power signal. Semi-active systems are a compromise between the active and passive systems (Alanoly *et al.*, 1986). They are commercialized recently by means of either a solenoid valve as an adjustable orifice, or MR-fluid dampers, both of which are very expensive. Leading automotive manufacturers such as GM and Volvo have started the implementation of these semi-active suspension systems for their high-end automobiles. However, there exist many challenges that must be overcome for these technologies. The MR dampers have still some crucial issues, such as MR degradation with time, temperature sensitivity, and sealing problems.

1.1.3 Active Suspension Systems

Active suspension system refers to a system that uses an active power source to actuate the suspension links by extending or contracting them as required (Gillespie, 2006). The main challenge in the automobile suspension system design is the trade-off between the conflicting requirements of ride-comfort and handling. In the past few decades, due to advances in sensors/actuators technologies, active suspension systems have emerged as an active research field to address those compromises.

In an active suspension, controlled forces are introduced to the suspension by means of hydraulic or electric actuators, between the sprung and unsprung-mass of the wheel assemblies (Brown, 2005). Karnopp (1983) studied the effect of adding an active damping force to the suspension system. Milliken (1988) developed the first fully active suspension to be used in a suspensions system application. A variable force is provided by the active suspension at each wheel to continuously modify the ride and handling characteristics. The key difference between semi-active and active suspension systems is that the latter applies an external force to the vehicle body either in an upward or downward direction, regardless of the absolute vehicle body velocity. Active suspension overcomes the compromises required in tuning passive dampers. Sensors, as essential elements of an

active suspension, are used to measure the suspension movements at different points. Although active suspensions have superb performance, the practical implementation of active suspension in vehicles has been limited due to their high weight, cost, power consumption, and reduced reliability that are not justified by the limited incremental benefit to the passenger (Deo, 2007). Most of the suspension systems that are proposed and implemented in vehicle suspension systems are based on hydraulic or pneumatic devices.

1.2 Simplified Vehicle Models and Performance Indexes

It is possible to study the fundamental concepts of vehicle dynamics based on simplified vehicle models. The choice of the suspension system models depends on the vibration mode and the simplicity of the analysis involved. Basic vehicle models that have been reviewed in the literature are the quarter-car one-degree-of-freedom (1DOF) model to study the bounce mode, the quarter-car 2DOF model to study the wheel-hop as well as the bounce mode, the half-car 4DOF model for bounce and pitch modes, and the full-car 7DOF model for bounce, pitch and roll modes (Deo. 2007). The most general and constructive automotive suspension system design information derives from a single-wheel station, quarter-car representation (Sharp and Crolla, 1987). Quarter-car models are perfect for a vehicle with a longitudinally independent suspension and a symmetric mass distribution in the vehicle body, where the front and rear suspension is decoupled (Mitschke, 1961). This model is a good approximation of a real suspension system only for long wavelength and low frequency inputs (Sharp and Hassan, 1984). It does not represent the geometric effects of having four wheels, and does not incorporate the longitudinal interconnection. However, it contains the most fundamental features of the real suspension system, such as suspension system forces, which are properly applied between a vehicle's wheels and body. It is the simplest model which has these features, retaining advantages over more complex models in terms of having fewer performance parameters. There is only a single input involved in a quarter-car model that simplifies the performance computation and the application of optimal control strategies. In addition, the quarter-car model offers a comprehensive model for understanding the correlation between performance and design parameters. The quarter-car model with realistic road input spectra is not sensitive to the body-to-wheel mass, and tire stiffness-to-weight supported ratios (Ryba, 1974) and (Sharp and Hassan, 1984), provided that these are reasonably selected.

Bernard *et al.* (1991) proposed a roll-over model to predict the vehicle roll characteristics. However, its application is limited because the model cannot predict the vertical motion of the vehicle (Eslaminasab, 2008). In order to consider the rollover as well as the vertical motions, more complex models are proposed, such as a 4DOF half-car vertical dynamic model that has already been developed and used in the numerous research works (Hrovat, 1997) and (Kyongsu *et al.*, 2007).

1.2.1 One and Two DOF Quarter-Car Models

The dynamic behavior of vehicle vertical isolation properties can be represented and analyzed by one or two DOF quarter-car models, as shown in Fig. 1-1 (Eslaminasab, 2008).

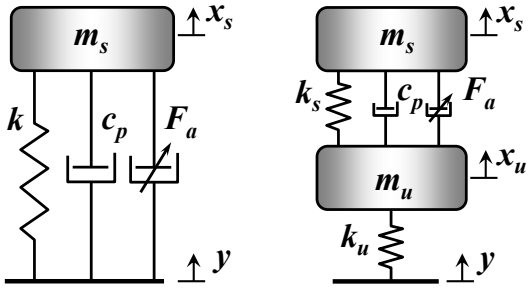

a) 1DOF quarter-car model b) 2DOF quarter-car model

Fig. 1-1 One and two DOF quarter-car models.

In this model representation, m_s is a quarter of the whole vehicle body mass (*sprung-mass*), while the wheel mass is represented by m_u and called the *unsprung-mass*. k_s and k_u represent the suspension and tire stiffness, respectively. The governing equation of motion for the 1DOF system in Fig. 1-1(a) is

$$m_s\ddot{x}_s = -k(x_s - y) - c_p(\dot{x}_s - \dot{y}) - F_a, \tag{1-1}$$

where k is the total suspension stiffness, and F_a is the actuator active force in case of the active suspension system, and is set by the control strategy. c_p is the passive damping coefficient in the system. In addition, x_s and y are the mass movements and the road disturbances. Considering the road disturbance as a sinusoidal function ($y = Y\,sin(\omega t)$), the equation of motion (1-1) is expressed as (Eslaminasab, 2008)

$$\ddot{x}_r + 2\zeta\omega_n\dot{x}_r + \omega_n^2 x_r = Y\omega^2 \sin(\omega t) - F_a / m_s, \tag{1-2}$$

where the parameters are damping ratio (ζ), natural frequency (ω_n), and the relative displacement (x_r) are defined as

$$\zeta = \frac{c}{2\sqrt{km_s}}, \quad \omega_n = \sqrt{\frac{k}{m_s}}, \quad x_r = x_s - y \tag{1-3}$$

On the other hand, the governing equation for a 2DOF suspension system in Fig. 1-1(b) is

$$\begin{aligned} m_s\ddot{x}_s &= -k_s(x_s - x_u) - c_p(\dot{x}_s - \dot{x}_u) - F_a, \\ m_u\ddot{x}_u &= k_s(x_s - x_u) - k_u(x_u - y) + c_p(\dot{x}_s - \dot{x}_u) + F_a. \end{aligned} \tag{1-4}$$

As a common practice, the 1DOF quarter-car model has been vastly used as a powerful and simple method to address the vertical motion of vehicles, such as in (Karnopp *et al.*, 1969), (Karnopp *et al.*, 1974), (Rakheja *et al.*, 1985), (Alanoly *et al.*, 1986), (Shen, 2005), and (Eslaminasab, 2008). As one of the subjects in this study is to adopt a simple model to analyze the damping characteristics correlation with the suspension performance, a 1DOF quarter-car model is primarily adopted in this thesis.

1.2.2 Vehicle Suspension Performance Indexes

There are a number of indexes in the suspension control analysis addressing the performance of the suspension system. Ride comfort and road-handling are among the most commonly used indexes in a vehicle suspension context. Much research has been conducted to find factors that affect ride comfort (Pollard and Simons, 1984), (Demic *et al.*, 2002), and (Ihsan *et al.*, 2008). The former, for example, investigated human behavior under random vibrations, and demonstrates that humans are normally very sensitive to frequencies below 1 Hz. Aspinall and Oliver (1964) suggested the Root Mean Square (RMS) of the vehicle body vertical acceleration at the passenger location is a good measure of discomfort.

The acceleration transmissibility, η, is defined as the principal source of discomfort for the driver (Anon, 1997), and (Griffin, 1998). The acceleration (force) transmissibility η is the ratio of the maximum magnitude of mass acceleration to the input acceleration at the natural frequency. This ratio also expresses the force transmitted to the mass as a result of excitation, and it is represented by

$$\eta = \left| \frac{\max(\ddot{x}_s)}{\max(\omega_n^2 y)} \right| . \tag{1-5}$$

In the aforementioned 1DOF model with a sinusoidal base excitation, the acceleration transmissibility, η, is expressed as (Shen, 2005)

$$\eta = \frac{\omega^2 \sqrt{\omega_n^4 + (2\zeta\omega_n\omega)^2}}{\omega_n^2 \sqrt{(\omega_n^2 - \omega^2)^2 + 4\zeta^2\omega_n^2\omega^2}} . \tag{1-6}$$

On the other hand, relative displacement transmissibility, λ, is translated as the vehicle's centre of gravity height, and is considered as a proper parameter for measuring the road-handling performance (Eslaminasab, 2008). The relative displacement transmissibility is defined as the ratio of the maximum magnitude of relative mass displacement to that of the input displacement, as:

$$\lambda = \left| \frac{\max(x_r)}{\max(y)} \right| , \tag{1-7}$$

where x and y are the mass and base displacements, respectively. Again, for a 1DOF system with the sinusoidal input, the relative displacement transmissibility, λ, is expressed as (Shen, 2005)

$$\lambda = \frac{\omega^2}{\sqrt{(\omega_n^2 - \omega^2)^2 + 4\zeta^2\omega_n^2\omega^2}} . \tag{1-8}$$

It should be mentioned that for an active suspension system, additional performance indexes are defined such as actuator force levels and power consumption (Sharp and Crolla, 1987).

As mentioned already in Section 1.1.1, setting the design parameters, in a suspension system, is a compromise between ride quality and handling. To have a better understanding, a 1DOF suspension system with m_s=2 kg and k_s=4600 N/m is considered. According to (1-8), the damping ratio (ζ) should be increased to reduce the relative displacement transmissibility of the system (λ). This is also shown in Fig. 1-2(a). However, as the damping ratio increases, the acceleration transmissibility (η) decreases up to a certain frequency ($\omega = \sqrt{2}\,\omega_n$ for a 1DOF system). But, beyond this frequency, the acceleration transmissibility increases with the excitation frequency as shown in Fig. 1-2(b). As another example, for a given road roughness and vehicle speed, ride comfort can be increased by reducing stiffness and damping, while suspension deflection is exacerbated. Suspension

deflection in a quarter-car 2DOF model (Fig. 1-1(b)) is defined as (x_s-y). It should be mentioned that low stiffness results in a good comfort performance, while statically stiff systems have advantages for a good dynamic control and handling characteristics (Sharp and Crolla, 1987).

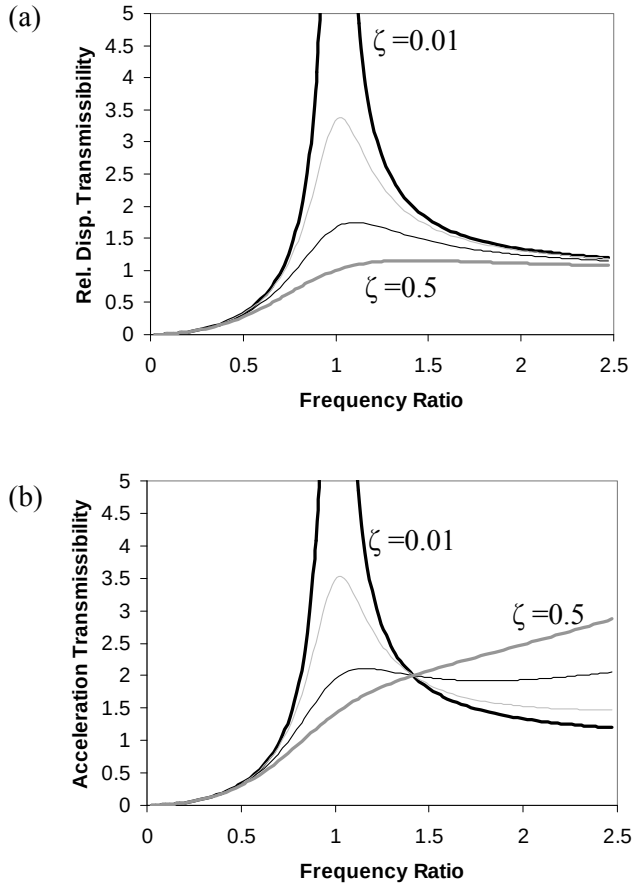

Fig. 1-2 The conflict between suspension performance indexes: (a) Relative displacement and (b) acceleration transmissibilities.

1.3 Dampers in Vehicle Suspension System

Automotive dampers commonly known as shock absorbers are used in vehicle suspension systems to isolate the vehicle chassis from unwanted vibrations due to the road disturbances, and to provide good road-handling. Arguably, the term shock absorber instead of damper is misleading, since the shocks are absorbed by deflection of tires and springs. The concept of linear damper that generates force proportional to its endings relative velocity is widely used and studied in vibration analysis. There is

no requirement that a damper must exhibit such characteristics, but a typical modern damper does so, mainly because the damper manufacturer considers this desirable to be used in a suspension system (Dixon, 1999). Dampers have been developed over the history of automotive technology from simple friction dampers to modern telescopic ones. The earliest paper appears to be that by Hadley (1928), dealing with mechanical friction dampers (Dixon, 1999). Weaver (1929) investigated damper characteristics, plotting the force-displacement curves, while three years later, James and Ullery (1932) discussed the superior performance of the hydraulic damping with a suitable force-velocity relationship, comparing it to the Coulomb friction damping. The first variable damper with solenoid valves, and Electro-Rheological (ER) fluids are tested by Hagela *et al.* (1990).

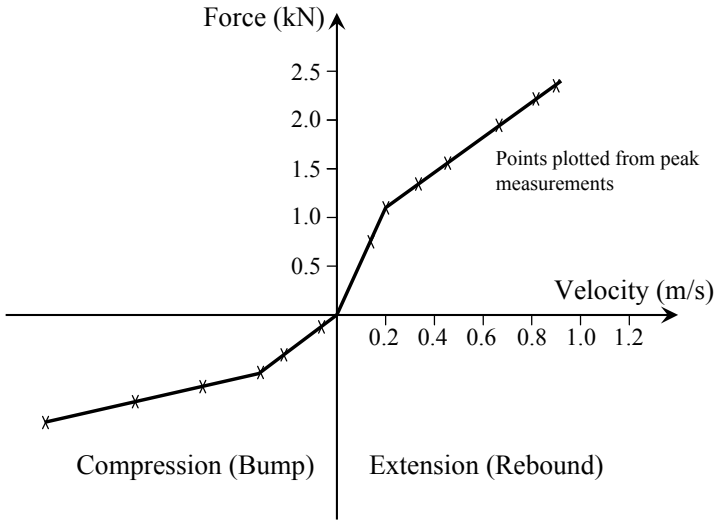

Fig. 1-3 Typical force-velocity behavior for a hydraulic passive damper.

Fig. 1-3 depicts typical force-velocity representation of a hydraulic passive damper. This graph is obtained by plotting the peak forces in stroking tests at different velocities. The damping coefficient is not constant over the working velocity range, and is defined as the curve's slope at each velocity. The asymmetry in damping performance between the extension and compression stages as well as a higher damping coefficient at lower velocities is apparent in Fig. 1-3. The effect of frequency-dependent asymmetric damping on suspension performance indexes has been thoroughly studied by (Thompson, 1996), (Dixon, 1999), and (Eslaminasab, 2008). Eslaminasab (2008) demonstrated that the damper with asymmetric damping behavior, shown in Fig. 1-3, causes a lower height for the vehicle body, and so has a positive effect on vehicle stability. Nevertheless, there is no general

standard for damper performance in the automotive suspension context, and damper design is highly influenced by the required functionality. The damper's asymmetric behavior from the design requirement perspective will be addressed in the next chapter.

In the following subsections, different commercial damper technologies such as passive (hydraulic) and semi-active, as well as proposed novel ideas, like eddy current, and hybrid dampers are introduced and the corresponding literature is reviewed.

1.3.1 Passive Hydraulic Dampers

Most conventional vehicle suspension systems utilize passive dampers to provide damping. Conventional hydraulic shock absorbers suppress vehicle frame vibration by a piston moving through oil. Holes in the piston are covered by valves, which resist the flow of the oil through the holes in a controlled manner to produce the damping effect.

There are basically two categories of passive dampers as shown in Fig. 1-4, mono-tube and twin-tube. Unlike the twin-tube damper, a mono-tube damper (Fig. 1-4(a)) composed of one cylinder filled with oil through which a piston with an orifice is moving. Passing the fluid through the orifice causes a resultant damping force due to the pressure drop between the compression and extension chambers. The presence of the gas chamber allows the volume of the piston rod to enter the damper. The gas also adds a spring effect to the force generated by the damper, maintaining the damper at its extended length when no force is applied (Gillespie, 2006). On the other hand, in the twin-tube design (Fig. 1-4(b)), outer and inner tubes form two chambers: the inner chamber with a piston moving in it, and the outer chamber that contains the gas chamber and acts as a reservoir for the oil. The outer chamber equalizes the oil volume changes caused by the piston rod movement. There are also two valves used (see Fig. 1-4(b)) in the twin-tube design: a piston valve and a foot valve. During the suspension extension, the piston valve alone takes over the damping, applying resistance to the flowing oil. However, when the suspension compresses, the foot valve, and partially the piston valve, determine the damping action.

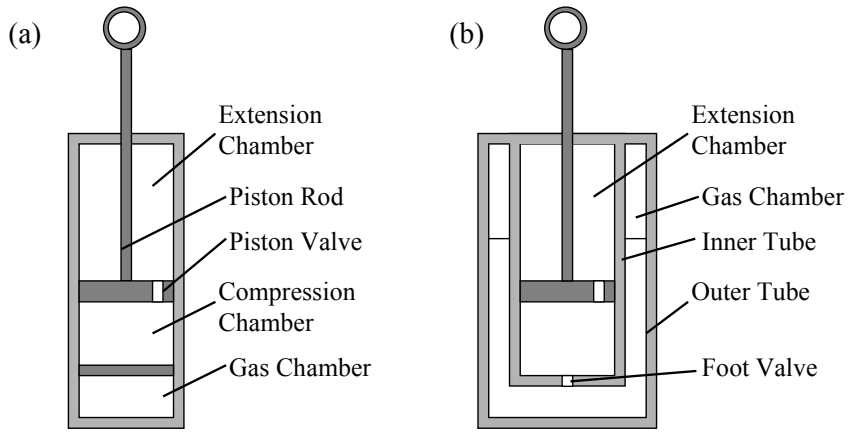

Fig. 1-4 (a) Mono-tube and (b) twin-tube dampers.

Mono-tube dampers are simpler in terms of manufacturing, lighter due to the fewer parts, requiring higher gas pressure, and are more susceptible to damage of the cylinder compared to their twin-tube counterparts. In contrast, twin-tube dampers can operate with lower gas pressure, but they are more complex, and have issues with dissipating the generated heat.

On the other hand, variable dampers vary the damping rate by varying the size of the valve opening by means of a servo-valve, shim-valving, piezoelectric actuators, solenoid-valve, or using MR-fluid in which the viscosity of the oil is varied, instead of the size of the valve opening. The following section describes the solenoid-valve and MR dampers.

1.3.2 Semi-active Dampers

Semi-active dampers use an actively powered valve or other technologies that allow the damping characteristics of the damper to be changed and adjusted. Like hydraulic passive dampers, they are designed in a way that the damping force is proportional to the relative velocity of the dampers' endings (Preumont, 2002). The variable damping in semi-active dampers arises from a variety of technologies, such as: solenoid-valves, ER and MR-fluids, and piezoelectric actuators. Currently, commercialized semi-active dampers utilize the solenoid-valve and MR-fluid technologies.

A solenoid-valve can be used in a damper to mechanically control the size of the piston valve's orifice. It can provide a high speed, accurate flow control at a high operating pressure. Moreover,

Solenoid-valves can be used in two- or three-state dampers in which the damping is varied between hard and soft by opening and closing a bypass valve.

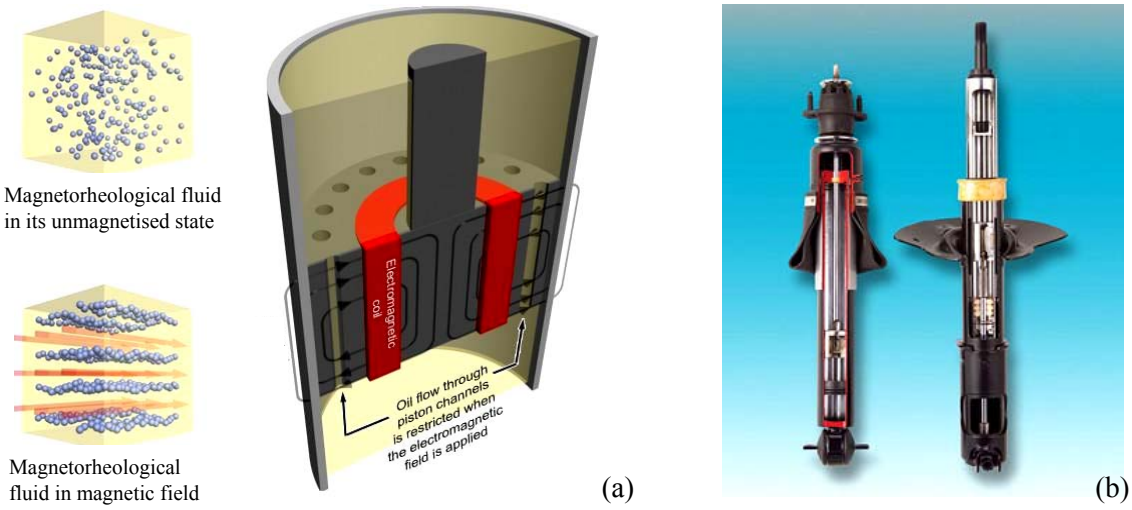

Fig. 1-5 (a) Schematic of an MR damper (Web1), and (b) cutaway of a MagneRide rear shock absorber (Web2).

Rheological fluids have flow characteristics that can be varied in a controlled manner by an applied magnetic field. The fluid's response is almost instantaneous and reversible. In an MR damper, the oil passages are surrounded by an electromagnet, as illustrated in Fig. 1-5. When the electromagnet is turned on, the iron particles in the oil passages align to form fibers in the oil, making the fluid thicker and therefore more resistant to flow. The thickness or viscosity of the fluid can be infinitely adjusted from that of a base oil to almost a plastic in less than two milliseconds simply by adjusting the current flowing through the coil. When the current is turned off, the fluid reverts to its base viscosity just as quickly. The result is a variable resistance to the fluid flow within the damper piston, providing a variable damping capability for the damper. Two variable dampers (the solenoid-valve damper of a Volvo S60 and the MR damper of a Cadillac SRX) are experimentally tested and modeled in Sections 2.2.1 and 2.2.2, respectively.

1.3.3 Eddy Current Dampers

Eddy currents (also known as Foucault currents) are caused when a conductor is exposed to a varying magnetic field. They are induced either by the movement of the conductor in the static field or by changing the strength of the magnetic field, initiating motional and transformer electromotive forces

(emf), respectively. Since the generated eddy currents create a repulsive force that is proportional to the relative velocity of the field and conductor, the moving magnet and conductor behave like a viscous damper.

For more than two decades, the application of eddy currents for damping purposes has been investigated, including magnetic braking systems (Cadwell, 1996), (Heald, 1996), and (Wiederick *et al.*, 1987), the vibration control of rotary machinery (Genta *et al.*, 1992), structural vibration suppression (Sodano *et al.*, 2005), (Bae *et al.*, 2005), and (Sodano *et al.*, 2006), and vibration isolation enhancement in levitation systems (Teshima *et al.*, 1997) and (Elbuken *et al.*, 2006). Graves *et al.* (2000) have derived a mathematical representation for Eddy Current Dampers (ECDs), based on the motional and transformer emf. Also, the authors have developed an analytical approach to compare the efficiency of the dampers in terms of these two sources.

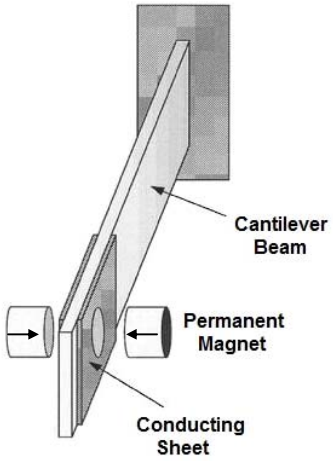

Fig. 1-6 Eddy current damper proposed by Sodano *et al.* (2006).

Sodano *et al.* (2005) have analyzed the suppression of cantilever beam vibrations, where a magnet is fixed so that it is perpendicular to the beam motion, and a conducting sheet is attached to the beam tip. Authors (Sodano *et al.*, 2006) have been modified the theoretical model of their ECD, and further developed it by applying an image method to satisfy the boundary condition of the zero eddy current density at the conducting plate's boundaries. Fig. 1-6 depicts the proposed configuration of their eddy current damping system, consisting of a cantilever beam with a copper conducting plate located between the two fixed PMs. The device utilizes two PMs with opposite magnetization directions, intensifying the radial magnetic flux density, to enhance the damping effect. Teshima *et al.* (1997)

have studied the effect of an ECD on the vibration isolation properties of superconducting levitation, and demonstrated that in the vertical direction, the damping is improved by approximately 100 times by using ECDs. For high precision magnetic levitation, Elbuken *et al.* (2006) have investigated the eddy current damping. Also it has been suggested that an ECD can suppress the vibration of the levitated object (Elbuken *et al.*, 2006). Schmid and Varaga (1992) have designed and analyzed a vibration attenuation system for the construction of high-resolution nanotechnology structures such as the Scanning Tunneling Microscope (STM) by using ECDs. For ECDs and couplers under rather general operating conditions, Tonoli (2007) has presented a physical, dynamic model. Ebrahimi *et al.* (2008) have developed a novel magnetic spring-damper based on the eddy current damping phenomenon.

Applications of the eddy current damping effect in vibration suppression studies have been reported, but, to the best of the author's knowledge, the application of the eddy current in vehicle suspension systems has not been addressed in prior publications. Chapter 3 covers the development and feasibility study of utilizing eddy current damping effect as a potential passive damping source in vehicle suspension applications.

1.3.4 Electromagnetic Dampers

In conventional hydraulic suspension systems, shock absorbers convert the mechanical energy of the vibration into heat energy, so this mechanical energy is dissipated (Suda *et al.*, 1996). Segal et al. (1982) have demonstrated that roughly 200 watts of power are dissipated in an ordinary sedan traversing a poor road at 13.4 m/s; hence, suspension systems have the potential for energy regeneration. Using electromagnetic dampers (composed of electromechanical elements), the kinetic energy of vehicle body vibration can be regenerated as useful electrical energy. The electromagnetic dampers (as actuators) have the potential to be used in active suspension systems.

Some authors have proposed self-powered active control systems by means of regenerative shock absorbers (Wendel *et al.*, 1991). This new generation of shock absorbers is expected to be available for practical use in the near future. Karnopp (1989) has devised a new electromechanical damper for vehicle applications, consisting of copper wires and PMs. He has proven that for oscillation frequencies, typically expected in road vehicle suspensions, electro-dynamic variable shock absorbers are feasible. Suda *et al.* (1969) have used a rotating DC motor to convert vibrational energy to electrical energy. They have explained some trade-offs involved during the design process; for

example, there is a trade-off between the energy regeneration efficiency and the damping coefficient, which depends on DC machine internal and external resistance. They also used two linear DC motors, one in the primary suspension called “regenerative damper” which regenerates the vibration energy and stores it in the condenser, and the second linear DC motor in the secondary suspension system, which uses this energy to attain active control (Suda *et al.*, 1998). Also, Suda (2004) has proposed another electromagnetic damper, as shown in Fig. 1-7, using DC motor, planetary gears, and a ball screw mechanism to convert the transverse motion of the vibration between the car body and wheels into the rotating motion of the DC motor. Arsem (1971) has proposed an electric shock absorber for automobile suspension systems. It converts the mechanical energy to electricity for charging the battery. The spiral screw causes the conversion of the linear motion to the rotary motion such that the screw moves up and down, the rotor starts to rotate, and an electric current is generated in the stator. Murty *et al.* (1989) have disclosed an electric variable damper for vehicle suspension systems, converting vertical suspension motion into rotary motion via a ball screw mechanism. To convert the three-phase alternator output to a single DC current, a rectifier bridge is used. The reported device dissipates the vibration energy as heat through a variable load resistance and does not recover the energy.

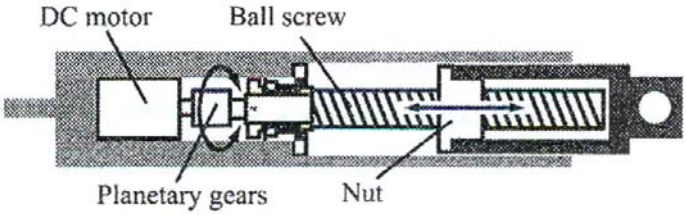

Fig. 1-7 Proposed electromagnetic damper by Suda *et al.* (2004).

Merritt *et al.* (1989) have proposed a linear electrical generator with a reciprocating armature with rectangular PMs, which are coupled to a source of relative motion. The device does not appear to fully utilize the magnetic field, generated by the PMs, since the generator uses only a single magnetic pole-coil interaction, which reduces the device’s efficiency. Konotchick (1994) has proposed several designs of linear electric power generators, consisting of a cylindrical assembly of rare earth magnets (NdFeB) and coils, positioned to move reciprocally relative to each other. The device is more appropriate for relatively large amplitude motions such as wave energy generation. To maximize the radial magnetic flux density in a linear generator that acts as a shock absorber, Goldner and Zerigian

(2005) have proposed a new assembly of magnet and coil winding arrays. The damper does not appear to be controlled actively, and so ride comfort and road-handling are sacrificed. Recently, Bose Corporation (maker of famous Bose speakers) has proposed an electromagnetic active suspension system for automobiles. The Bose active suspension system, composed of an electromagnetic motor as the actuator unit and a power amplifier, delivers electrical power to the motor in response to signals from the control unit. However, no data is available on the performance of these dampers.

Fig. 1-8 Michelin active wheel with an active suspension system (Kendall, 2008).

The Michelin Company also unveiled its electric drive system in late 2008. Fig. 1-8 depicts the Michelin novel active wheel incorporates an active suspension system. Their proposed system integrates a drive motor with electrical active suspension components. The principal component is a compact electric motor rated at 30 kW continuous output. A second motor provides power for the active suspension system, fitted vertically across the diameter of the wheel (Kendall, 2008). Michelin has claimed that the suspension system response time is 3 ms. With propulsion and suspension components fitted in the wheel, it would free up space in the front of the car that could result in better impact energy absorption, better interior packaging, and vehicle weight reduction.

Gupta *et al.* (2007) described the manufacturing and implementation of two electromagnetic shock absorbers (one based on a linear motor and the other one based on a rotary dc motor) for a small all-terrain vehicle (ATV). Similar to the design proposed by Goldner and Zerigian (2005), their proposed linear shock absorber is composed of two concentric coil rings moving relative to the two concentric magnet rings.

Finally, the most recent research in using the electromagnetic damper concept is done by Allen (2008). He presented the design, fabrication, and testing of an active suspension on a quarter-car system, using a tubular linear motor with various control algorithms. His master thesis is on developing control algorithms for the linear motor in the suspension system to minimize the transmitted acceleration to the sprung-mass.

1.3.5 Hybrid Dampers

Although, significant performance improvement is achieved by introduction of active suspension systems, they are not commercialized yet due to their cost, weight, and fail-safety issues. Another disadvantage of active suspension systems is their high energy consumption. Consequently, the idea of using hybrid electromagnetic dampers was formed, addressing the active suspension system drawbacks. Hybrid dampers combine an active actuator part with a passive damper unit, maintaining the fail-safety of passive dampers and keeping the performance of the active part, with a smaller, lighter, and more reliable design.

There is not much research in the field of hybrid dampers, especially in vehicle suspension applications. However, the application of hybrid dampers for controlling seismic response of buildings and towers (Watakabe *et al.*, 2001) and (Lee *et al.*, 2007), vibration suppression of machine components (Yau and Chen, 2006) and (Moore *et al.*, 1997), and other vibration isolation systems (Lee and Jee, 1996) has been investigated in recent years. Foshage *et al.* (1996) developed a hybrid actuator for multi-axis vibration isolation of an optical spacecraft payload. The active component was a voice coil motor, while a parallel passive component was used providing a backup isolation in case of electrical break down or control instability. Similar applications are developed by Vailon *et al.* (1999) and Anderson *et al.* (1999), using a piezoelectric stack actuator for active vibration suppression. Martins *et al.* (1999) proposed a new hybrid damper design for vehicle suspension application, composed of a linear actuator as the active unit, and the hydraulic passive damping effect as the passive part. Lin *et al.* (2007) proposed a hybrid base isolation with MR dampers, and showed that a combination of high damping rubber isolators and a semi-active MR damper can provide robust control of vibration for large civil engineering structures that need protection from a wide range of seismic events. Hu and Wereley (2008) developed a novel hybrid MR-fluid elastomeric lag damper for helicopter stability augmentation, so that the damping requirements can be varied as a function of different flight conditions. Fig. 1-9 illustrates their proposed hybrid damper in which two MR

dampers are mounted parallel to an elastomeric damper to form a hybrid damper having three attributes: a baseline stiffness, a base line damping, and continuously adjustable damping capabilities (Hu and Wereley, 2008).

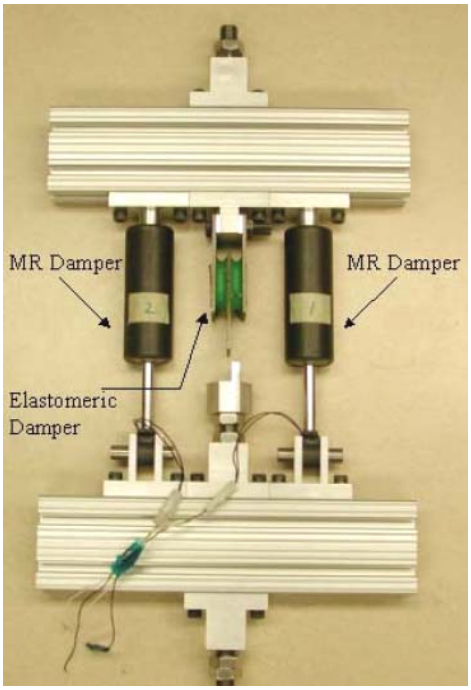

Fig. 1-9 The hybrid damper proposed by Hu and Wereley (2008) for helicopter stability augmentation.

After this brief overview on different damper technologies, the next section introduces various approaches for damper modeling. In the dynamic studies of vehicles, accurate damper modeling is essential. A number of damper modeling methods have been proposed, such as physical, rheological, and nonparametric modeling techniques. Among different modeling approaches, the main focus in this thesis is nonparametric and rheological models.

1.3.6 Damper Modeling

In a commercial hydraulic damper, the damping effect is caused by the fluid passes through a complex series of orifices and valves. Therefore, modeling and identification of a damper can be very complex due to the number of parameters involved in the process. In this section, different modeling

approaches for damper identification are discussed, and two are highlighted. The modeling approaches for the damper modeling are listed as follows:

- Analytical (physical) modeling
- Experimental modeling
    - Rheological
        - Linear
        - Bilinear
        - Complex
    - Nonparametric
        - Frequency domain
        - Time domain
            - Continuous velocity pick-off
            - Peak velocity pick-off

A *physical model* is based on a detailed description of its internal structure, and the processes inside the shock absorber during operation. From the theoretical perspective, the physical model represents the behavior of the damper for a wide operating range. However, the model is somewhat complex, which demands time-consuming subroutines. Also, the number of parameters necessitates many measurements and restricts the design flexibility. On the other hand, *experimental models* are based on data obtained from experiments, and are divided into two groups, rheological and nonparametric models, discussed in the next sections.

Rheological models, which utilize dashpots, springs, friction, and backlash elements, result in models with more or less the same advantages and disadvantages as physical models. The use of hysteresis and backlash elements for modeling non-linearities causes a set of non-linear differential equations, requiring numerical solutions. For accurate modeling, the price is time-consuming subroutines. Fig. 1-10 depicts a lumped parameter representation of a damper. An ideal damper is modeled as a linear dashpot only, but in an actual damper, the force and velocity relationship is not linear. Spring, dry friction, and inertia elements are also added to the model to account for the following

- The presence of bushings at the point of attachment of the damper to the chassis of the suspension
- The effect of the pressurized gas chamber

● The oil compressibility due to gas emulsification

● The effective inertia of the moving mass

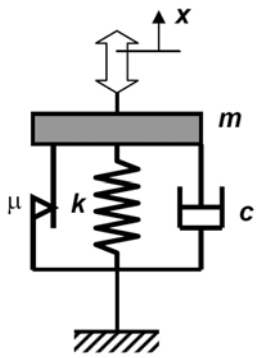

Fig. 1-10 Lumped model of a damper, consisting of nonlinear damper and spring elements with dry friction and inertia effects.

Nonparametric models define a relationship between the measured quantities such as force, on the one hand, and displacement and velocity, on the other hand, by using mathematical approaches. In contrast to the previous modeling methods, nonparametric modeling accurately represents the behavior of the damper only in the limited operating range; the positive aspect is its time efficiency. In this category of modeling, the shock absorber is modeled as a black box for a certain range of test conditions that cause the development of an input/output relationship. The selected parameters may or may not have a physical meaning. It should be noted that the parametric models are valid only within the range of test conditions. Nonparametric modeling is divided into two categories: frequency and time domain modeling. In frequency domain modeling, a sine-sweep displacement excitation is applied and the reaction force measured. Force-displacement transmissibility, dynamic stiffness, and other useful parameters can be plotted with respect to frequency. On the other hand, in the Continuous Velocity Pick-off (CVP) method, a sinusoidal excitation is applied to the damper, and the damper reaction forces are measured in that cycle. The CVP method is suitable only when the damping force is not position-dependent. The Peak Velocity Pick-off (PVP) involves peak values only on the force-velocity curves. By applying a range of sinusoidal excitations, with respect to the amplitude and frequency, the PVP method captures the peak values of each excitation for plotting the force-velocity curves (Vahid, 2006). The CVP and PVP approaches are the most common ones adopted to extract the damping properties in vehicle suspension studies, and are widely used in this research.

1.4 Research Motivation and Methodologies

Active suspension systems have shown superior performance in terms of ride comfort and road-handling performances compared to other passive and semi-active suspension systems in automotive applications. Nevertheless, they are not commercialized yet due to their high weight, complexity, cost, and energy consumption. Another issue with active suspensions is that they are not fail-safe in case of a power break-down. Almost, all systems that are implemented in automotive suspension are based on hydraulic or pneumatic operation. It is verified that current solutions for implementation of hydraulic/pneumatic dampers in active suspension are not practical due to the aforementioned problems. Consequently, Hybrid dampers, as a potential solution addressing these challenges, are proposed and studied in this Ph.D. research.

Hybrid dampers consist of two main elements, an actuator, as an active part of the damper, and a passive part, as a back-up in case of power failure; the passive part also provides a base damping effect in the system. Maintaining the same level of controllability, the hybrid damper is smaller, lighter, and more reliable compared to an active damper, due to the presence of a passive damping element. The use of electromagnetic actuators is an alternative for the implementation of the active element in a hybrid damper, while it has the advantage of regenerating power out of the kinetic energy of the vehicle body motion. Electromagnetic dampers are cost effective, regenerative, and simple to manufacture, while they have the potential to be used as a sensor/actuator, simultaneously. Therefore, electromagnetic dampers are studied and developed in detail in this research.

The development of eddy current dampers as a potential source for passive damping element in the final hybrid design is another main contribution of this research. Amongst the advantages of the proposed eddy current passive damper, one can note the simplicity of the design requiring no external power supply or other electronic devices. The eddy current damper is an oil-free passive damper, so the sealing, oil leakage and other related drawbacks are non-existent. Consequently, the design and development of eddy current dampers is thoroughly considered and studied in this thesis.

1.5 Thesis Outline

This PhD thesis focuses on the design, modeling, and performance study of hybrid electromagnetic dampers. This venture further involves a study of commercial, eddy current and electromagnetic dampers, analytical and numerical modeling, and prototype fabrication and experimental analysis to

verify the numerical and analytical studies and proof of concept. This process is presented and organized in six chapters, as follows:

Chapter 1 presents a brief introduction on the vehicle suspension system, including different vehicle suspension types, conventional control strategies used in vehicle suspension, suspension modeling, and suspension performance indexes. The Introduction chapter follows with an overview of dampers in vehicle suspension, including a review of the literature on eddy current, electromagnetic, and hybrid damper technologies. This chapter concludes with a concise summary of damper modeling.

Chapter 2 includes the assessment of the damper design requirements and constraints, involving the evaluation of commercial dampers, testing off-the-shelf variable dampers such as solenoid-valve and MR dampers to assess the existing variable damper technologies, and experimental analysis on the active suspension systems. Experimental results for the solenoid-valve and MR dampers are presented, and the time-domain nonparametric approaches, CVP and PVP, are applied to study the dampers behavior at the velocity range expected in a vehicle suspension system. The derived results, together with the results from the active suspension analysis, leads towards an inclusive perception on the damper design requirement to be used in the design process. Since the primary goal of this research is to develop hybrid electromagnetic dampers, chapters 3 and 4 will deal with the eddy current damping effect and electromagnetic dampers, as two essential components of a hybrid damper, achieving the ultimate goal of the project.

Chapter 3 presents a study on the eddy current damping phenomenon as both a novel damping effect and a potential passive damping source in the final hybrid damper design. This process involves several steps including: analytical model development, finite element analysis, heat transfer analysis, designing a prototype for the proof of concept, fabricating the prototype, and preparing a test bed for the experimental evaluation of the developed model. This chapter includes extensive experimental analysis on the eddy current damping effect, including time and frequency domain and transient response analysis as well as magnetic field measurements. The objective further involves the feasibility study of a stand-alone eddy current damper for passive automotive suspension application. This includes the analysis of the design parameters correlation with the damper performance, a comparison of the results with relevant passive off-the-shelf dampers, and finally, a modification of the design to improve the performance of the prototype.

Chapter 4 deals with the design procedure of an electromagnetic active damper as a stand-alone unit. This begins with selecting the most appropriate topology of the electromagnetic damper for vehicle suspension applications. The objective necessitates the preliminary and parametric design of a prototype for the proof of concept. An analytical approach is employed for the initial design of an electromagnetic damper prototype. This is followed by fabricating a prototype, preparing a test bed, and performing the experimental study on the prototype. Experiments are carried out to verify the designed model, which facilitates the final hybrid damper design, in the last chapter. Finally, a full-scale electromagnetic damper for automotive suspension application is designed and the maximum achievable damping force is estimated to investigate the feasibility of using this damper in an automotive active suspension system.

Chapter 5 addresses the final hybrid damper design and evaluation. After the assessment of the current knowledge of the suspension systems and the damper design requirements, together with the development of the eddy current and electromagnetic dampers, the final step is the design and evaluation of hybrid dampers. It is explained how the hydraulic/eddy current forces can provide the required passive damping effect to ensure a smaller, lighter, and more reliable active damper with reduced power consumption.

The feasibility of the hybrid damper concept is studied, started with selecting appropriate hybrid damper topologies, followed by initial sizing of the electromagnetic subsystem. Two sources of passive damping are proposed for the hybrid damper conceptual designs: hydraulic and eddy current forces. For the first design, a general hydraulic damper design procedure is presented and then narrowed down to the specific case of the electromagnetic/hydraulic damper design. For the second design, an attempt is made to derive the optimum dimensions and materials to achieve the required passive damping performance from the eddy current damping effect. Finally, the hybrid damper designs are compared and their advantages relative to the previous active damper design are demonstrated.

Chapter 6 presents the overall conclusion of this Ph.D. thesis, followed by future research recommendations. Academic publications that are resulted from this Ph.D. research are listed in this chapter.

Chapter 2

Damper Design Requirements

2.1 Overview

One of the key issues in the damper design process is to assess the damper requirements and constraints within a vehicle suspension system context; this chapter addresses the evaluation of damper design requirements. Unfortunately, there aren't many standards for the damper design requirements, since the damper design is mainly influenced by the vehicle make, model, and envisaged functionality. This chapter comprises three main sections. The first two presents an experimental analysis on semi-active and active dampers, respectively, while the last section summarizes the results and discusses force, damping, geometry, and other design factors. The derived experimental analysis from semi-active dampers, together with the results from active suspension analysis, leads to a general understanding of the design requirements.

2.2 Evaluation of Commercial Semi-active Damper Technologies

The currently available semi-active damper technologies are divided into two main groups: dampers that use solenoid valves, and dampers that utilize Magneto-Rheological (MR) fluid to control the damping characteristics. This section involves the evaluation of these two commercial variable dampers. Experimental results for the solenoid-valve and MR dampers within the velocity range expected in automotive suspension applications (<1.2 m/s) are presented and the damper performance for different input voltages are discussed.

2.2.1 Experimental Modeling of a Solenoid-valve Damper

To evaluate the solenoid-valve damper performance, the front damper of a Volvo S60R (Fig. 2-1(b)) is purchased, and experiments are conducted with a hydraulic shaker at the University of Waterloo. The shaker is equipped with a 35 klb load-cell and an internal Linear Variable Displacement

Transducer (LVDT) to measure the relative displacement. Fig. 2-1(a) reflects the hydraulic shaker and the MTS-FlexTest-SE controller used in the experiment. The damper is fixed at the bottom and undergoes a sinusoidal excitation at the top with fixed amplitude at frequencies between 0.25 Hz and 6 Hz. The system sampling frequency is also set to 1000 Hz.

Fig. 2-1 (a) UW MTS shaker test setup (Vahid, 2006) and (b) Volvo S60 solenoid-valve damper.

Fig. 2-2 shows the force-displacement and force-velocity data, obtained from the averaged measurement results for constant excitation amplitudes with increasing frequencies at no input voltage to the solenoid, by using the CVP method.

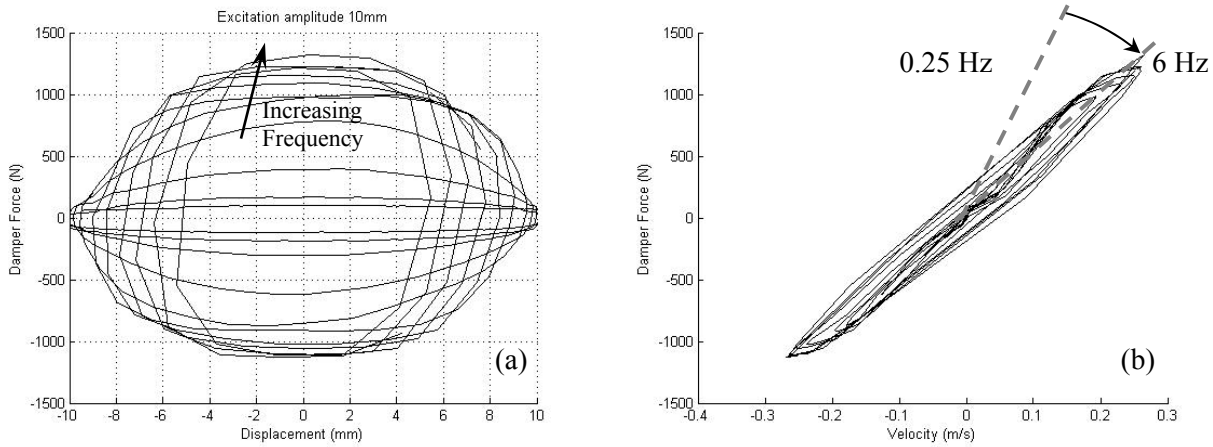

Fig. 2-2 (a) Damper force vs. displacement and (b) damper force vs. velocity (Vahid, 2006).

The test is conducted at a constant amplitude of 10 mm with the damper force increased with frequency. Although the amplitude of the vibration is expected to be constant, the actual amplitude of vibration shrinks at higher frequencies due to the limitations in the hydraulic system.

The force-velocity plot in Fig. 2-2(b) reveals the overall inclination of the curves, which is interpreted as a decrease in the damping coefficient, at higher velocities; the shape of the curves are changed from a line to a rotated ellipse due to the inertia effect. The influence of the frequency on the damping coefficient increases even more when a voltage greater than 2 volts is applied to the solenoid.

Test data can also be represented by using the PVP method in order to eliminate the displacement-dependency effect of the damping coefficient in the force-velocity curves. Fig. 2-3 shows the force-velocity behavior in extension (rebound) and compression (bump) for a series of tests with a preset excitation amplitude of 10 mm at frequencies between 0.25 and 12 Hz. The test is repeated for each applied voltage. The resistance and inductance of the solenoid are 5.3 Ω and 7.78 mH, respectively. An experimental non-parametric bi-linear model is fitted to the data in Appendix B.

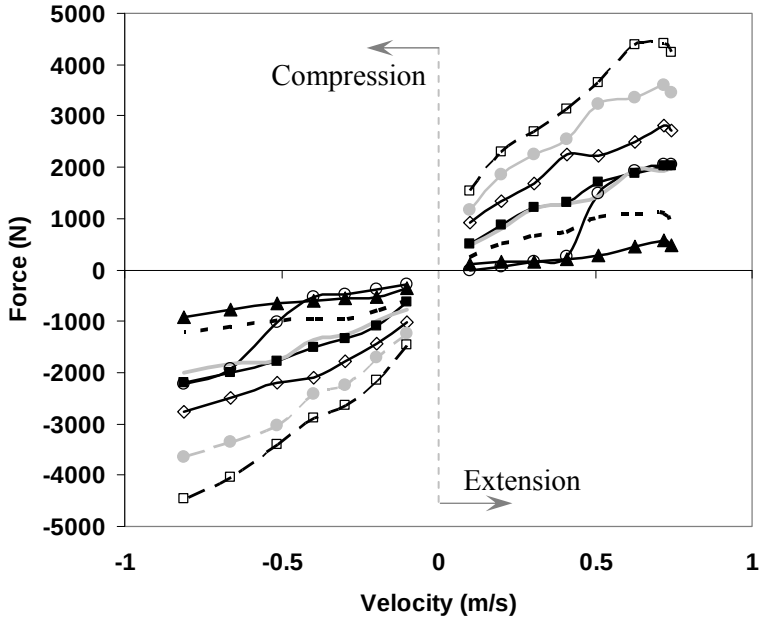

Fig. 2-3 Force-velocity behavior of the solenoid-valve damper at different applied voltages using the PVP method. —■—:0A (0V), —○—: 0.2A (1.06V), —▲—: 0.4A (2.12V), ▪▪▪: 0.6A (3.18V), ——: 0.8A (4.24V), —◊—: 1.0A (5.3V), —●—: 1.2A (6.36V), — □ —: 1.4A (7.42V).

Fig. 2-4 illustrates a 3D surface of the force vs. peak velocity and the applied voltage for the measured data.

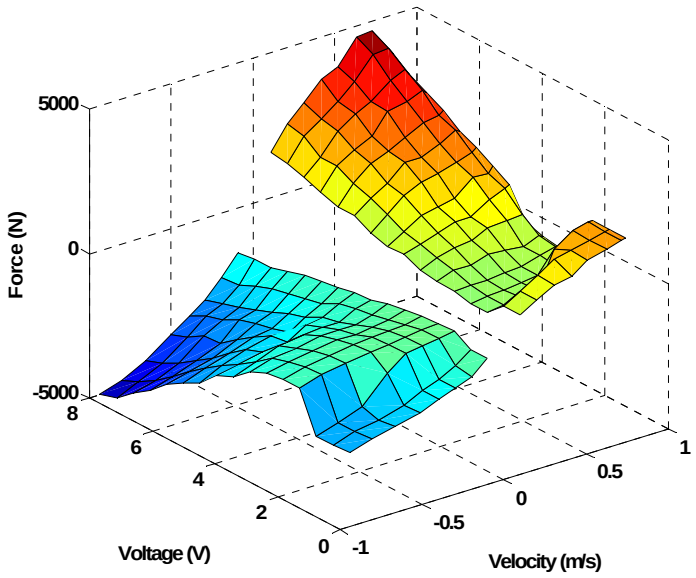

Fig. 2-4 Solenoid-valve damper force vs. velocity and input voltage.

The Volvo damper exhibits a relatively high level of damping coefficient in the off-mode. As shown in Fig. 2-4, by applying voltage to the Volvo damper, the damping coefficient is decreased, applying voltage up to 2 volts. Applying higher voltages increases the damping coefficient such that it is higher than the off-mode's.

2.2.2 Experimental Modeling of an MR Damper

To investigate the behavior of an MR damper, two MR dampers of the Cadillac SRX (front and rear) are purchased, and experiments are carried out on the same test bed used in the previous section. Fig. 2-5 displays the test equipment, as well as the rear and front dampers. Experiments are conducted with a preset excitation amplitude of 10 mm at frequencies between 0.25 and 15 Hz. The test is repeated for each applied voltage between 0 and 3.5 V. The resistance of the MR damper's coil is equal to 1Ω.

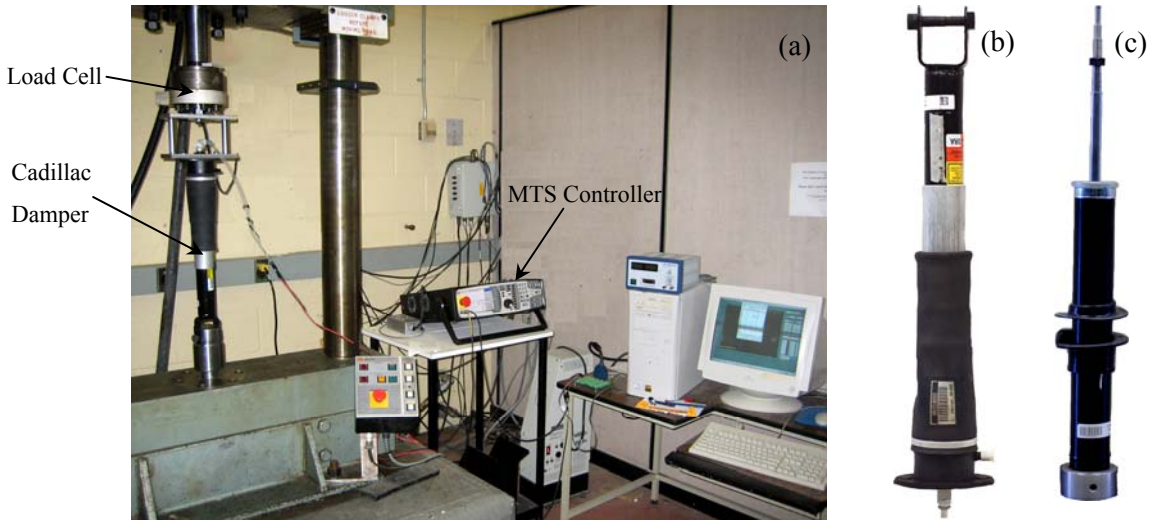

Fig. 2-5 (a) UW MTS shaker test setup, (b) Cadillac SRX rear, and (c) Cadillac SRX front damper.

In case of the front damper, the force-velocity plot for each applied voltage is shown in Fig. 2-6, by using the same procedure as in the previous section.

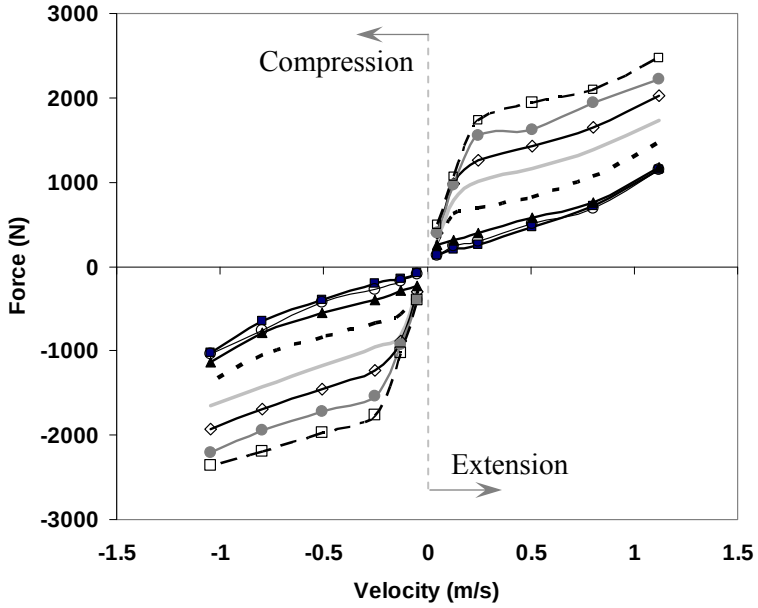

Fig. 2-6 Force-velocity behavior of the MR damper at different applied voltages using the PVP method. —■—:0A (0V), —○—: 0.5A (0.5V), —▲—: 1.0A (1.0V), ▪▪▪: 1.5A (1.5V), ——: 2.0A (2.0V), —◊—: 2.5A (2.5V), —●—: 3.0A (3.0V), — □ —: 3.5A (3.5V)

A non-parametric bi-quadratic model is fitted to the data in Appendix B. For low velocities, damper force/velocity curves are commonly arranged to be particularly steep (Polak and Burton, 1971). This higher damping at low velocities is also inferred from Fig. 2-6.

Fig. 2-7 illustrates a 3D surface of the force vs. peak velocity and applied voltage for the measurement data. For the Cadillac damper, the damping force increases with the increase in the applied voltage, resulting in a low damping coefficient in the off-mode. A relatively low damping characteristic in the off-mode is one of the MR damper's drawbacks. In addition, the literature on MR dampers exposes some drawbacks of MR dampers such as the degradation of the MR-fluids, sealant failure, leakage and performance problems as well as high cost for commercial vehicles.

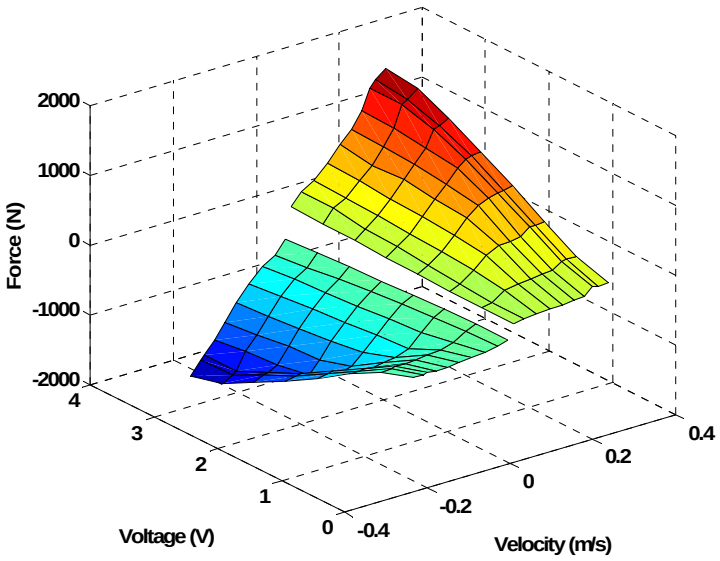

Fig. 2-7 Cadillac MR damper force vs. velocity and input voltage.

Table 2-1 shows the damping coefficient range for Cadillac MR-fluid and Volvo solenoid-valve dampers in both extension and compression stages. In general, the damping coefficient in the extension stage is higher compared to that of the compression stage (ex. 10% higher for MR damper). The minimum damping for the MR damper case is obtained at no voltage applied, and is roughly equal to 800 Ns/m for both extension and compression stages.

Table 2-1 Damping properties of semi-active dampers in extension and compression.

Damper type	Extension		Compression	
	C_{min} (Ns/m)	C_{max} (Ns/m)	C_{min} (Ns/m)	C_{max} (Ns/m)
Solenoid-valve (Volvo)	101 @ 1V	15,302 @ 7.4V	1,127 @ 2.1V	14,330 @ 7.4V
MR-fluid (Cadillac)	860 @ 0V	9,872 @ 3.5V	772 @ 0V	8,177 @ 3.5V

The minimum damping at extension is much lower for the solenoid-valve damper compared to the MR damper, which makes it more suitable for applying optimal control strategies. This will be discussed in Section 2.3 with more details. In addition, the damping range is more extended for the solenoid damper case study.

2.2.3 Electrical and Mechanical Time-constant Measurement

Despite different semi-active control strategies, the response-time is a key factor for all controllable dampers. In this section, the response-times of the off-the-shelf semi-active dampers are measured and discussed. There are some parameters that affect the response-time of semi-active dampers and are out of the scope of this thesis, such as: operating current, piston velocity and system compliance (Koo *et al.*, 2006). The response-time of a semi-active damper is limited by the response of the fluid as well as the driving electronics. The goal is to measure the actual mechanical time-constant of the semi-active dampers, and then compare the results with their electrical time-constant.

The response-time of an electro-mechanical system is affected by the electrical time-constant due to the system inductance. Electrical time-constant of the dampers are obtained from

$$\tau_e = L / R , \tag{2-1}$$

where R and L are the resistance and inductance of the driving electronic system, respectively. The electrical time-constants for the solenoid-valve and MR-fluid dampers are obtained from (2-1) as 1.4 and 2.3 ms, respectively.

For semi-active dampers, the mechanical time-constant is defined as the required time for the force signal to reach 90% of the final-state/command signal (Eslaminasab, 2008). The mechanical time-constant of semi-active dampers should be evaluated at constant velocities, because the force variation due to the coil activation is the only concern, and the force change due to the velocity

complicates the analysis. The most appropriate displacement pattern that satisfies the constant velocity condition is a triangle wave (Koo *et al.*, 2006). Fig. 2-8 shows the typical procedure for mechanical time-constant evaluation in semi-active dampers. The power is switched when the displacement is around zero, where the velocity is constant. The experimental results from a solenoid-valve damper show a mechanical time-constant equal to 16 ms. In case of the MR dampers this value is measured as 14 ms (Eslaminasab, 2008). For a generic MR-fluid damper, the mechanical time-constant varies with the operating current and the piston velocity, and is found to be less than 25 ms (Koo *et al.*, 2006).

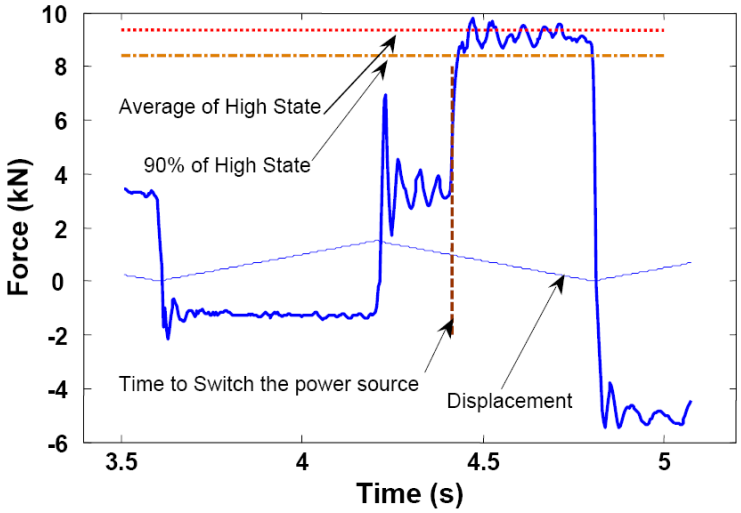

Fig. 2-8 Mechanical time constant for a solenoid-valve damper (current from 0.3 to 0.8 A) (Eslaminasab, 2008).

It is revealed that the overall response-times of both semi-active dampers are dominated by the mechanical time-constants rather than the electrical ones.

2.3 Comparison between Active and Semi-active Suspension Control Strategies

2.3.1 Conventional Active Suspension Control Strategies

From early 1980s, it has been recognized that the actuator can moderate the motion of the vehicle body and significantly improve ride comfort (Pollard, 1983). The active component is defined as the power-driven device that can inject, store, transfer or extract energy (Chang, 1998). Recently, the

active suspension concept has been extensively researched in academic works. Optimal control has been widely used to achieve a better comfort/handling performance. Prokop (1995) used road preview information to improve the ride quality, utilizing LQG (linear Quadratic Gaussian) and LQR (Linear Quadratic Regulator) optimal control theories. Hrovat (1993) utilized LQ (Linear Quadratic) optimal control to minimize the cost functions, combining excessive suspension stroke, sprung-mass acceleration, and sprung-mass jerk in 1DOF models, 2DOF models, half-car models, and full-car models. In general, the LQG controller is less robust with respect to system modeling errors. Moreover, determining the weighting coefficients for the LQG is a challenging task. Until now, most of the weighting coefficients for LQG/LQR have been determined by trial-and-error (Shen, 2005).

In searching for the optimal feedback gain that minimizes the cost function of the mean square velocity of the sprung-mass and the mean square control effort, the well-accepted skyhook feedback policy gives the best results (Shen, 2005). The skyhook control law is the most widely-used control policy for semi-active dampers, although many other variations of the skyhook control policy have been introduced in the past two decades (Ahmadian and Vahdati, 2006). Li and Goodall (1999) compared different control strategies for applying the skyhook damping control policy in active suspension of railway vehicles. Skyhook damping is explained as a damping force in proportion to the absolute velocity of the sprung-mass, and in opposite direction to the sprung-mass absolute velocity. Consider moving the damper from between the sprung-mass and the base to the position shown in Fig. 2-9. At this configuration, the damper is connected to an inertial reference in the sky (a vertically-fixed ceiling relative to a ground reference).

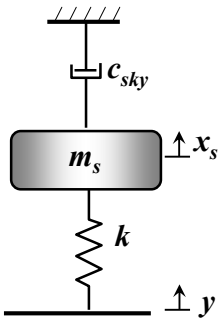

Fig. 2-9 Ideal skyhook configuration.

The damping force (control effort) is obtain simply as

$$F_d = -c_{sky}\dot{x}_s \tag{2-2}$$

This control policy, so-called *active continuous skyhook*, can be ideally realized using an active force generator. This ideal case can not be emulated with any passive/semi-active damper. For instance, compare the system in Fig. 1-1(a) with an ideal skyhook configuration in Fig. 2-9, and assume the situation where the base and unsprung-mass are separating and the mass is moving downward ($0 > \dot{x}_s > \dot{y}$). The force applied to the mass is in an upward direction for the skyhook configuration, while it is in a downward direction in the real case of Fig. 1-1(a).

The concept of semi-active control was first proposed by Crosby and Karnopp (1973), while the skyhook on-off control damper was first suggested by Karnopp *et al.* (1974). For a 1DOF system the ideal skyhook is modified to a *semi-active on-off skyhook* control policy, expressed as:

$$\begin{cases} F_d = -c_{\max}(\dot{x}_s - \dot{y}) & if \quad \dot{x}_s(\dot{x}_s - \dot{y}) \geq 0 \\ F_d = 0 & if \quad \dot{x}_s(\dot{x}_s - \dot{y}) < 0 \end{cases} \tag{2-3}$$

Although, the semi-active skyhook suggests the zero damping force in a situation where $\dot{x}_s(\dot{x}_s - \dot{y}) < 0$, in practice, applying zero damping force by a semi-active damper is not applicable. Karnopp *et al.* (1974) encountered the difficulty of reducing the damping sufficiently when the control law demands no force.

Since the skyhook on-off control method can be easily implemented, it has been widely used for vehicle suspension control (Shen, 2005). Margolis *et al.* (1975) have suggested another on-off control strategy. The idea was to switch the damper off when the sprung and unsprung-masses move in the same direction, and the unsprung-mass has a large velocity. Rakheja and Sankar (1985) have proven the damping force in the suspension system increases the sprung-mass acceleration when the damping and spring forces are in the same direction. Therefore, in the ideal case, the damping force should turn to zero when the damping force is in the same direction as the spring force. Variable stiffness is the other approach for semi-active control. Karnopp (1983) suggested a three-parameter isolator (also called a load-leveling system), in which the damper is in a series with a high stiffness spring, whereby the equivalent stiffness changed with the change in the damping.

Assessing the damper requirement in an active suspension is a crucial stage in the damper design process. To the best of this author's knowledge, the damper force requirement in an active suspension

is not yet evaluated in the literature. Thus, in the next section, an experimental analysis is conducted in order to obtain a comprehensive performance evaluation of active suspensions utilizing linear actuators. The correlation between an active skyhook and a semi-active one is also studied in order to take advantage of the established semi-active suspension knowledge in the active damper design.

2.3.2 Experimental Setup for Active Suspension Evaluation

As shown in Fig. 2-10, an experimental test rig is developed for this Ph.D. research that consists of a 1DOF vibration isolation system mounted on a LMS722 shaker. Two accelerometers are used to measure the base and mass accelerations. The absolute displacement of the mass is measured by a LVDT, and the damping force is monitored with a load-cell (Omega-Model LC703). The sprung-mass is 1.94 kg, and the stiffness of the system is 4.6 kN/m. Therefore, the natural frequency of the system is obtained equal to 48.63 rad/s (7.74 Hz). A linear electromagnetic actuator (LinMot PS01-37x120) is used as an actuator. The linear motor used in this experiment provides 55 N of continuous and 122 N peak force. Table 2-2 provides more detailed specifications of the linear motor. The actuator is equipped with analog hall sensors for position feedback and temperature sensors for overload protection. A swept sine excitation with amplitude of 2.5 mm and a frequency range of 5 Hz (min shaker range) to 15 Hz is used to excite the system. According to definitions of the Society of Automotive Engineers, the design of a suspension system usually deals with a vibration less than 25 Hz (Hrovat, 1993).

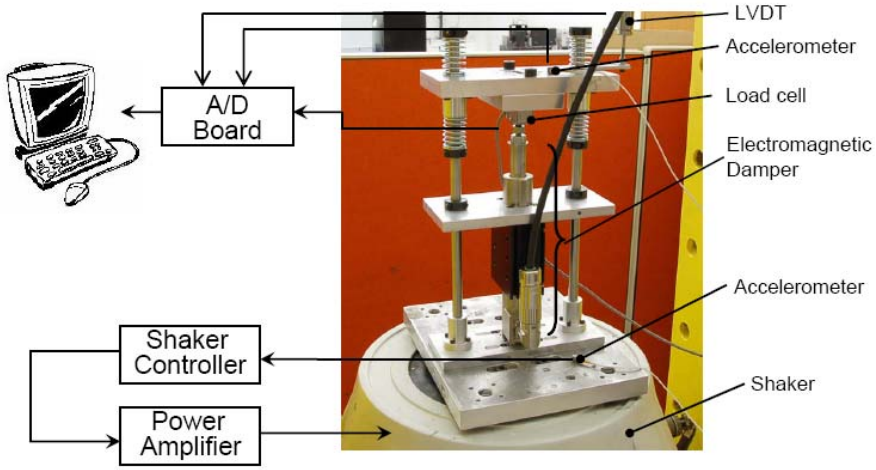

Fig. 2-10 Experimental test setup.

Table 2-2 Linear motor specifications.

Quantity	Value/Unit
Maximum stroke	100 mm
Maximum force	122 N
Slider weight	0.6 kg
Stator weight	0.74 kg

Quantity	Value/Unit
Slider diameter	20 mm
Slider length	240 mm
Stator diameter	37 mm
Stator length	216 mm

In order to have a valid comparison between the semi-active and active control strategies, the same test bed is used in both cases. The performance of the control strategies are compared based on the ride comfort index (acceleration transmissibility), considering the control effort applied by the linear actuator. As mentioned, the skyhook control is the optimal control policy in terms of its ability to isolate the suspended mass from the base excitations (Karnopp, 1995). Thus, among different proposed control strategies, the skyhook control policy is selected and applied in two different cases: active continuous and semi-active on-off modes. The active continuous skyhook is implemented based on (2-2), while the semi-active version is realized using (2-3). Fig. 2-11 shows the actuator force for the active and semi-active control policies.

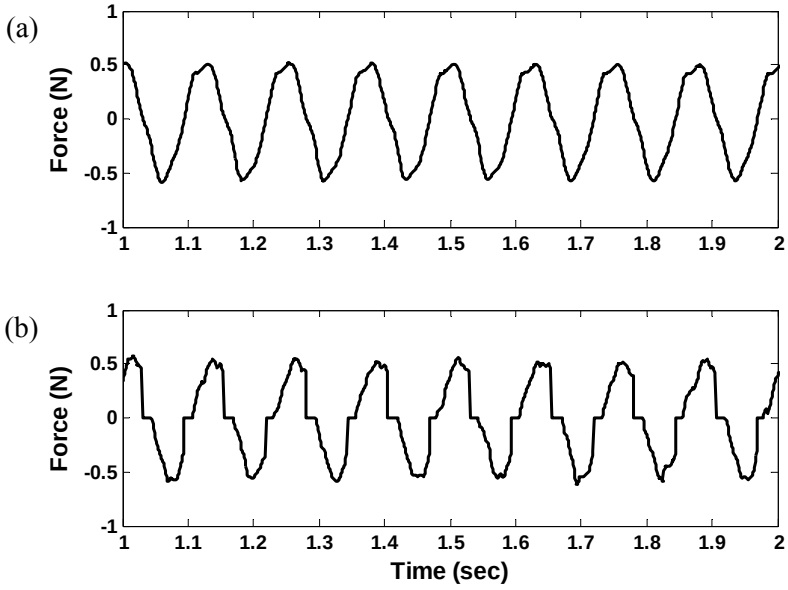

Fig. 2-11 Control effort for different skyhook strategies: (a): Active continuous and (b): semi-active skyhook.

The relative velocity $(\dot{x}_s - \dot{y})$ is obtained by differentiating the measured relative displacement between the moving mass and the base, while the relative displacement is measured by the motor's internal hall sensors. However, the absolute velocity of the sprung-mass $\dot{x}_s$, is practically measured by integrating the acceleration of the sprung-mass, and passing the result through a high-pass filter to remove the DC offset. Shen (2005) suggested the use of sprung-mass's jerk $\dddot{x}_s$, obtained from differentiating the filtered mass acceleration instead of the absolute mass velocity. Apparently, for a sinusoidal input, the phase different between $\ddot{x}_s$ and $\dot{x}_s$ is equal to π, so the control policies should be modified for using the jerk term.

In order to compare the performance of the semi-active and active skyhook policies, the control effort applied by the linear motor and the ride comfort performance is plotted in Fig. 2-12. Although the amplitude of the resonant peak is reduced by increasing the damping rate in semi-active mode, a higher damping rate causes larger deviation at a high frequency rate.

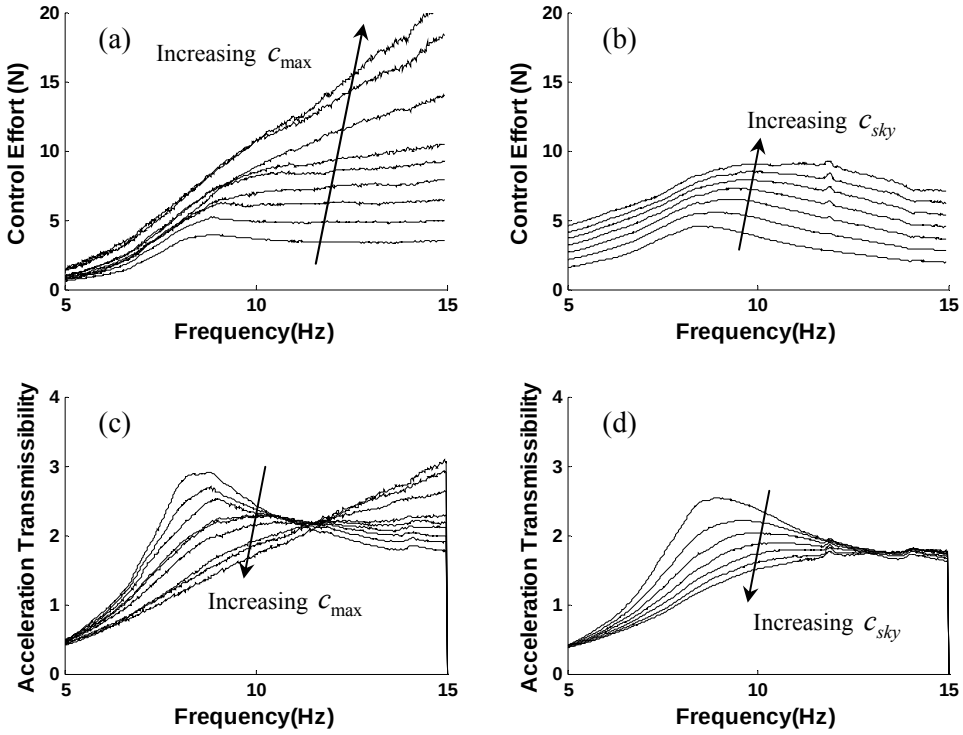

Fig. 2-12 Control effort and acceleration transmissibility obtain from (a) and (c): the semi-active skyhook, (b) and (d): the active continuous skyhook.

In contrast to the active skyhook, the applied force in the semi-active mode is significantly increased at higher frequencies, comparing the control efforts in Fig. 2-12(a) and (b). As also seen in Fig. 2-12(c), the high frequency isolation problem cannot be thoroughly addressed with the semi-active skyhook strategy. It should be mentioned that these results are obtained with the assumption that the semi-active damper is capable of providing the zero damping force when it is required, so the real case scenario with semi-active dampers has a lower performance in terms of acceleration transmissibility and the required control effort. As perceived from experimental results in Table 2-1, there is a minimum practical damping coefficient which is considerably high, especially in the case of MR-fluid dampers.

Considering the road-handling index, a similar trend to the ride comfort is occurred. Sharp and Hassan (1986) show that when control laws for the quarter-car system are chosen with a high weighting on the road-handling index, the semi-active systems lose ground in comparison with their active counterparts. In addition, in the case of the semi-active mode, the force discontinuity shown in Fig. 2-11(b) creates jerks during the switch transition (Lane, 1990).

To compare the semi-active with active skyhook modes, the situation in which the two polices are transmitting similar acceleration to the mass is considered, as shown in Fig. 2-13(c) and (d). It is inferred from Fig. 2-13(a) and (b) that to achieve a similar performance at the resonant frequency of the system, 35% lower control force is required, when using the active skyhook strategy compared to the semi-active one. This ratio increases at higher frequencies, which means that the linear actuator with the active control strategy is required to produce even less damping force at higher frequencies.

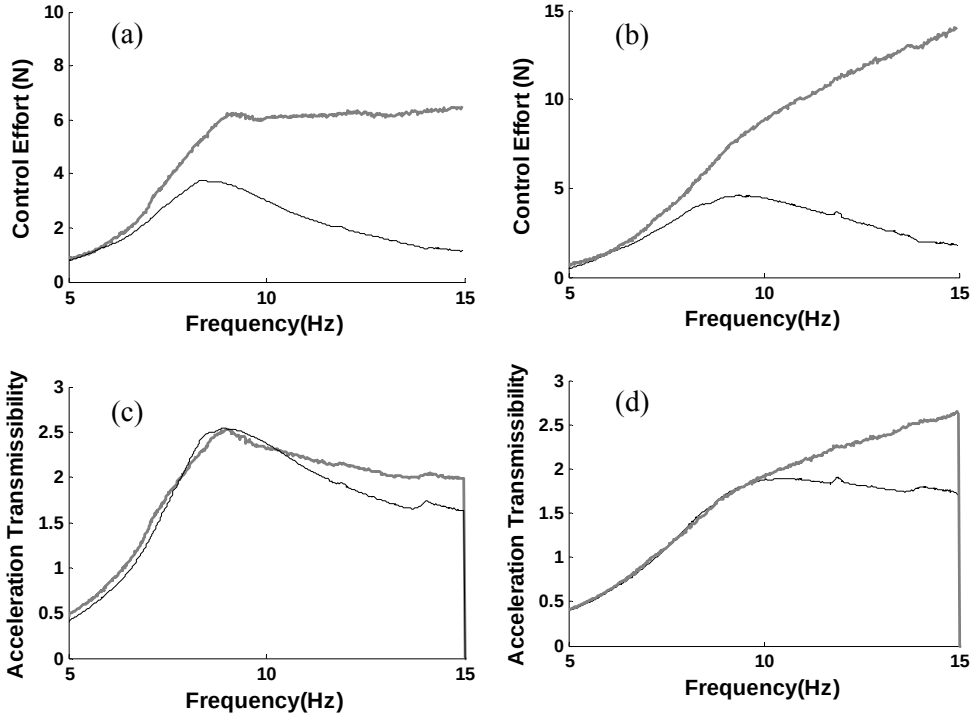

Fig. 2-13 (a), (b): Control effort, (c) and (d) Acceleration Transmissibility comparison for two different control polices. ——: Active continuous skyhook and ——: semi-active on-off skyhook.

2.4 Design Requirements and Criteria

So far in this chapter, the semi-active damper technologies have been assessed through experimental analysis, and a reliable comparison in terms of control effort and performance has been conducted between active and semi-active control strategies. In this section, the force and damping requirements as well as the dimension restrictions are characterized as design criteria for the damper design to be used in active and passive suspension systems. These requirements are established, utilizing the derived results from previous sections.

2.4.1 Force and Damping Characteristics

Vehicle suspension systems are exposed to a wide range of input disturbance frequencies due to road irregularities. Resonant frequencies of the two suspension subsystems including sprung and unsprung-masses are the most important working points regarding comfort and safety when choosing

design requirements/parameters. Sprung and unsprung-masses natural frequencies are roughly 1 and 9 Hz, respectively.

Dealing with active suspension systems, the two main design criteria are the required actuator force level and power consumption. Both of these criteria are corresponded to standard road conditions and acceptable acceleration range for passengers. The ISO 2631 standard sets the acceptable time period exposure of a passenger experiencing vertical and lateral acceleration within the range of 1 to 80Hz. Human reaction to vibration below 1 Hz and above 80 Hz is extremely variable and depends on a large number of external factors. The ISO standard on *Whole Body Vibration* (WBV) exposure is directed into three categories of health effects: *reduced comfort*, *fatigue-decreased proficiency*, and *exposure limits*. Reduced comfort is applicable where passenger comfort is of concern. The fatigue-decreased proficiency boundary is applied to situations where maintaining driver efficiency is of concern. Exposure limits applies to situations where driver health and safety may be compromised by chronic injuries to the back, neck, and internal organs (Levy *et al.*, 2005).

The vibration levels shown in Fig. 2-14 are indicated in terms of RMS acceleration levels, representing fatigue-decreased proficiency. An upper boundary for acceptable exposure time to vibration is twice as high as for fatigue-decreased proficiency, while the reduced comfort boundary is assumed to be one-third of the stated levels. Drivers start feeling uncomfortable at these vibration levels. Simulations done by Martins *et al.* (2006) showed the reduced comfort time boundary, where the sum of two sinusoidal waves were fed as the input disturbance to the system shown in Fig. 1-1(b). Table 2-3 depicts these results for the reduced comfort boundary. The simulation frequencies were set as the sprung and unsprung-mass resonance frequencies. Based on these simulations, a passive damper should be able to exert a RMS damping force of ~1040 N at the RMS velocity of ~0.7 m/s, *i.e*. the average passive damping coefficient of ~1480 Ns/m.

Table 2-3 Simulation results for the reduced comfort boundary (Martins *et al.*, 2006)

Input Disturbances	Reduced Comfort Time Boundary	Max. Stroke	Peak Force	RMS Force
1.2 Hz 3.5 cm/9 Hz 1.5 mm	1 hour	80 mm	900 N	451 N
1.2 Hz 8.5 cm/9 Hz 2.5 mm	1 min	160 mm	2000 N	1040 N

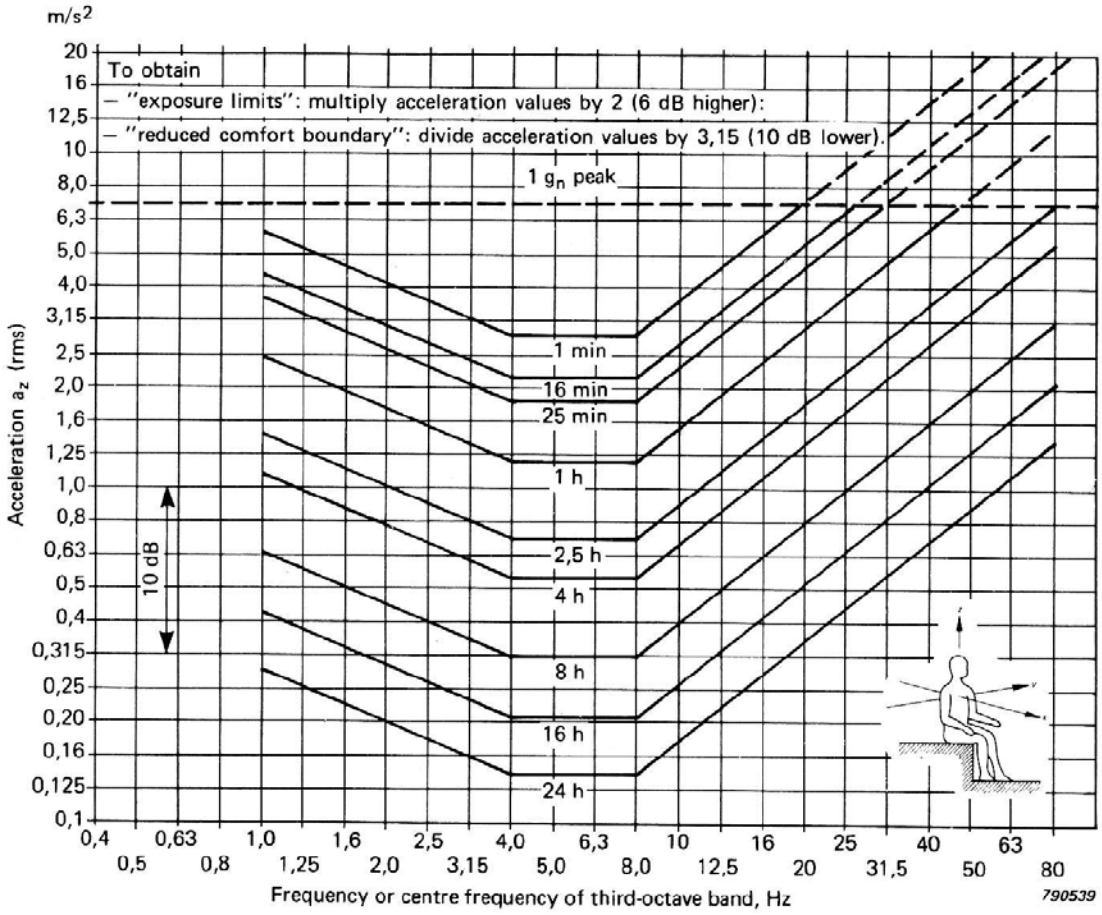

Fig. 2-14 Vertical vibration exposure criteria levels defining equal fatigue-decreased proficiency boundaries (ISO 2631, 1978).

The results obtained from Section 2.2 shows that for the semi-active MR dampers, the average damping coefficient in compression/extension stages for peak velocities below 1 m/s and applied voltage below 1 V is ~1500 Ns/m. Similarly, for the solenoid-valve damper this average value is obtained as 2300 Ns/m for the applied voltage below 3 V. Therefore, for a passive damper in a midsize vehicle, the required mean damping coefficient in the range of 1500-2000 Ns/m is accepted.

It should be noted that the required force values in Table 2-3 reflect passive suspension performance, and force requirements should be modified for a hybrid damper. As mentioned in Section 2.3.1, skyhook control is the optimal control strategy in terms of its ability to isolate the sprung-mass from the base excitation (Karnopp, 1995). Based on the skyhook active control strategy,

the actuator force should be proportional and in the opposite direction to the absolute sprung-mass velocity. So the total hybrid damper force, F_H, acting on the sprung-mass in a 1DOF model is

$$F_H = -c_p(\dot{x}_s - \dot{y}) - C\dot{x}_s\,, \tag{2-4}$$

where C is the active skyhook force coefficient. The term $C\dot{x}_s$ corresponds to the required active force in a hybrid system. The two coefficients, respecting the passive an active damping coefficients, should be carefully selected for each particular vehicle.

One of the key parameters in hybrid damper design is the ratio of the passive damping force to the active electromagnetic force. Martins *et al.* (1999) showed that for a hybrid vehicle suspension system, 5-to-1 is a good choice for the ratio of peak passive damping force to peak electromagnetic active force. Based on this ratio, the peak passive damping force and the peak electromagnetic active force are obtained as 1650 and 350 N, respectively. Considering the peak relative velocity of 1.2 m/s (Martins *et al.*, 1999) the required passive damping coefficient of 1400 Ns/m is obtained for a hybrid damper. The hybrid damper force and damping coefficient requirements, resulting from Table 2-3, are listed in Table 2-4.

Based on the derived experimental results in Section 2.3.2, for an active system, the maximum required damping force is more than 35% less than the aforementioned 2000 N peak value in Table 2-3, *i.e*. the maximum required damping force in a fully active system is less than 1300 N.

Table 2-4 Hybrid damper design parameters.

Quantity	Value
Peak force	2000 N
RMS force	1040 N
Peak active force	350 N
Peak passive force	1650 N
Passive damping coefficient	1400 Ns/m

For a passive suspension system, the best damping performance turns out to be a symmetrical behavior in compression and extension (Thompson, 1969). However, the damper's asymmetrical action appears to be advantageous in the case of large disturbances, stemming from large pot-holes, by preventing the wheel from descending too deep into the hole due to substantial damping in

extension. Also, the damper asymmetric behavior in extension/compression causes a lower vehicle height, especially at higher relative velocity of damper endings. This, in turn, has a positive effect on the vehicle stability. On the other hand, lowering the suspension system results in a smaller damper stroke in one direction, and might cause a hard stop if this parameter is not considered in the design (Eslaminasab, 2008). Typically, the passive damping has an asymmetric characteristic in extension/compression stages. So, another important parameter is the ratio of total damping in extension and compression. Although there is no general rule, for a passenger car, this ratio is around 0.4 (also express as 30%/70%) (Dixon, 1999).

2.4.2 General Dimension Data

General dimension data includes the length (distance between mountings), weight, stroke, and the external diameter of the damper. The exact dimension of the damper should be assigned based on the vehicle manufacturer and each individual vehicle. The general dimension listed in Table 2-5 could be used as typical data for damper design.

The damper weight is another important issue in the damper design, and its optimal value is corresponded to the vehicle make and overall suspension design. The fuel economy and handling quality may be influenced by the damper weight. However, for an active suspension, the lighter damper is more desirable. Although there is no limit assigned to the damper weight in the literature, it is preferable not to exceed 7 kg for each damper.

Table 2-5 General dimension data (Martins *et al.*, 2006).

Quantity	Value
Max. diameter	150 mm
Max. Length	600 mm
Stroke	160 mm

2.4.3 Other Factors

Other factors might include the operating temperature restrictions, friction, response-time, mounting method, and cost. Yabuta *et al.* (1981) included the influences of damper friction, and revealed that high levels of friction particularly decrease ride handling on smooth roads. They recommended that friction forces should be less than 40 N for a midsize car.

The response-time is an important practical aspect of controllable dampers. Rapid response time is desired for almost all real-time control applications (Koo *et al.*, 2006). The level of sensitivity of the overall suspension performance (in terms of acceleration and displacement transmissibilities) to the damper's response-time corresponds to the employed control strategy. Generally, the acceleration and displacement transmissibilities exhibit higher values (worse performance) with increasing response time (Eslaminasab, 2008). Although a proper limit for the command-switching frequency and the response time should be considered for the specific control strategy in use, a practical time-constant ~20 ms is within the reasonable range.

The cost of the damper can be minimized by avoiding exotic manufacturing techniques and materials. Material costs are estimated for developed dampers in this thesis and compared to that of commercial dampers, but manufacturing and assembly costs are beyond the scope of this research. Final design requirements for passive, active, and hybrid dampers are listed in Appendix C.

2.5 Conclusions

In this chapter, the hybrid and active damper design requirements are characterized, starting with the semi-active damper technology assessment and an experimental analysis on active suspension systems. Two variable dampers, the solenoid-valve damper of a Volvo S60 and the MR damper of a Cadillac SRX are used for the evaluation of the commercial semi-active dampers, resulting in the characterization of the semi-active dampers and obtaining their operating damping ranges. An experimental comparison in terms of control effort and damper performance was conducted between active and semi-active control strategies, revealing that to achieve a similar performance at the resonant frequency of the system, a 35% lower damping force is required when the active skyhook strategy is compared to the semi-active one. Finally, the force and damping requirements as well as the dimension restrictions are characterized as the design criteria for the damper design to be used in passive and active suspension systems (Appendix C).

Addressing the primary goal of this research as the development of hybrid electromagnetic dampers, the next two chapters deal with the eddy current damping effect and electromagnetic damper design as two essential components of a hybrid damper. The design of hybrid dampers is discussed in Chapter 5, achieving the ultimate goal of the project.

Chapter 3

Development of Eddy Current Damping Concept

Now that the damper design requirements have been assessed, the eddy current damping phenomenon as a potential source of the passive damping in hybrid dampers will be studied in this chapter. The idea is that eddy currents transform the vibration energy of the vehicle frame into heat, suppressing the vehicle body vibration. This chapter presents the comprehensive development of a novel Eddy Current Damper (ECD), utilizing design, modeling, simulation, and experimental analysis. The chapter outlines three main sections. In Section 3.1 and 3.2, the eddy current damping effect is employed to develop a Magnetic Spring-Damper (MSD) and an ECD design, respectively, for model verification and proof of concept. In the last section (3.3), a full-size ECD is designed based on the derived damper requirements in Chapter 2, and its predicted performance is compared with that of the commercial dampers, proving the applicability of the ECD in vehicle suspension systems.

3.1 First Eddy Current Spring-Damper Design

In this section, the eddy current damping effect is exploited for the development of a spring-damper, and a model of the magnetic and eddy current forces for the designed MSD is proposed. Fig. 3-1 is a schematic of the proposed system, which consists of a ring-shaped conducting Aluminum (Al) plate and two cylindrical Permanent Magnets (PMs), whose like-poles are in close proximity. The lower PM and the Al plate are stationary, while the upper magnet has a reciprocating motion. The use of a ring-shaped conductor plate simplifies the fabrication, and its thickness does not limit the magnets' air-gap. Also, the conductor's shape is appropriate for laboratory experiments that are described in Section 3.1.5.3. As described before, eddy currents are induced in a conductor either by the movement of the conductor in a static magnetic field (motional eddy currents) or by changing the strength of the magnetic field (transformer eddy currents). For this case study, the relative movement of the magnets causes the conducting plate to undergo a time-varying magnetic field such that

transformer eddy currents are generated. Since there is a relative movement between magnets and the conducting plate, motional eddy currents are induced as well.

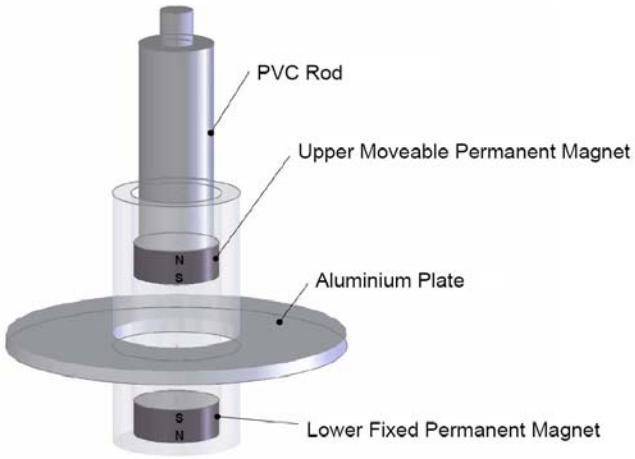

Fig. 3-1 Schematic view of the proposed magnetic spring-damper.

An analytical approach is adopted for modeling the proposed damper. Finite Element (FE) modeling and the experimental results verify the accuracy of the analytical model derived from basic electromagnetic principles. This section outlines the steps to model the proposed MSD. First, the magnetic flux density, generated by a single cylindrical PM is calculated in Section 3.1.1 by the current method (Furlani, 2001). The calculated flux density is validated with FE and experimental results, and then used for the eddy current calculation in Section 3.1.3. Next, the repulsive force between the two adjacent magnets is calculated, and the spring effect is characterized via combining the current method and Ampere's force law. In Section 3.1.5.2, the accuracy of the newly-developed force model is confirmed by the FE and experimental results. Finally, the motional and transformer eddy forces are calculated and validated by experimental results that ultimately lead to the dynamic damping modeling and analysis of the designed MSD.

3.1.1 Flux Density Calculation

There are a number of approaches for calculating the magnetic flux density of a PM (Forbes *et al.*, 1997). The simplest approach is the dipole moment model (A-23), which is more appropriate for the flux density calculation for long distances, when compared to the magnets' diameter. The charge method and the current method model the magnet with a distribution of the charge and the current, respectively (Furlani, 2001). In this section, the current model is used for modeling the PMs. Furlani

(2001) has shown that a cylindrical magnet can be replaced by an equivalent magnetic volume current density $\boldsymbol{J}_m = \nabla \times \boldsymbol{M}$ and an equivalent surface current density $\boldsymbol{j}_m = \boldsymbol{M} \times \hat{\boldsymbol{n}}$ that circulates around the body of the cylinder (It should be noted that in this thesis, the vector quantities are represented by bold letters). $\boldsymbol{M}$ and $\hat{\boldsymbol{n}}$ are the magnetization vector and unit surface normal, respectively. By assuming that the cylindrical magnet is polarized along its longitudinal direction with unit vector $\hat{\boldsymbol{z}}$ and that a uniform magnetization, *i.e.* $\boldsymbol{M} = M\hat{\boldsymbol{z}}$, the volume and surface current densities are

$$\boldsymbol{J}_m = 0,$$

$$\boldsymbol{j}_m = M\hat{\boldsymbol{\varphi}}, \tag{3-1}$$

where $\hat{\boldsymbol{\varphi}}$ is the tangential unit vector. For a cylindrical current sheet, extending between $z' = \pm\tau_m / 2$, the flux density components at (*r, z*) are given by Craik (1995) as

$$B_r(r,z)\big|_{R_m,\tau_m} = \frac{\mu_0 I}{2\pi\tau_m}\int_{-\tau_m/2}^{\tau_m/2} \frac{(z-z')}{r\left[\left(R_m+r\right)^2+(z-z')^2\right]^{1/2}}\left[-K(k)+\frac{R_m^2+r^2+(z-z')^2}{\left(R_m-r\right)^2+(z-z')^2}E(k)\right]dz',$$

$$B_z(r,z)\big|_{R_m,\tau_m} = \frac{\mu_0 I}{2\pi\tau_m}\int_{-\tau_m/2}^{\tau_m/2} \frac{1}{\left[\left(R_m+r\right)^2+(z-z')^2\right]^{1/2}}\left[K(k)+\frac{R_m^2-r^2-(z-z')^2}{\left(R_m-r\right)^2+(z-z')^2}E(k)\right]dz'. \tag{3-2}$$

$K(k)$ and $E(k)$ are the complete elliptic integrals of the first and second kind, respectively, and are defined as

$$K(k) = \int_0^{\pi/2} \frac{d\theta}{\sqrt{1-k^2\sin^2\theta}} \tag{3-3}$$

and

$$E(k) = \int_0^{\pi/2} \sqrt{1-k^2\sin^2\theta}\,d\theta, \tag{3-4}$$

where

$$k^2 = 4R_m r\left[\left(R_m+r\right)^2+(z-z')^2\right]^{-1}.$$

Parameters R_m and τ_m are the radius and thickness of the cylindrical PM, respectively, and $I = M\tau_m$ is the equivalent current of the PM (Craik, 1995). Since Eq. (3-2) does not have any analytical solution (Sodano *et al.*, 2005), a numerical approach is used for solving the integrals. The estimated values are validated by the FE and experimental results. The calculated magnetic flux density is used for the estimation of the eddy current in Section 3.1.3.

3.1.2 Magnetic Force Calculation

In this section, the repulsion force between the two adjacent cylindrical PMs is obtained by considering the magnets as two single current-carrying loops and also two solenoids, as depicted in Fig. 3-2. The force that a single current-carrying loop undergoes in the presence of another current-carrying loop is calculated by applying Ampere's force law (A-36). It states that when two current-carrying elements $I_1 d\boldsymbol{L}_1$ and $I_2 d\boldsymbol{L}_2$ interact, the elemental magnetic force, exerted by element 1 on element 2, is

$$d\boldsymbol{F}_{21} = \frac{\mu_0 I_2 d\boldsymbol{L}_2}{4\pi} \times \left[\frac{I_1 d\boldsymbol{L}_1 \times \boldsymbol{R}_{21}}{R_{21}^3} \right], \tag{3-5}$$

where $\boldsymbol{R}_{21}$ is the distance vector between the two elements, as illustrated in Fig. 3-2. R_1 and R_2 are the radii of loop one and two, respectively.

Therefore, the magnetic force is

$$\boldsymbol{F}_{21} = \frac{\mu_0}{4\pi} \int_{c2} I_2 d\boldsymbol{L}_2 \times \int_{c1} \frac{I_1 d\boldsymbol{L}_1 \times \boldsymbol{R}_{21}}{R_{21}^3} . \tag{3-6}$$

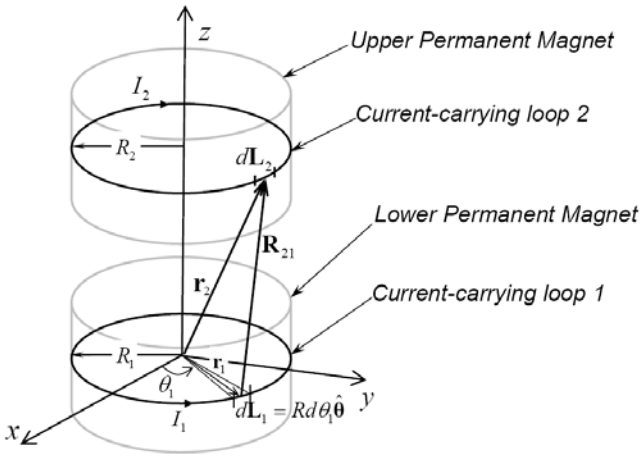

Fig. 3-2 Schematic of two current-carrying loops, illustrating the variables used in Eq. (3-5)

The right integral is the magnetic flux density produced by current-carrying loop 1 at the location of element 2. Typically, when a current-carrying loop is placed in an external magnetic field $\boldsymbol{B}$, the magnetic force of the loop is mathematically expressed as

$$\boldsymbol{F} = \int_c I d\boldsymbol{L} \times \boldsymbol{B} . \tag{3-7}$$

By assuming $R_1 = R_2 = R_m$, the vertical component of the interacting forces between two current-carrying loops with the opposite current direction is

$$F_z(z_d) = \frac{\mu_0 I_1 I_2 R_m^2}{4\pi} \int_0^{2\pi}\int_0^{2\pi} \frac{-z_d \cos(\theta_2 - \theta_1)\, d\theta_1\, d\theta_2}{(2R_m^2 - 2R_m^2 \cos(\theta_2 - \theta_1) + z_d^2)^{3/2}} , \tag{3-8}$$

where z_d is the distance between the two loops. By using the same current technique as that for the PM modeling, the vertical component of the interacting forces between the two adjacent magnets with the opposite magnetization direction is obtained by integrating (3-8) along the magnets' thickness, as follows

$$F_z = \frac{\mu_0 I_1 I_2 R_m^2}{4\pi\tau_m^2} \int_{g/2}^{g/2+L}\int_{-L-g/2}^{-g/2}\int_0^{2\pi}\int_0^{2\pi} \frac{-\left[z_d - z' - z''\right]\cos(\theta_2 - \theta_1)\, d\theta_1\, d\theta_2 dz' dz''}{(2R_m^2 - 2R_m^2 \cos(\theta_2 - \theta_1) + \left[z_d - z' - z''\right]^2)^{3/2}} . \tag{3-9}$$

Eqs. (3-8) and (3-9) are used in Section 3.1.5.2 as alternative approaches for the magnetic force estimation. It is seen that the single loop approximation of Eq. (3-8) maintains its accuracy for the wide air-gap between the magnets, but underestimates the magnetic force for the narrower air-gaps. The accuracy of the calculated repulsive force in Eq. (3-9) is verified in Section 3.1.5.2 by using the FE and experimental results. Finally, Eq. (3-9) is used to anticipate the spring behavior of the MSD device.

3.1.3 Eddy Current Damping Force Calculation

Fig. 3-3 exhibits the configuration of the eddy current damping system, where the stationary Al plate is the source of the eddy currents due to the movement of the upper PM.

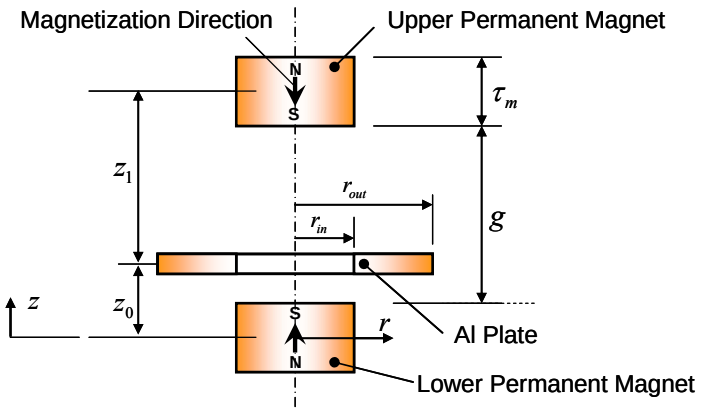

Fig. 3-3 Geometric definition of the eddy current spring-damper.

Fig. 3-4 demonstrates a 2D axial-symmetry FE simulation of the proposed system. The Comsol 3.4 software is utilized for this simulation under the magnetostatics condition, where Lagrange quadratic shape-functions are used for the triangular elements. The streamlines represent the magnetic flux density. The upper magnet in Fig. 3-4(b) is moved 10 mm closer to the lower magnet, compared to Fig. 3-4(a). This movement is equivalent to moving the Al plate with a thickness of δ and a conductivity of σ, up 5 mm. It is noteworthy that the plate velocity ($\boldsymbol{v}$) should be considered as half of the upper magnets' velocity.

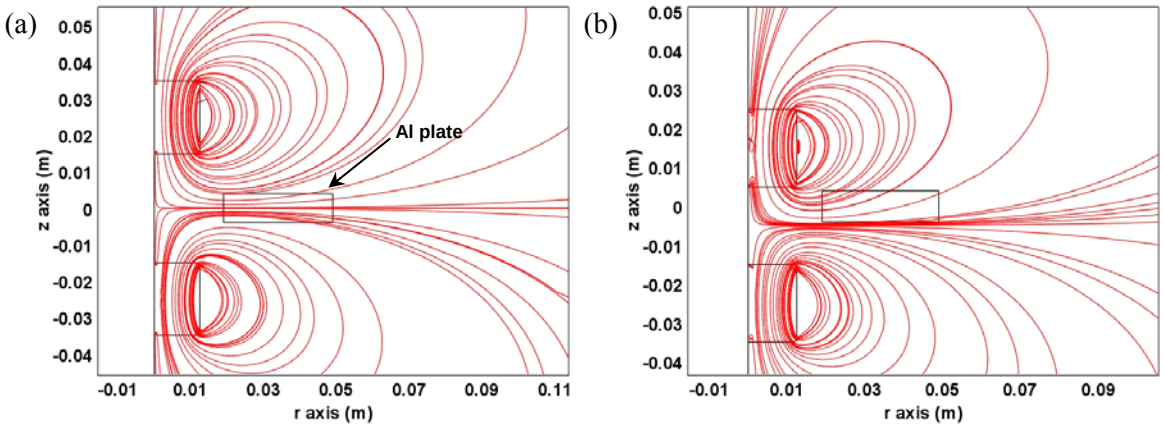

Fig. 3-4 2D axial symmetry simulation of the system by Comsol, where the air-gap is decreased from (a) 30 mm to (b) 20 mm; the streamlines represent the magnetic flux density; (other specifications are listed in Table 3-1).

As shown in Fig. 3-4, PMs generate a time-varying magnetic field in both the axial (z) and radial (r) directions. The total generated electromotive force of the Al plate is based on either a time-varying magnetic field, or the relative motion of the conducting plate. The former contribution is associated with the "*transformer emf*" and is easily obtained from the third Maxwell equation (Faraday's law), whereas the latter is associated with the "*motional emf*" and is derived from the Lorentz force law. The total induced emf is obtained by calculating

$$E = E_{trans} + E_{motional} = -\int_s \frac{\partial \boldsymbol{B}}{\partial t} \cdot d\boldsymbol{s} + \oint_c (\boldsymbol{v} \times \boldsymbol{B}) \cdot d\boldsymbol{l} \,. \tag{3-10}$$

Also, it is noted that plate velocity ($\boldsymbol{v}$) is actually the relative velocity of the conducting plate with respect to the PMs. Since the relative movement of the Al plate is in the vertical direction, the vertical component of the magnetic flux density does not contribute to the generation of the motional eddy current (*i.e.*, $\boldsymbol{v} \times \boldsymbol{B}_z = 0$). As a result, the generated motional-electromotive-force depends on the radial component of the magnetic flux density. The current density $\boldsymbol{J}$, induced in the conducting sheet due to the motional emf is:

$$\boldsymbol{J} = \sigma(\boldsymbol{v} \times \boldsymbol{B}) \,. \tag{3-11}$$

The damping force due to the motional emf term is defined (Sodano *et al.*, 2005) by computing

$$\boldsymbol{F}_{\boldsymbol{motional}} = \int_{\Gamma} \boldsymbol{J} \times \boldsymbol{B} d\Gamma = -\hat{z}\sigma\delta v_z \int_0^{2\pi} \int_{r_{in}}^{r_{out}} r B_r^2(r, z_0) dr d\theta \,, \tag{3-12}$$

where Γ, r_{in} and r_{out} are the conductor's volume, inside radius, and outside radius, respectively. As demonstrated in Fig. 3-3, the total radial component of the magnetic flux density is the sum of the magnetic flux density, generated by the two PMs at the mid-plane of the conducting plate such that

$$B_{r,total} = B_r(z_0) + B_r(z_1), \tag{3-13}$$

where

$$z_1 = \begin{cases} \tau_m + g - z_0 & if\ z_0 < \tau_m + g \\ -\tau_m - g + z_0 & if\ z_0 > \tau_m + g \end{cases}$$

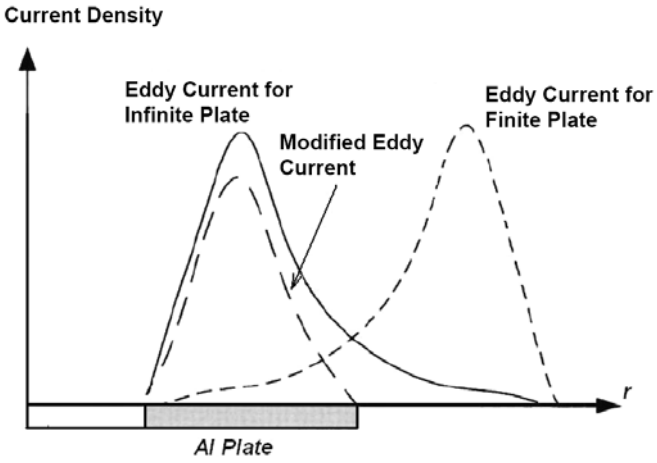

Fig. 3-5 Modification of the eddy current using the image method (Sodano *et al.*, 2006).

Eq. (3-12) is valid for only an infinite conducting plate, indicating that the boundary condition of zero current at the conducting plate's boundaries (the edge effect) is not considered. If the edge effect is not considered, the predicted force is overestimated (Sodano *et al.*, 2006). To include the edge effect, the image method (Lee *et al.*, 2002) is employed, as illustrated in Fig. 3-5. Thus, the motional eddy current force is modified by calculating

$$\begin{aligned}\boldsymbol{F}_{\boldsymbol{motional}} &= -\hat{\boldsymbol{z}}\sigma\delta v_z\left(\int_0^{2\pi}\int_{r_{in}}^{r_{out}} rB_r^2(r,z_0)drd\theta - \int_0^{2\pi}\int_{r_{in}}^{r_{out}} rB_r^2(2r_{out}-r,z_0)drd\theta\right) \\ &= -\hat{\boldsymbol{z}}\sigma 2\pi\delta v_z\left(\int_{r_{in}}^{r_{out}} rB_r^2(r,z_0)dr - \int_{r_{in}}^{r_{out}} rB_r^2(2r_{out}-r,z_0)dr\right).\end{aligned} \tag{3-14}$$

As denoted in Fig. 3-5, the first term in Eq. (3-14) corresponds to the damping force to account for the infinite plate, whereas the second term is the damping force for considering the imaginary eddy currents. The subtraction of these two terms gives the modified motional damping force. Since the magnetic field is not uniform in the vertical direction, the Al plate is prone to a magnetic flux density variation during the reciprocating oscillation. Consequently, the transformer term should be considered in the eddy current calculations.

The transformer emf is calculated by conducting numerical integration over the surface of the conductor plate as follows

$$E_{trans} = -\int_s \frac{\partial \boldsymbol{B}}{\partial t}\cdot d\boldsymbol{s} = -\int_s \left(\frac{\partial \boldsymbol{B}}{\partial z}\frac{\partial z}{\partial t} + \frac{\partial \boldsymbol{B}}{\partial r}\frac{\partial r}{\partial t}\right)\cdot d\boldsymbol{s} = -\int_s \left(\frac{\partial B_z}{\partial z}\frac{\partial z}{\partial t}\hat{\boldsymbol{z}} + \frac{\partial B_r}{\partial z}\frac{\partial z}{\partial t}\hat{\boldsymbol{r}}\right)\cdot d\boldsymbol{s}, \tag{3-15}$$

where the second term in the last integral is zero, by considering the symmetry of the radial flux density about the plate center axis. The calculated gradient of the magnetic flux density on the bottom surface is reduced from that of the upper one, since their respective normal units are in the opposite directions. Therefore, the damping force generated by the transformer eddy currents, is calculated from the respective electromotive force (E_{trans}) as follows:

$$\boldsymbol{F}_{trans} = \frac{-\hat{\boldsymbol{z}}\sigma}{l}\int_s \frac{\partial \boldsymbol{B}}{\partial t}\cdot d\boldsymbol{s}\int rB_r d\Gamma = \frac{-\hat{\boldsymbol{z}}\sigma v_z}{l}\int_s \frac{\partial B_z}{\partial z}d\boldsymbol{s}\int rB_r d\Gamma, \tag{3-16}$$

in which $l = \pi(r_{out} + r_{in})$. Thus, Eqs. (3-14) and (3-16) provide the motional and transformer damping force estimation, and the total damping force is validated in Section 3.1.5.3 by experimental results.

3.1.4 Experimental Analysis

Two experimental setups are established to validate the accuracy of the three developed models in Sections 3.1.1-3.1.3. The MSD in Fig. 3-1 is fabricated and tested, as shown in Fig. 3-6 and Fig. 3-7.

The physical properties of the newly-developed prototype are listed in Table 3-1. The PMs in this experiment are Neodymium-Iron-Boron rare earth magnets ($Nd_2Fe_{14}B$) with a radius of 25 and thickness of 20 mm.

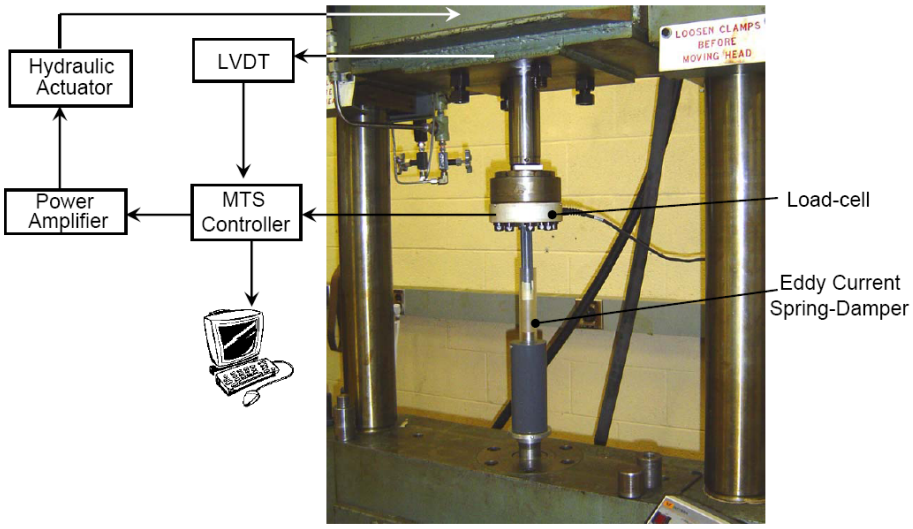

Fig. 3-6 First experimental test-bed for large amplitudes and low frequencies.

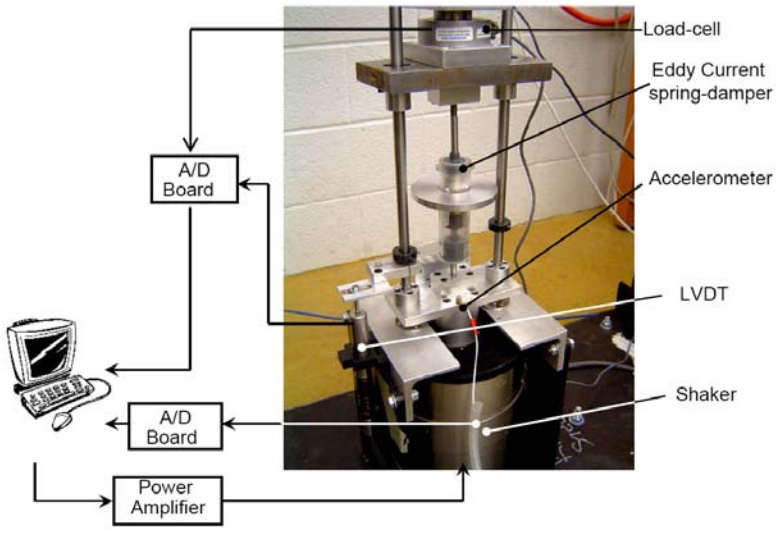

Fig. 3-7 Second experimental test-bed for small amplitudes and high frequencies.

The prototype frame, as well as the rod connecting the upper PM to the load-cell, is composed of PVC to avoid interference with the magnetic field. The first test-bed in this experiment is composed of a hydraulic shaker with feedback from a LVDT displacement sensor, a 1 klb load-cell (Omega

model LCHD) and an MTS-FlexTest-SE controller device. This system is particularly appropriate for large displacement strokes (more then 5 mm) and static force measurements. The hydraulic shaker covers the frequencies as high as 5 Hz at 15 mm displacement amplitude. Fig. 3-6 reflects the first experimental test-bed to verify the MSD's spring effect.

Table 3-1 Physical properties of the experimental configuration.

Property	Value
Aluminum electrical conductivity	3.37e7 S/m
Inside diameter of Al plate	38 mm
Outside diameter of Al plate	100 mm
Thickness of the Al plate	8 mm
Permanent magnet diameter	25 mm
Permanent magnet thickness	20 mm
Magnetization of the permanent magnet	1.03e6 A/m
Permanent magnet composition	NdFeB grade 42

As seen in Fig. 3-7, the second experimental test-bed is prepared, achieving higher accuracies for small amplitudes and high frequencies. The setup consists of a VTS electromagnetic shaker, which is controlled by accelerometer sensor feedback data. Load-cell data, as well as LVDT displacement data, is captured by another A/D board. The electromagnetic shaker is capable of producing amplitudes up to 3 mm and a force up to 100 lbf. All of the measurements are carried out at the University of Waterloo.

3.1.5 Comparison of Analytical and Experimental Analysis

In the experimental setups, the accuracy of the proposed model is verified. Before the eddy current damping force is established, the magnetic flux density and the force, generated by the PMs, are calculated and verified by experimental results.

3.1.5.1 Verification of the Magnetic Field Model

Since Eq. (3-2) does not have an analytical solution (Sodano *et al.*, 2005), it is numerically integrated. Fig. 3-8 shows the verification of the vertical component of the magnetic flux density along the magnet's centerline with the experimental results and the FE results, obtained from Comsol 3.4

software. For the FE results, the Lagrange-quadratic shape-functions for triangular elements are used to solve the PDE equations (A-15). As it is inferred from Fig. 3-8, the proposed analytical model is reliable and is used for the eddy current estimation in Section 3.1.5.3.

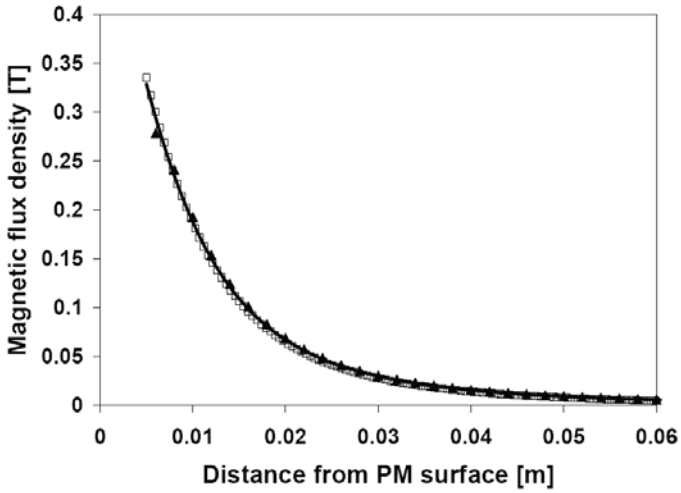

Fig. 3-8 Vertical component of the magnetic flux density along the magnet's centerline. □: FE results, —: theoretical results, ▲: experimental results.

3.1.5.2 Verification of the PM's Interaction Force Model

The force equations for both the single loop approximation (3-8) and solenoid electromagnet approximation (3-9) for simulating the PMs are derived. Fig. 3-9 gives the results of these two approximations, compared with the FE results. It is observed in Fig. 3-9 that the single current-carrying loop method (3-8), in which the PM is modeled as a single current-carrying loop at the middle of the magnet's thickness, deviates from the solenoid approach (3-9) and the FE results for the air-gap between the magnets below 3 cm. It is revealed that modeling the PM with a single current-carrying loop is no longer valid for narrow gap distances between the magnets.

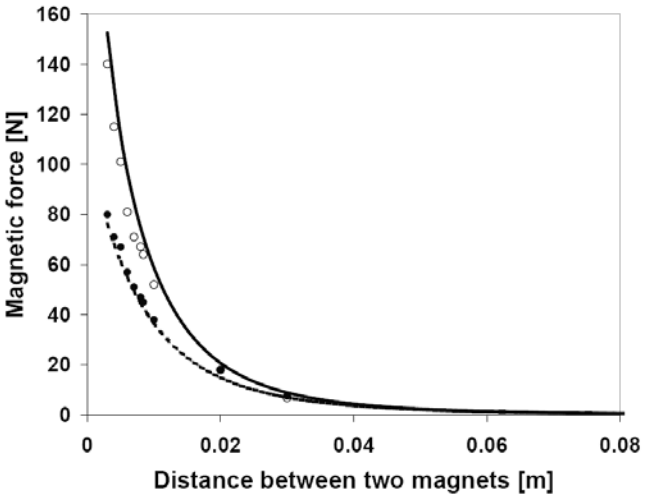

Fig. 3-9 Analytical and FE results comparison for the interaction force between two magnets. — —: Analytical solution for a single loop, ——: analytical solution for a solenoid, ●: FE solution for a single loop, ○: FE solution for PM.

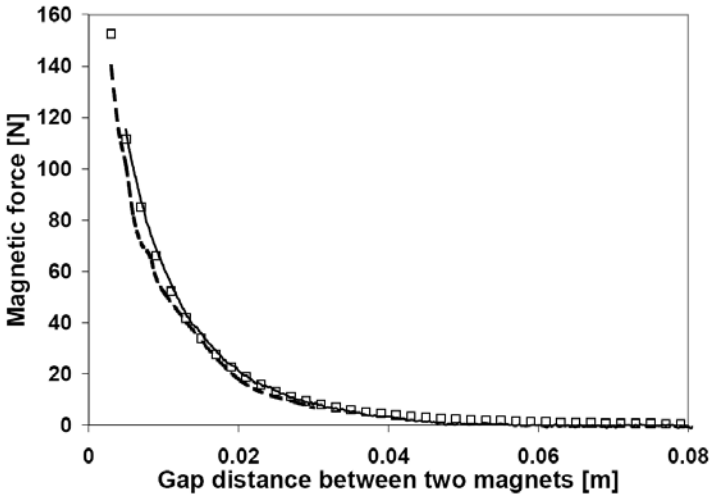

Fig. 3-10 Comparison of the experimental results and the analytical results. ——: Experimental force, □: analytical solution for a solenoid, — —: FE solution for PM.

By using the first test setup in Fig. 3-6, the magnetic force between the two adjacent PMs is experimentally measured. Fig. 3-10 signifies the accuracy of the proposed model, compared with the experimental results. Also, it is observed that a force, as high as 150 N can be achieved when the

magnets' air-gap is close to 5 mm. This graph also conveys the nonlinear spring characteristic of the system in the absence of the Al plate.

3.1.5.3 Validation of Eddy Current Model

There are a number of factors that can affect the damping ratio, and they can be varied to attain the desirable damping characteristics. In this section, the effect of the air-gap between the magnets, Al plate size and position are considered. As mentioned in Section 3.1.3, the time-varying magnetic field, and the relative motion of the Al plate and PMs produce two different effects, causing the opposing eddy force. Fig. 3-11 denotes the motional and transformer effects contributing in the damping generation at the different size air-gaps between the magnets. It is observed that for vibration amplitude equal to 5 mm, the transformer eddy current contribution is 25% less than that of the motional eddy currents. This contribution varies in relation to the position and thickness of the Al plate. The plate is positioned in the middle of the air-gap between the magnets in Fig. 3-11. The amplitude and frequency of the upper magnet oscillation are 5 mm and 10 Hz, respectively.

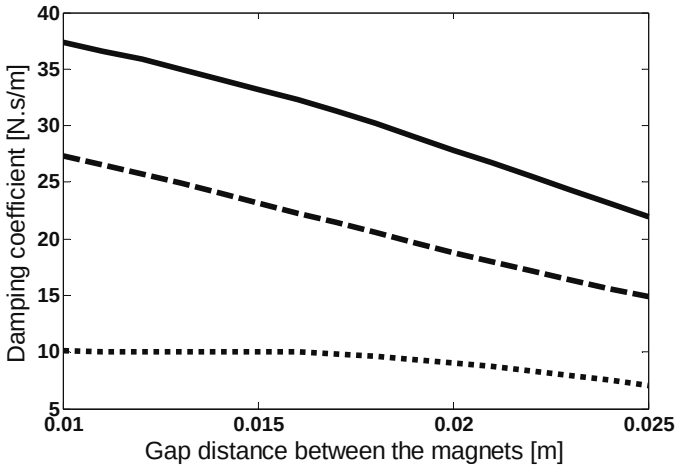

Fig. 3-11 Transformer, motional and total eddy current damping versus distance between the magnets, where Al plate is located at mid-distance of the magnets and the upper magnet peak velocity is 0.3m/s. — —: Motional eddy current effect, ▪▪▪▪▪: transformer eddy current effect, ——: total effect.

As illustrated in Fig. 3-11, the total damping effect decreases for the wider air-gap distance between the two magnets. Consequently, the desired damping ratio is achieved by choosing the gap

distance between the magnets. The opposing eddy force, generated by eddy current effect, is also calculated for the different plate positions. Fig. 3-12 shows the analytical and experimental values for the damping coefficient at different Al plate positions (z_0), when the upper magnet peak velocity is 0.25 m/s and the air-gap between the magnets is 30 mm. The Al plate positions are measured from the mid-plane of the lower PM.

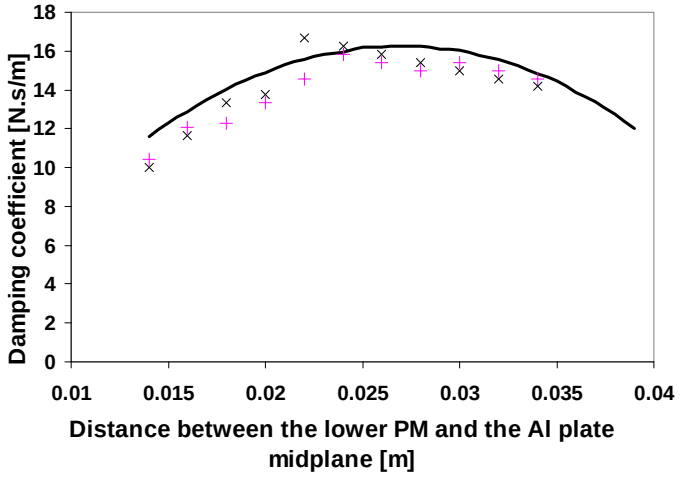

Fig. 3-12 Maximum eddy force at different conductor sheet positions, where the upper magnet peak velocity is 0.25 m/s and magnets gap is 30 mm. ×: Experimental result 1, +: experimental result 2, ——: analytical result.

It is observed that the most effective position for the Al plate is midway between the two PMs. A comparison of the two sets of experiments with the analytical solutions shows an RMS error of 1.05 kg/s (7.5%) in the damping coefficient estimation.

The size of the conducting plate is optimized as exhibited in Fig. 3-13. It is observed that increasing the outside radius of the Al plate does not affect the damping coefficient after a certain level and so there is an optimal outside radius for each case to obtain the maximum damping coefficient. This figure is obtained for a 20 mm gap between the magnets, and the upper magnet oscillation amplitude and frequency are 5 mm and 10 Hz, respectively. Each line represents the specific Al plate position (z_0), measuring from the mid-plane of the lower magnet.

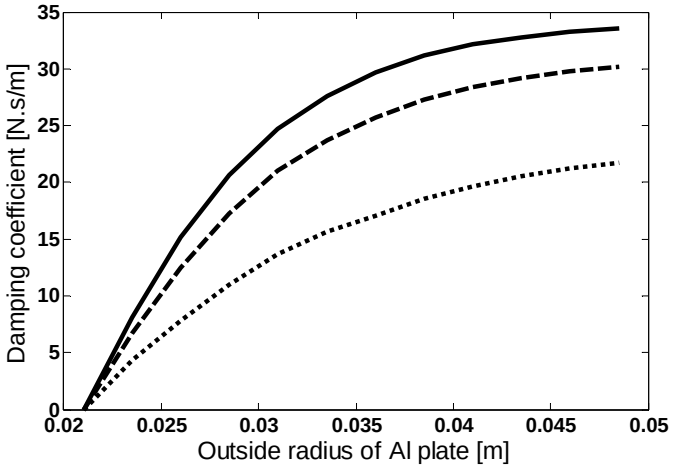

Fig. 3-13 Damping coefficient versus outside radius of the Al plate, where the magnets' gap is 0.02 m, and the upper magnet peak velocity is 0.3 m/s. ——: $z_0 = 0.02$ m, — —: $z_0 = 0.018$ m, ▪▪▪▪▪: $z_0 = 0.014$ m.

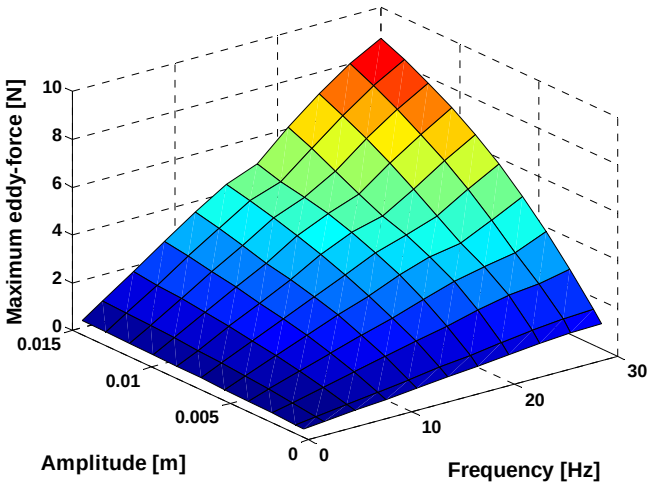

Fig. 3-14 Maximum eddy force at different vibration frequencies and amplitudes.

Fig. 3-14 signifies the maximum value of the eddy current's opposing force at different frequencies and amplitudes. It is observed that the damping characteristic of the eddy currents is similar to the linear viscous damper for the range of frequencies and amplitudes in Fig. 3-14. Also, the linear dependency of the force on the frequency at a low speed is confirmed by Canova *et al.* (2003). In

addition, it is shown that a maximum damping force up to 10 N is achievable by using the specified dimensions. Figs. 13 and 14 illustrate the analytical results of Eqs. (3-14) and (3-16).

In summary, a passive magnetic spring-damper system is developed by using the eddy current damping effect. Then, a theoretical model of the proposed system is constructed by using the transformer eddy current contribution and the image method for the motional eddy current estimation. Finally, the magnetic flux, interaction force of the magnets, and eddy current damping force are analytically calculated and validated by FE and experimental results.

The newly-developed analytical model offers a comprehensive insight into the eddy current damping phenomenon, and could be used to design high-performance dampers for a variety of applications. The damping characteristic of the proposed system can be easily changed by either re-positioning the conductor or choosing the appropriate conductor size and the air-gap distance between the magnets. The novel MSD described in this section is a non-contact device with adjustable damping characteristics, no external power supply requirement, and suitable for different vibrational structures for high accuracy and simple implementation.

3.2 Second Eddy Current Damper Design

After the development of the first eddy current damper design, the next step is to utilize the obtained perspective, and proceed with an optimal topology and design for the eddy current damper to be used in vehicle suspension applications. The very first modification is to intensify the magnetic flux density that is perpendicular to the conductor, and continue with an optimal magnets and conductor configuration. Fig. 3-15 depicts a schematic configuration of the proposed system, which consists of a conductor as an outer tube, and an array of axially-magnetized, ring-shaped PMs, separated by iron poles as a mover. The relative movement of the magnets and the conductor causes the conductor to undergo motional eddy currents.

This section describes the development of the proposed modified topology as the second eddy current damper design, and outlines the following steps to evaluate the proposed ECD. First, an analytical model is developed to estimate the damping force, generated by the induced eddy currents, for the proposed configuration. Then, a prototype ECD is fabricated and the developed model is verified by frequency/time domain analyses. Finally, the heat transfer through the conductor is investigated to complete the energy flow study.

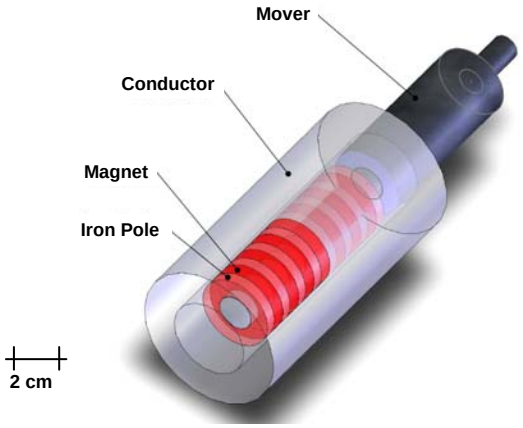

Fig. 3-15 Schematic view of the proposed ECD.

3.2.1 Analytical Damper Modeling

Fig. 3-16 illustrates the proposed ECD configuration. The direction of the magnetization for each PM is indicated by the bold arrow.

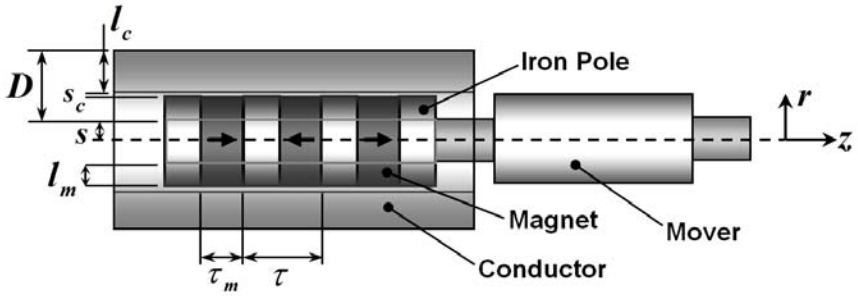

Fig. 3-16 Configuration of the proposed ECD.

The assembly comprises the tubular design, which has less leakage flux comparing to the flat design, and is vastly better for utilizing the magnetic flux, leading to higher eddy current generation. Axially-magnetized PMs in the mover result in a higher specific force capability than that of radially-magnetized ones (Wang *et al.*, 2004). Annularly-shaped magnets, supported by a non-ferromagnetic rod, are selected instead of disk-shaped magnets, and fastened onto a nonmagnetic rod, reducing the effective air-gap. Due to the relative motion of the PMs, the eddy current is generated in the conductor. As mentioned in the previous section, the eddy current phenomenon occurs either in a steady conductor in a time-varying magnetic field, or in a conductor that moves in a constant

magnetic field, calling transformer and motional eddy currents, respectively. Since the magnetic field is not changing as a function of time, there is only the motional emf as the source of eddy currents.

Fig. 3-17 depicts the schematic configuration of the PMs in the proposed design. The damping force for each pole in the *z*-direction, caused by the motional emf, is obtained using (3-12) as

$$\boldsymbol{F} = \int_{\Gamma} \boldsymbol{J} \times \boldsymbol{B} d\Gamma = -\hat{\boldsymbol{z}}\sigma(\tau - \tau_m) v_z \int_0^{2\pi} \int_{r_{in}}^{r_{out}} r B_r^2(r,z) dr d\theta \,, \tag{3-17}$$

where r_{in}, and r_{out} are the conductor's inside radius, and outside radius, respectively. τ and τ_m are the pole pitch and the magnets' thickness. In conclusion, the equivalent constant damping coefficient, *C*, for the proposed eddy current damper is obtained as:

$$C = \sigma \int_{\Gamma} B_r^2 d\Gamma \,. \tag{3-18}$$

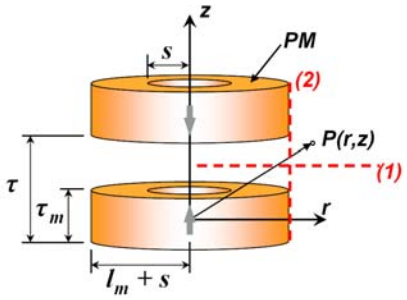

Fig. 3-17 Schematic view of two PMs with like poles in close proximity.

Among different proposed approaches for calculating the magnetic flux density of a magnet, the model proposed by Craik (1995) is used for the magnetic flux density calculations as it offers an accurate model with a reasonable complexity. For a PM with thickness τ_m and radius R_m, the magnetic flux density at distance (*r, z*) from the PM geometric centre is obtained by computing (3-2). For the PMs, the axial magnetic fluxes, along the dashed line 1, in Fig. 3-17, cancel each other, whereas the two radial fluxes are combined to produce a radial magnetic flux that is exactly twice as high as the one produced by a single magnet. Therefore, the total radial component of the magnetic flux density, B_r along the dashed line 1 is given by

$$B_r = 2\left(B_r(r,z)\big|_{l_m+s,\tau_m} - B_r(r,z)\big|_{s,\tau_m} \right). \tag{3-19}$$

A numerical approach is adopted for solving the integrals (3-2), and the calculated values are validated by both the FE analysis and experiments, as indicated in Section 3.2.4.

The effect of the bounded conductor plate, modeled in (3-14), is neglected, due to its negligible contribution in the total damping force. However, Eq. (3-17) could be additionally modified to accommodate another effect, called the skin effect. This effect is the tendency of an alternating current in a conductor to be distributed such that the current density at the conductor surface is greater than the density at the core. The skin effect causes the effective conductor's resistance to increase with the current frequency. The current density in a thick conductor plate decreases exponentially with depth d_s from the surface, and is represented by

$$J = J_S e^{-d_s/\delta_p}, \tag{3-20}$$

where J_s and δ_p are the current at the surface and the depth of penetration, respectively. The depth of penetration is defined as the depth below the conductor surface at which the current density decreases to $1/e$ of the current at the surface, and is obtained from

$$\delta_p = \sqrt{\frac{1}{\sigma \pi \mu_a \omega}}, \tag{3-21}$$

where ω is the frequency of the alternating current, and μ_a is the absolute permeability of the conductor equal to $\mu_0 \mu_r$ (μ_r is the relative permeability of the conductor). Equation (3-17) is modified to accommodate the described skin effect as follows:

$$F = 2\pi\sigma(\tau - \tau_m) v_z \int_{r_{in}}^{r_{out}} r B_r^2 e^{\frac{-(r-r_{in})}{\delta_p}} dr, \tag{3-22}$$

Equation (3-22) is computed for the damping force estimation of the proposed ECD configuration. In the next section, the geometry of the proposed ECD is optimized to obtain the highest damping force, regarding the external and internal dimension restrictions and the manufacturing limitations.

3.2.2 Sizing of the Proposed Topology

In order to verify the derived analytical model of the damper, the dimensions of the prototype ECD are set. The conductor external radius (D+s), inner rod radius (s), and air-gap thickness (s_c) are selected as 25 mm, 6.25 mm, and 0.5 mm; they can be carefully selected for each specific application based on the external size restriction, mechanical stress consideration, and manufacturing restrictions, respectively. The conductor thickness (l_c) is obtained such that it is equal to the eddy current depth of penetration at the highest working frequency. From (3-21), the depth of the penetration at 30 Hz is obtained, 12 mm. By considering the restricted external radius and l_c=12 mm, the ring-shaped magnets' diameter (2(l_m+s)) of each magnet is calculated as 25 mm. The outward magnetic flux from each pole is estimated by

$$\phi_g = 2\pi(l_m + s)(\tau - \tau_m)B_r, \tag{3-23}$$

where B_r is calculated from (3-19). Fig. 3-18 reflects the variation of this outward magnetic flux in terms of the normalized magnetic thickness.

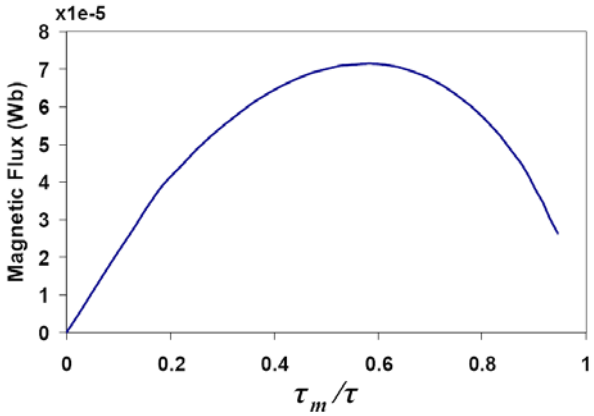

Fig. 3-18 Magnetic flux vs. normalized magnet thickness.

It is observed that the maximum flux is obtained at τ_m / τ equals to 0.55. Consequently, the magnets' thicknesses have an optimal value of 5 mm by assuming pole pitch τ is 9 mm. After the ECD dimensions are set to obtain the highest radial flux in the air-gap, and thus, the highest damping force, an experimental analysis is conducted in the next sub-sections, and the results are employed to validate the derived model.

3.2.3 Finite Element Modeling

To validate the developed analytical model for magnetic flux density, a 2D axisymmetric model of the mover is analyzed by using Comsol 3.4 under the magnetostatic condition. Fig. 3-19 shows the 2D model of the proposed mover configuration in Fig. 3-16. The magnetic flux density streamlines and the induced magnetic field are plotted in this figure.

It is observed that the radial magnetic flux density is concentrated and enhanced at the iron pole pieces, causing a greater eddy current induction such that the ECD is more effective. The agreement between the numerical FE, analytical and the experimental results is indicated in Fig. 3-21 and discussed in the next section.

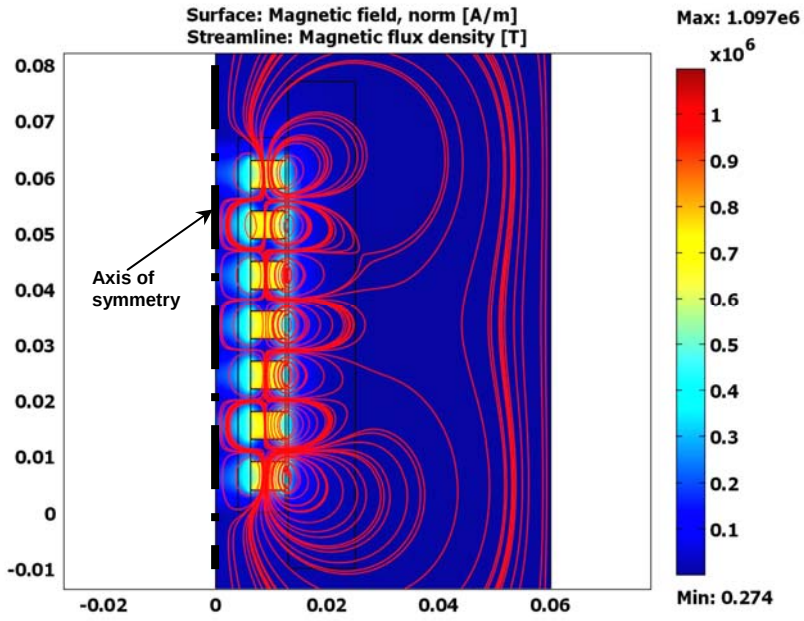

Fig. 3-19 2D axisymmetric FE simulation of the ECD prototype.

3.2.4 Experimental Analysis

3.2.4.1 Experimental Setup for Magnetic Flux Measurements

After the initial sizing in Section 3.2.2, a prototype ECD is fabricated and experiments done to verify the accuracy of the analytical model for the magnetic flux density (3-19) as well as the force model

(3-22). Fig. 3-15 provides a schematic view of the novel ECD, which is fabricated and tested. Its dimensions are obtained in Section 3.2.2 and listed in Table 3-2.

Table 3-2 ECD prototype dimensions.

Item /Symbol	Value/Unit
Number of poles p	8
Pole pitch τ	9 mm
Magnets' thickness τ_m	5 mm
Rod diameter $2s$	12.5 mm
Magnets' diameter $2(l_m + s)$	25 mm

Item /Symbol	Value/Unit
Air-gap s_c	0.5 mm
Conductor external radius	25 mm
Conductor thickness l_c	12 mm
Magnets' material	Nd-Fe-B B_r=1.17 T

Fig. 3-20 denotes the experimental setup, which is used for the magnetic flux measurements. The gaussmeter (LS410) is used to measure the magnetic flux density. The gaussmeter probe is moved to the desired position by an Epson SCARA robot. The radial magnetic flux density is measured at 0.5 mm incremental steps along the mover's length.

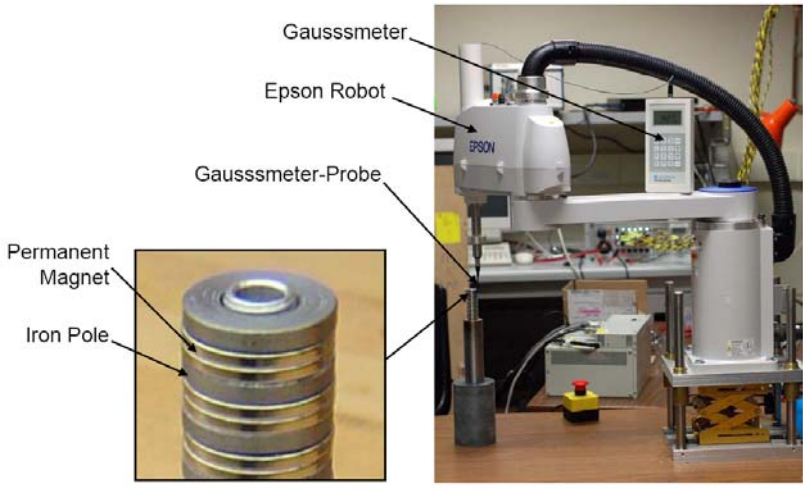

Fig. 3-20 Experimental setup for the magnetic flux measurements.

Fig. 3-21(a) exhibits the radial component of the magnetic flux density along horizontal line 1 in Fig. 3-17 at the mid-distance of the air-gap, obtained from the analytical, as well as the FE results. In addition, the FE results are verified by the experimental results for the case in which the iron pole is

inserted between the two magnets. The magnets and the conductor boundaries are added, providing more clarity. The data are captured from the pole surface at r=12.5 mm to r=25 mm.

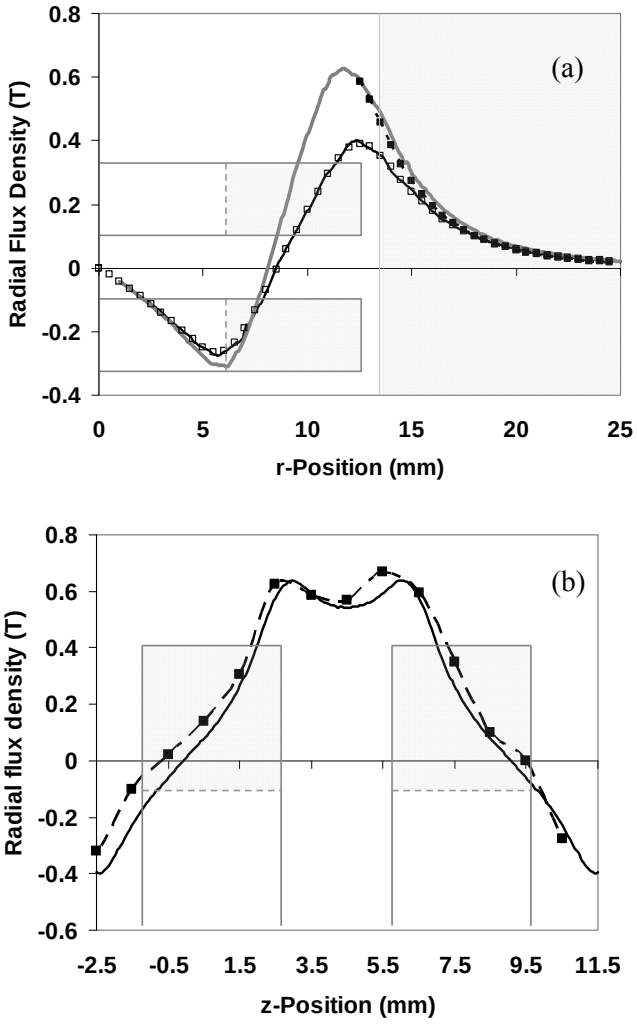

Fig. 3-21 Radial component of the flux density, (a) along line 1 obtained from: □: Analytical, ——: finite element, ——: finite element (with iron pole), ▪■▪: experiments (with iron pole), and (b) along line 2 in Fig. 3-17 obtained from: ─ ■ ─: experiments, and ——: finite element analysis.

Although, the insertion of an Iron pole between the two magnets causes a 50% increase in the flux at the magnets' edges, but the iron pole effect decreases as the distance from the magnets increases in a way that the maximum flux change in the conductor is not more than 2%. Thus, the derived analytical calculations are still valid, estimating the generated force in the conductor due to eddy

currents. It is also concluded that the analytical model has less than 0.02 T (6%) RMS error in estimation of the radial flux density. Fig. 3-21(b) shows the radial flux density along the vertical dashed line 2 in Fig. 3-17. It is evident that the analytical approach accurately models the flux density. The calculated magnetic flux density is used for the eddy current estimation.

3.2.4.2 Experimental Setup for the Magnetic Force Measurements

To validate the accuracy of the force model (3-22), another experimental setup is established. As shown in Fig. 3-22, the experimental test bed consists of an electromagnetic shaker (model LDS-722), which is controlled by an accelerometer sensor feedback. An A/D board captures the data from a 200 lb load-cell (Omega model LC703) and the LVDT at 1000 Hz sampling frequency. As depicts in the figure, the ECD's mover is attached to the fixed load-cell. The measurements are taken at the University of Waterloo.

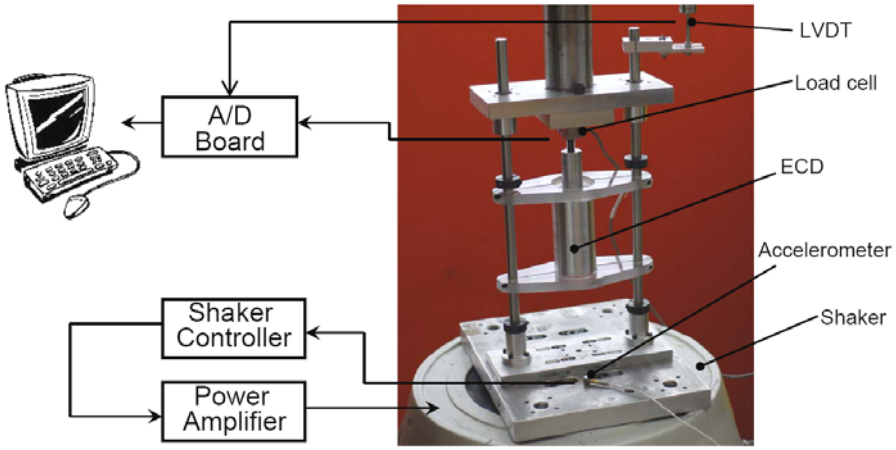

Fig. 3-22 Experimental set up for ECD.

The measurements are carried out at a constant amplitude of 2 mm, and a frequency range of 5 Hz (min shaker range) to 45 Hz. Fig. 3-23 represents the dynamic behavior of the ECD prototype at various frequencies.

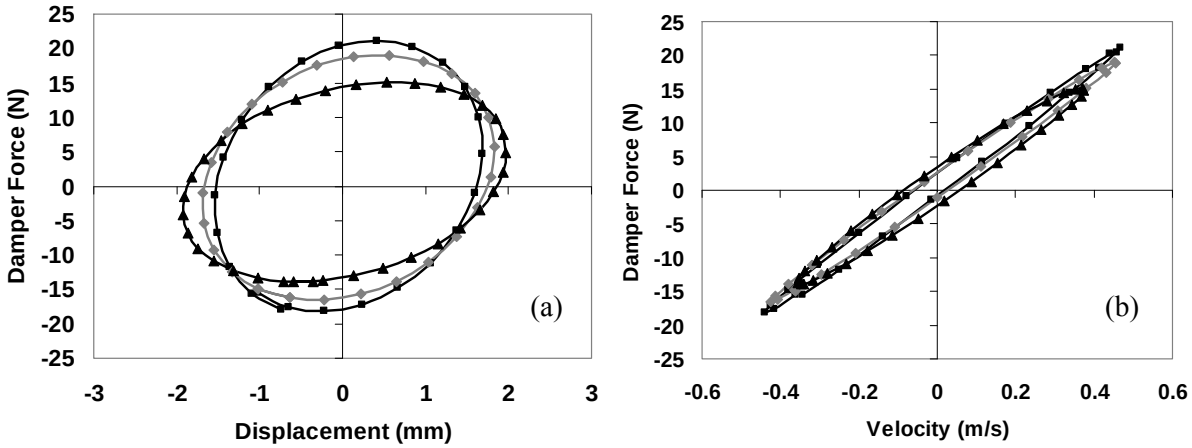

Fig. 3-23 (a) ECD force vs. displacement and (b) ECD force vs. velocity at —■—: 45Hz, —♦—: 40 Hz, —▲—: 30 Hz.

Another vital graph for the dynamic characterization of a damper is obtained by using the PVP method, as explained in Section 1.3.6, and presented in Fig. 3-24. It is observed that the results from the experimental analysis are in good agreement with those of the analytical model in (3-22); for the model without the skin effect consideration, the damping force appears to be overestimated. The derived model for the damping force exhibits a 1.4 N (7%) RMS error in the damping force estimation.

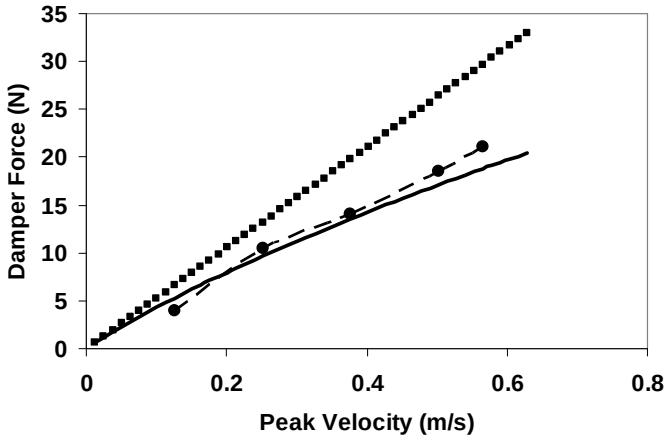

Fig. 3-24 ECD peak force vs. peak velocity at a constant amplitude of 2 mm. —●—: Experimental, ——: analytical with skin effect, and ▪▪▪: analytical without skin effect.

After the time domain analysis of the proposed ECD, the next step is the frequency and transient time domain analysis of the damper, investigating the performance of the ECD in the frequency range that is expected in the vehicle suspension system application.

3.2.4.3 Frequency and Transient time Analysis

This section employs the ECD in a vibration isolation system, investigating the frequency and transient time domain performance of the damper. An isolation system protects a delicate object either from excessive displacement or from acceleration transmitted to it from its supporting structure. A vibration isolation experimental test rig is set up, as represented in Fig. 3-25, to investigate the ECD performance and verify the derived analytical eddy current damper model. In addition, the system is simulated based on the derived analytical model for the damping coefficient, using MATLAB/Simulink, and the results are compared, confirming the analytical solution.

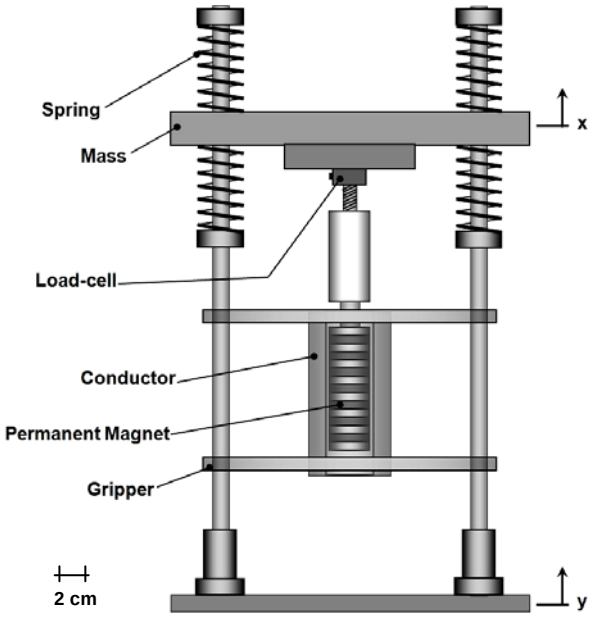

Fig. 3-25 Schematic view of the proposed eddy current damper.

As shown in Fig. 3-26, the test rig consists of a 1DOF vibration isolation system mounted on an electromagnetic shaker (model LDS 722). Two accelerometers are used to measure the base and mass accelerations. The absolute displacement of the mass is measured by a LVDT, and the damping force is monitored with a load-cell (Omega-Model LC703). The sprung-mass is 1.94 kg, and the stiffness of

the system is 4.6 kN/m. Therefore, the natural frequency of the system is obtained equal to 48.63 rad/s (7.74 Hz). A swept sine excitation with an amplitude of 1 mm and a frequency range of 5-15 Hz is used to excite the system.

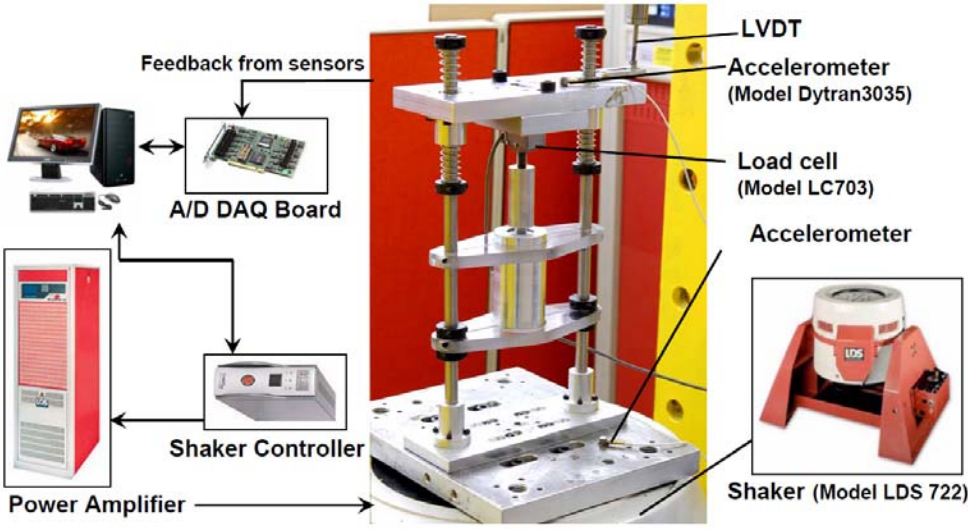

Fig. 3-26 Experimental test setup.

Fig. 3-27 depicts the Bode diagram of the displacement transmissibility for the fabricated 1DOF vibration isolation system with the aforementioned excitation input. The displacement transmissibility γ is defined as the ratio of the maximum magnitude of mass displacement to that of the input displacement as

$$\gamma = \left| \frac{\max(x)}{\max(y)} \right| , \tag{3-24}$$

where x and y are the mass and base displacements, respectively.

As shown in Fig. 3-27, the eddy current damping effect significantly reduces the motion transmitted to the mass at the natural frequency of the vibration isolation system. As in other passive dampers, the transmitted motion from the supporting structure to the mass is reduced when the ratio ω / ω_n is less than $\sqrt{2}$.

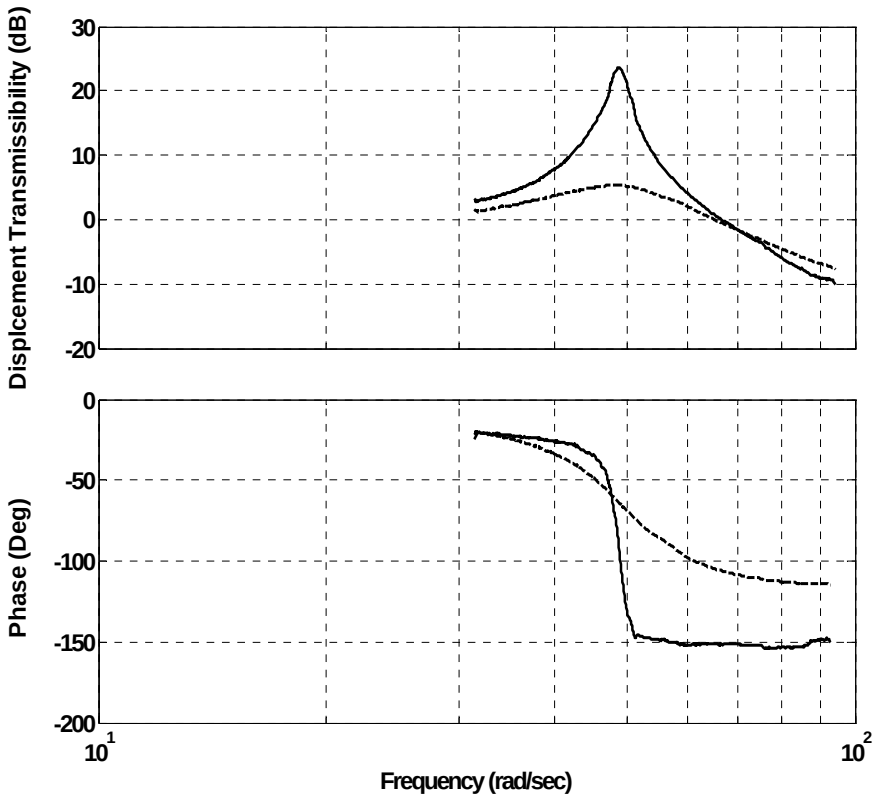

Fig. 3-27 Bode diagram of the displacement transmissibility in the 1DOF vibration isolation system, ▪▪▪▪: with, and ——: without eddy current damping.

A 1DOF isolation system with constant damping coefficient (which is a result of (3-17)) and constant spring stiffness (equal to 4.6 kN/m) is simulated in MATLAB/Simulink to validate the obtained constant damping coefficient model of the eddy current damper. Fig. 3-28 illustrates the bode diagram of the transfer function (displacement transmissibility) for the 1DOF isolation system, with and without eddy current damping effect, obtained from this simulation. The simulation results are plotted in the wide range of frequency from 1 to 10e5 rad/sec, and confirmed by the experimental results in Fig. 3-27.

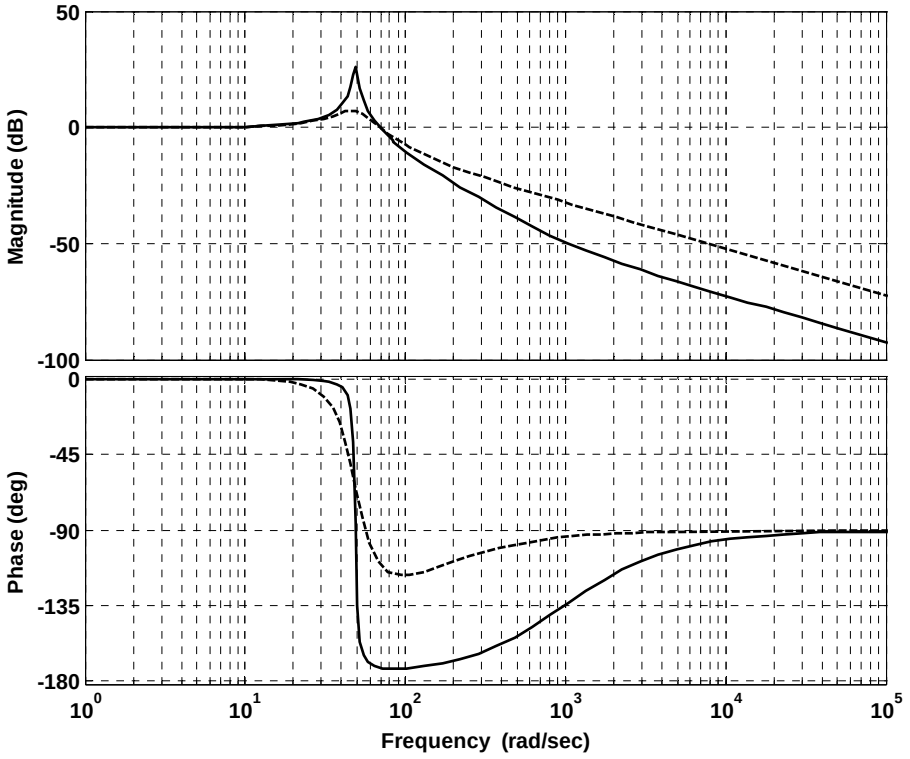

Fig. 3-28 Bode diagram of the system transfer function (displacement transmissibility), obtained from simulation, ▪▪▪▪: with, and ——: without eddy current damping effect.

Fig. 3-29(a) and (b) represent the consistency of the experimental and simulation results for the displacement and acceleration transmissibilities of the eddy current damper at the frequency range of 5-15 Hz.

As defined in Section 1.2.2, the acceleration (force) transmissibility η, as the ratio of the maximum magnitude of mass acceleration to the input acceleration at the natural frequency, and it is represented as

$$\eta = \left| \frac{\max(\ddot{x})}{\max(\omega_n^2 y)} \right| . \tag{3-25}$$

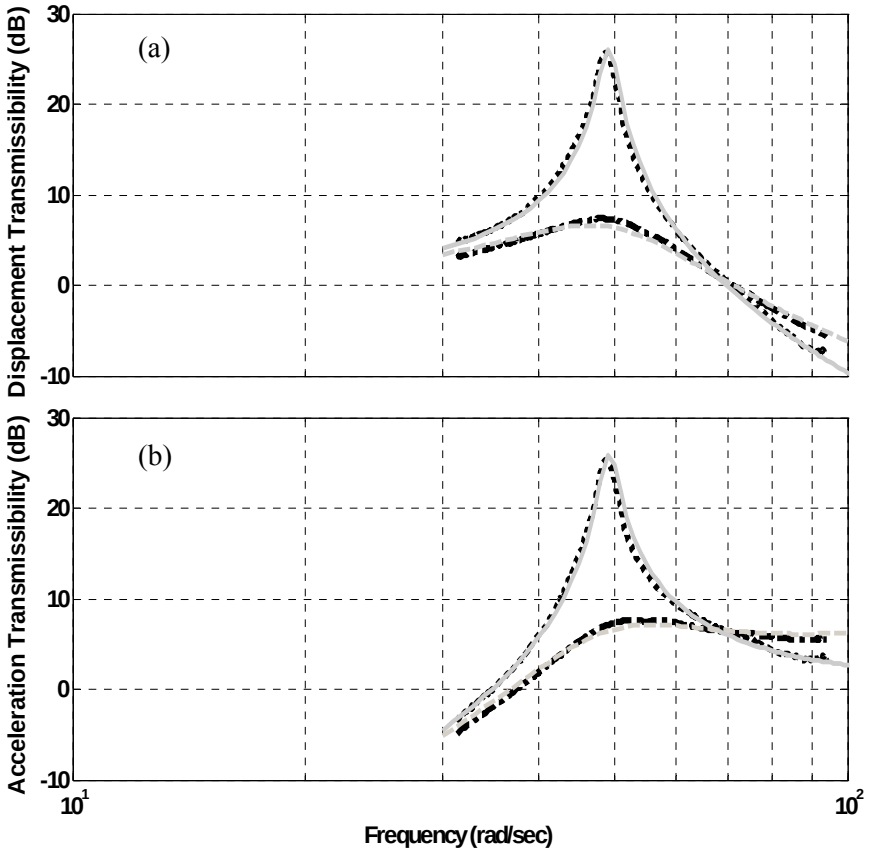

Fig. 3-29 (a) Displacement, and (b) acceleration transmissibilities of the 1DOF vibration isolation system, — ▪ —: with and ▪▪▪▪: without eddy current damping (experimental), and — —: with and ——: without eddy current damping (simulation).

It is revealed that in case of displacement transmissibility, the transmitted displacement is reduced 18.7 dB at the natural frequency. The damping ratio, as the ratio of the damping constant to the critical damping constant, is increased from $\zeta = 0.035$ at no eddy current damping condition, where the conductor tube is replaced with the similar plastic tube, to $\zeta = 0.28$ because of eddy current damping effect. The experimental results confirm the analytical model for damping coefficient of the proposed eddy current damper, obtained in (3-17), where the damping coefficient is equal to 53 Ns/m ($\zeta = 0.28$). The derived analytical model exhibits 0.1 m/s^2 (4.8%) RMS error in the transmitted acceleration to the mass.

Fig. 3-30, on the other hand, confirms the obtained results from (3-17), representing the step input response of the 1DOF system. It is seen that the simulation results, respecting the constant damping ratio of $\zeta = 0.28$, is in good agreement with the experimental data. Table 3-3 summarizes the performance criteria of the vibration isolation system obtained from Fig. 3-30. It is also observed that the maximum overshoot, and the settling time (for a 5% requirement) are decreased 54%, and 33 %, respectively, adding the eddy current damping effect.

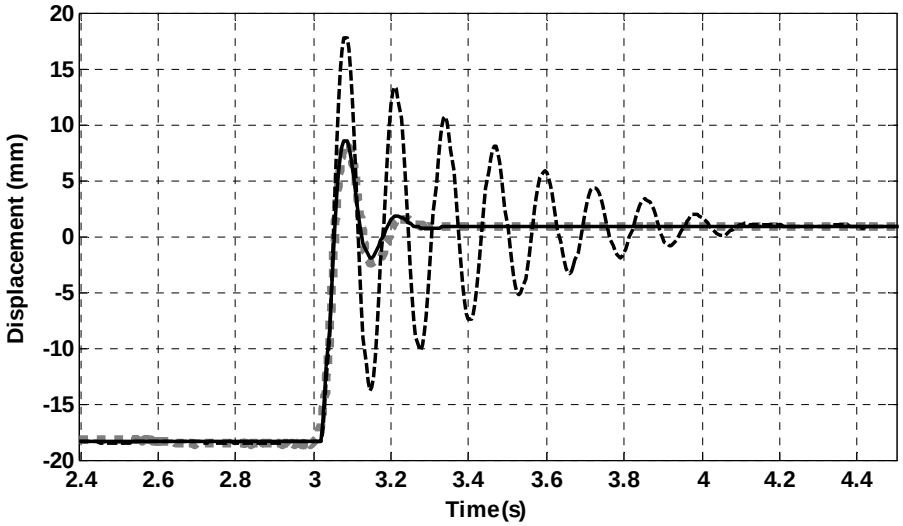

Fig. 3-30 Step response of the 1DOF vibration isolation system, ▪▪▪▪: with and ― ―: without eddy current damping (experimental), and ──: with eddy current damping (simulation).

Table 3-3 Performance criteria of the 1DOF system with and without eddy current damping.

	1DOF System without eddy current damping	1DOF System with eddy current damping	Eddy Current Damping effect
Maximum overshoot	16.9 mm	7.7 mm	54% reduction
Settling time	4.88 sec	3.23 sec	33% reduction
Damping ratio	0.035	0.28	8 times increase
Damping coefficient	6.5 Ns/m	53 Ns/m	8 times increase

The agreement between the simulation and experimental results confirms that the eddy current damping effect is similar to that of the passive oil dampers and can significantly reduce the transmitted motion to a delicate mass and improve the transient time response characteristics of a vibration isolation system.

One of the key factors for the ECD feasibility study in vehicle application is the reliability issue. The demagnetization of the PMs plays a vital role in the ECD fail-safety, while it is highly influenced by the temperature. Thus, the next step is to analyze the ECD from the heat transfer perspective, and to estimate the temperature rise due to the eddy current generation in the conductor material. The demagnetization effect and ECD reliability will be discussed later on, in Section 3.4.1.

3.2.5 Heat Transfer Analysis

As discussed earlier in Chapter 1, the vibration energy of the car frame is converted into heat via eddy current induction causing the conductor to heat up. The primary role of this section is to establish the heat transfer properties of the damper, to ensure it does not overheat, and to predict the temperature rise to be used in the PM demagnetization studies in Section 3.4.1.

In this stage, after the governing heat transfer equations for the ECD are derived, the temperature increase due to the eddy current generation at the inside surface of the conductor is calculated. The heat is generated around the internal surface of the conductor cylinder and is dissipated either by the forced convection in the air-gap and then by the conduction in the mover, or by the natural convection at the external surface of the conductor. A schematic view of the thermal resistance network for the ECD heat transfer is given in Fig. 3-31.

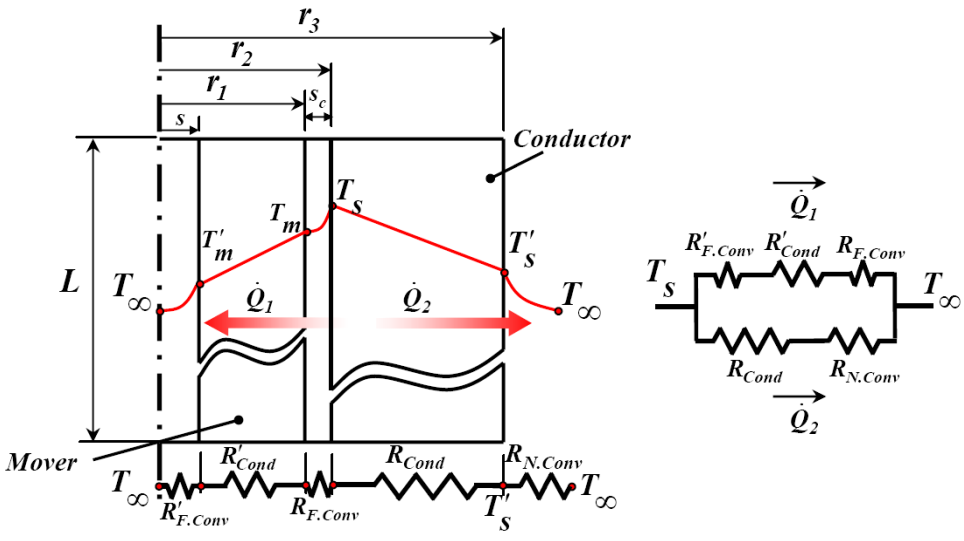

Fig. 3-31 Thermal resistance network for heat transfer through the ECD.

The temperature in the hollow section of the mover's rod is assumed as the ambient temperature to simplify the modeling. By calculating the thermal resistances, the surface temperature is obtained from Newton's law of cooling as follows:

$$(T_s - T_\infty) = \left[\frac{\left(R_{Cond} + R_{N.Conv}\right)\left(R_{F.Conv} + R'_{Cond} + R'_{F.Conv}\right)}{R_{Cond} + R_{N.Conv} + R_{F.Conv} + R'_{Cond} + R'_{F.Conv}} \right] Q \,. \tag{3-26}$$

The conduction resistances are conveniently obtained as

$$R_{Cond} = \frac{\ln(r_3 / r_2)}{k_c 2\pi L} \tag{3-27}$$

and

$$R'_{Cond} = \frac{\ln(r_1 / s)}{k_m 2\pi L}, \tag{3-28}$$

where k_c and k_m are the thermal conductivity of the conductor and mover, respectively. The forced-convection resistances are found by computing

$$R_{F.Conv} = \frac{1}{h_F (2\pi r_2 L)} \tag{3-29}$$

and

$$R'_{F.Conv} = \frac{1}{h'_F (2\pi s L)}, \tag{3-30}$$

where h_F and h'_F are the forced-convection heat transfer coefficients, calculated from

$$h_F = \frac{k_a}{s_c} Nu \tag{3-31}$$

and

$$h'_F = \frac{k_a}{2s} Nu \,, \tag{3-32}$$

where k_a and Nu are the thermal conductivity of the air and the Nusselt number, respectively. The dimensions, s_c and $2s$, represent the characteristic lengths (L_c) of the respective geometries. The Nusselt number is calculated from empirical equations (Cengel, 2005) and depends on the flow regime. The Reynolds number determines the forced convection regime (laminar/turbulent) in the air-gap. The Reynolds number inside the concentric annular ducts is calculated by

$$Re = \frac{vL_c}{\upsilon}, \tag{3-33}$$

where v and υ are the velocity and kinematic viscosity of the air, respectively. The critical Reynolds number is accepted to be 2300.

Finally, the natural-convection resistance is estimated from

$$R_{N.Conv} = \frac{1}{h_N(2\pi r_2 L)}. \tag{3-34}$$

h_N is the natural-convection heat transfer coefficient. A vertical cylinder can be treated as a vertical plate, when

$$2r_2 \geq \frac{35L}{Gr_L^{1/4}}, \tag{3-35}$$

where G_r is the Grashof number (Cengel, 2005); therefore, the natural-convection heat transfer coefficient is conveniently obtained from an empirical correlation equation as follows:

$$h_N = \frac{k_a}{2r_2}\left[2 + 0.5\left(P_r.G_r\right)^{0.25}\right], \tag{3-36}$$

where P_r is the Prandtl number of the air for the respective pressure and temperature. The Grashof number for natural convection is similar to the Reynolds number in forced convection, and is mathematically expressed as

$$G_r = \frac{g\beta(T_s - T_\infty)(2r_2)^3}{\upsilon^2}, \tag{3-37}$$

where g and β are the gravitational acceleration and coefficient of volume expansion, respectively, for an ideal gas $\beta = 1/T_\infty$. According to (3-36), h_N is a function of the surface temperature, so the surface temperature is obtained from (3-26) after a few iterations.

The properties of air at 1 atm and $20^{\circ C}$ are $k_a = 0.0269\,\mathrm{W/m^{oC}}$, $P_r = 0.7241$, $\upsilon = 1.749\times10^{-5}\,\mathrm{m^2/s}$, $\beta = 1/293$ 1/K, and the geometry dimensions are $L = 0.1\,\mathrm{m}$, $r_1 = 13\,\mathrm{mm}$, and $r_2 = 25\,\mathrm{mm}$. The conductor (aluminum) and mover (iron) thermal conductivities are $k_c = 235$ W/mK and $k_m = 80.4$ W/mK, respectively. For the average mover velocity of 0.12 m/s, the heat transfer rate is 1.5 W. Since the Reynolds number is below the critical value, the flow regime is assumed to be laminar, and the Nusselt number for the force-convection is $Nu = 4.36$ (Cengel, 2005). The steady-state temperature rise of the conductor surface is obtained from (3-26) by iteration as $14.2\,^{\circ C}$.

In this next section, the ECD design will be modified for a full-size damper, its applicability in vehicle suspension applications will be evaluated, and the demagnetization effect will be studied to ensure the fail-safety and reliability of the ECD.

3.3 Real-size Eddy Current Damper Design

After the modeling and experimental analysis of the ECD prototype, the feasibility of using a full-scale ECD as a passive damper in vehicle suspension is studied in this section. The obtained results for the full-scale ECD studies will be also used for the final hybrid damper design in Section 5.5. The design is modified and optimized specifically for automotive applications, achieving a higher damping performance while minimizing weight and cost. According to obtained results in Section 2.4, a mean damping coefficient within the range of 1500-2000 Ns/m is required for a passive damper in a typical vehicle suspension system. The maximum acceptable damper external diameter and length are also 150 and 600 mm, respectively.

One crucial parameter in the full-size ECD design is the radial component of the magnetic flux density. According to (3-17), the damping force increases with the radial flux density to the second power. Fig. 3-32 displays the different PM configurations in the mover.

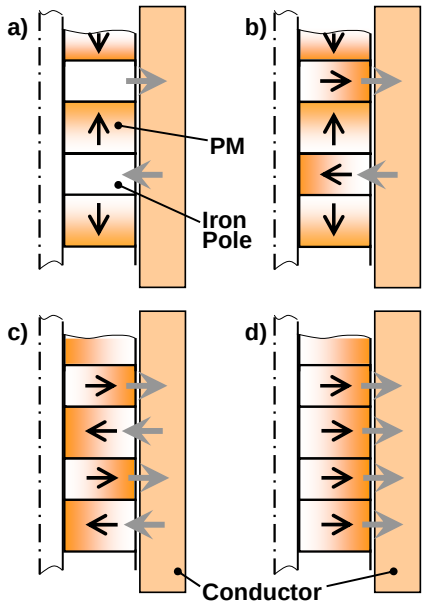

Fig. 3-32 Different PM configurations in the mover. a) Axially, b) axially and radially, c) radially (inward and outward), and d) radially (outward) magnetized PMs in the mover.

The optimum choice is the configuration that results in the highest damping coefficient obtaining from (3-22). The FE simulations of the four different cases, with the overall dimensions listed in Table 3-2, are done with Comsol 3.4 and are represented in Fig. 3-33. The overall maximum radial flux density, the maximum radial flux density in the air-gap, and the damping coefficient for each case are presented in Table 3-4. In this table, FE method is used for the magnetic flux density calculation, and the damping coefficient is obtained by doing the integral (3-18) over the conductor volume for each case, in the FE software. It is inferred from Table 3-4 that the configuration in Fig. 3-32(b) increases the damping coefficient by as much as 57%, compared with that of (a) and four times as much, compared with that of (c). Fig. 3-32(d) configuration results in the lowest radial flux density, and so the lowest damping coefficient.

Fig. 3-34 signifies the radial component of the magnetic flux density at the mid-distance of the air-gap, along the conductor's length. It is observed that the use of axially and radially-magnetized PMs in Fig. 3-32(b), is the optimum topology, providing highest air-gap magnetic flux density and resulting in the highest damping coefficient.

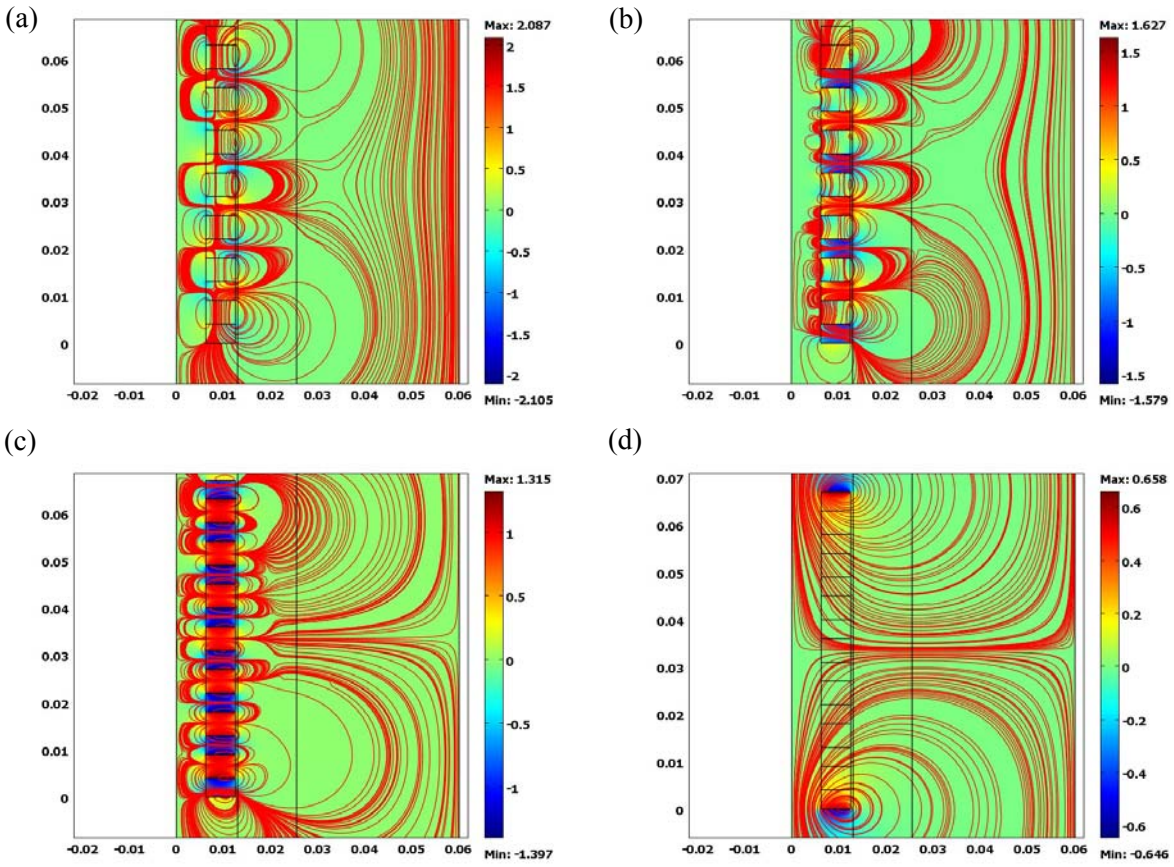

Fig. 3-33 2D axisymmetric FE simulation of different PM arrangements in the mover. Surface: magnetic flux density, r component (T), Streamline: magnetic flux density.

Therefore, the configuration in Fig. 3-32(b), which is composed of axially and radially-magnetized PMs, is selected as the optimum topology.

Table 3-4 Comparison of different PM configuration.

Configuration	(a)	(b)	(c)	(d)
Max(B_r) [T]	2.087	1.627	1.315	0.658
Max(B_r) in the gap [T]	0.68	0.81	0.43	0.18
Damping Coefficient (C) [Ns/m]	52.47	82.46	19.86	3.9

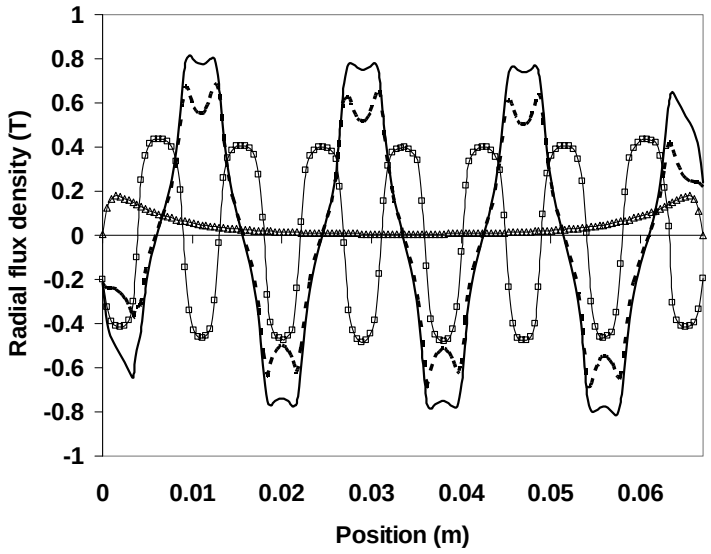

Fig. 3-34 Radial flux density along the mover length for different magnet configurations: ▬▬: Axially, ──: axially and radially, ─□─: radially (inward and outward), and ─Δ─: radially (outward) magnetized PMs.

To increase the effective radial magnetic flux density over the conductor, another layer of a PM array is added to the design. The polarity of the outer magnets array is chosen such that the radial magnetic flux from the outer magnets adds to that of the inner magnets.

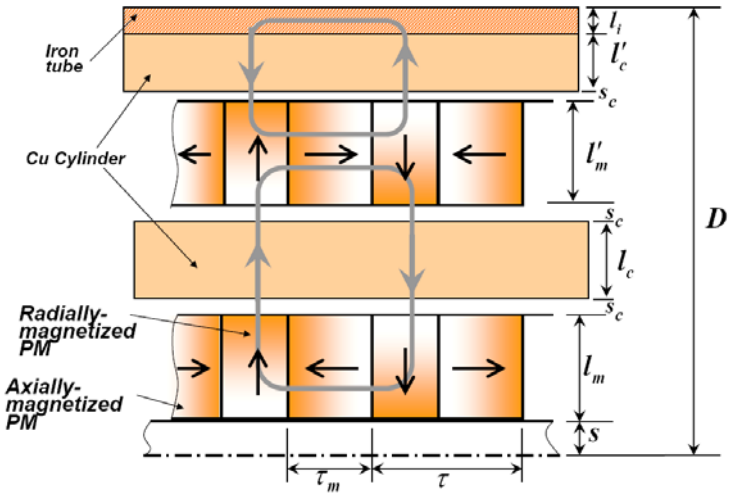

Fig. 3-35 Schematic configuration of the real-size ECD.

Fig. 3-35 reflects the modified ECD configuration with the additional PM tube. To take advantage of the outward magnetic flux that is generated by the second PM layer, another conductor layer is added to the ECD.

Another modification is that copper is selected as the conducting material instead of aluminum because of its higher electrical conductivity (σ_{Cu}=5.88e7 S/m) compared to aluminum (σ_{Al}=3.7e7 S/m). The outside diameter limit of the damper is set to 90 mm for the physical restriction. The design procedure for inner PMs is similar to that of the ECD prototype, described in Section 3.2.2. The air-gap thickness should be as small as possible, and is limited by the manufacturing restrictions. The air-gap thickness is set to 1 mm. The damping coefficient and the weight of the ECD for different outer conductor and PM thicknesses are listed in Table 3-5

Table 3-5 Damping coefficient and weight of the ECD for different conductor and PM thicknesses.

	l_c=2 mm	l_c =5 mm	l_c =10 mm	l_c =15 mm	l_c =20 mm
l'_m =3 mm	645 kg/s 1.65 kg	1118 kg/s 2.45 kg	1340 kg/s 4.03 kg	1336 kg/s 5.95 kg	1305 kg/s 8.22 kg
l'_m =6.25 mm	1053 kg/s 2.43 kg	1880 kg/s 3.25 kg	2351 kg/s 5.1 kg	2448 kg/s 7.2 kg	2498 kg/s 9.65 kg
l'_m =10 mm	1408 kg/s 3.48 kg	2551 kg/s 4.5 kg	3267 kg/s 6.48 kg	3488 kg/s 8.79 kg	3641 kg/s 11.46 kg

In order to obtain the optimum conductor and outer magnets thicknesses, the generated damping coefficient for different magnet thicknesses are plotted vs. the conductor thickness in Fig. 3-36. The hatched box in Fig. 3-36 shows the required passive damping coefficient. It is observed that increasing the conductor thickness does not affect the damping coefficient after a certain level, and so there is an optimum conductor thickness for each outside magnets' thickness. The amount of generated damping coefficient divided by ECD weight is also plotted in Fig. 3-37. It is revealed that the maximum damping coefficient is obtained at conductor thickness l_c equal to 5 mm, regardless of the outer magnets' size. It is also deduced that the generated damping effect per ECD weight does not linearly increases by outer magnets' thickness, and has its optimum value at the outer magnet thickness l'_m equal to 6.25 mm.

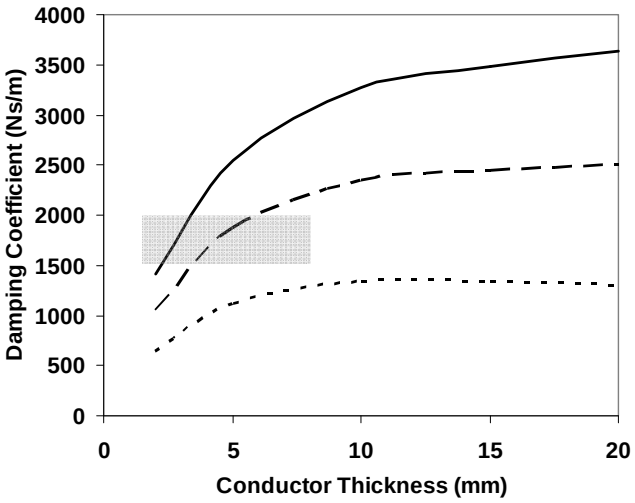

Fig. 3-36 Damping Coefficient vs. conductor thickness for different outer magnets thicknesses. ——: $l'_m = 10mm$, — —: $l'_m = 6.25mm$, ▪▪▪: $l'_m = 3mm$.

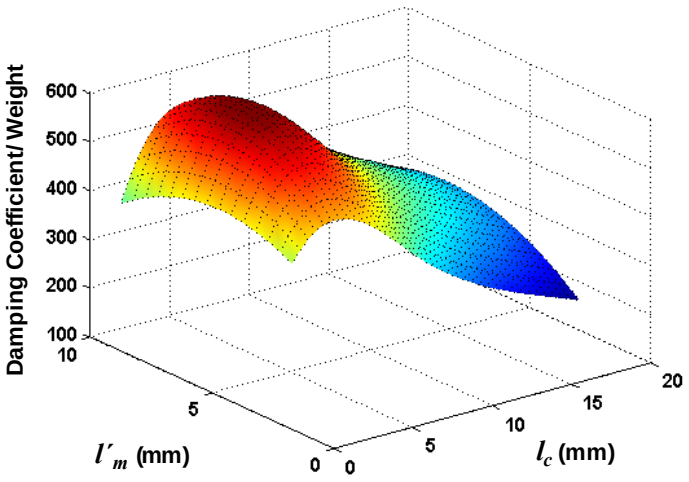

Fig. 3-37 Damping Coefficient/weight vs. conductor thickness for different outer magnets thicknesses.

After selecting the conductor and outer magnet thicknesses, the final step is to set the outer conductor's thickness. The radial component of the magnetic flux density along the centerline of the radially-magnetized PMs is shown in Fig. 3-38. Obviously, the radial flux density over the outer conductor is insignificant, and its contribution to the damping force, given by (3-22), is less than 4% of the inner conductor. Thus, the outer conductor is omitted from the final design. Consequently, the

iron shell is eliminated, and replaced with a lightweight protecting shield, due to its negligible contribution in enhancing the overall damping coefficient of the ECD.

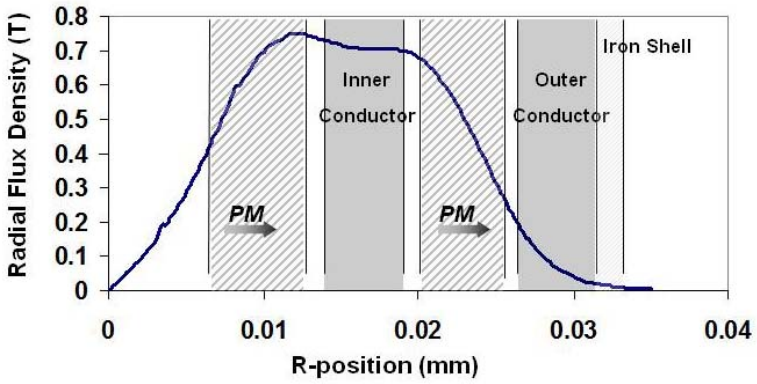

Fig. 3-38 Radial flux density along the centerline of the radially-magnetized PMs.

Fig. 3-39 offers the proposed design for a real-size ECD, consisting of a hollow, copper cylinder, and two cylinders of axially and radially-magnetized PMs in the configuration shown in Fig. 3-35. The design specifications are listed in Table 3-6.

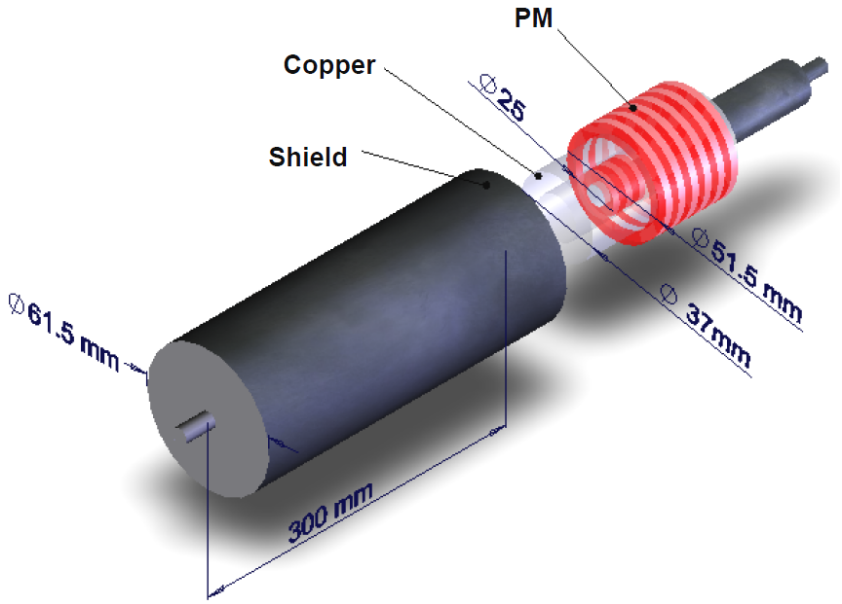

Fig. 3-39 Real-size version of the ECD for vehicle suspension systems.

Table 3-6 Specification of the real-size ECD.

Item /Symbol	Value/Unit
Number of poles p	12
Pole pitch τ	20 mm
Magnets' thickness τ_m	10 mm
Inner magnets	
Inside diameter $2s$	12.5 mm
Outside diameter $2(l_m+s)$	25 mm
Outer magnets	
Inside diameter	39 mm
Outside diameter	51.5 mm
Rod diameter $2s$	12.5 mm
Mover weight	2.25 kg

Item /Symbol	Value/Unit
Shield thickness l_i	4 mm
Inner conductor	
Inside diameter	27 mm
Outside diameter	37 mm
Length	240 mm
Air-gap thickness s_c	1 mm
Damper outside diameter $2D$	61.5 mm
Conductor weight	1 kg
Damper weight	3.25 kg
Magnets' material	Nd-Fe-B B_r=1.17 T

3.4 Comparison and Evaluation

In the previous section, the optimum dimensions of the full-scale ECD are derived to be used in a passive suspension system. The evaluation of the novel ECD is followed by a comparison of the size, weight, cost, and performance of four dampers: a magnetorheological-fluid semi-active damper, two commercial passive dampers, and the ECD. Table 3-7 illustrates the size, weight, cost, and the maximum damping coefficient comparison of these dampers. The passive mono-tube damper is a C1500 Chevy pickup damper that offers traditional Bilstein technology for trucks, and features a mono-tube high-pressure design. Another passive damper is a Tokico's D-spec series (DSP-4) damper for Mustang, utilizing a variable-aperture bypass, which is tuned manually by an adjustable slide valve. Finally, the Cadillac MR-fluid damper is a newly commercialized MagneRide damper from Delphi. The MagneRide design employs an electromagnetic coil wrapped around the passageway between the chambers, which are filled with MR-fluid. The MR-fluid yield stress varies through the coils' current adjustment. A comparison of the ECD with the off-the-shelf passive dampers reveals that the size and cost of the ECD is higher than those of passive oil dampers. It seems that the high density of the copper and rare-earth magnets results in the ECD being three times heavier than an ordinary passive damper. Moreover, the ECD cost is more than twice higher than a

commercial passive damper, due to the high cost of rare-earth magnets, which is around 250 US$/Kg. It should be mentioned that the manufacturing costs are not included for the eddy current damper.

Table 3-7 Size, weight, price, and maximum damping comparison of dampers.

Damper type	Max. Length (mm)	Weight (kg)	Cost (US$)	C_{max} (Ns/m) in Compression	C_{max} (Ns/m) in Extension
MR-fluid damper (0 A)	650	4.08	1000	1608	2642
MR-fluid damper (1.5 A)	650	4.08	1000	5646	5480
Passive mono-tube damper	550	1	80	1960	9800
Passive double-tube damper	600	1.2	200	1568	3920
Eddy current damper	400	3.25	400	1880	1880

Fig. 3-40 illustrates the damper performance comparison. The non-dimensional damping coefficient, C/C_{max}, is plotted for the ECD and compared with that of Mustang, Chevy (Vahid, 2006), and Cadillac MR-fluid dampers. As previously mentioned, the off-the-shelf, Cadillac, MR-fluid damper is purchased and tested at different input currents with an MTS hydraulic shaker at the University of Waterloo. It appears that all the dampers have the same pattern of higher damping coefficients at low velocities, which is desirable in automobile damper design. The mean damping coefficient for the proposed eddy current damper is obtained as 1500 Ns/m, which is within the acceptable range obtained in Chapter 2.

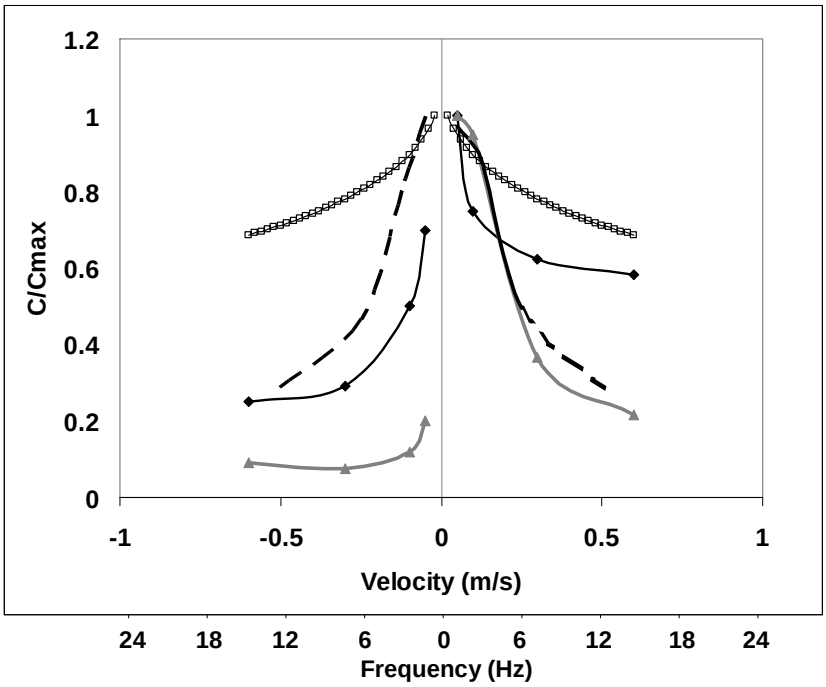

Fig. 3-40 Normalized damping coefficient vs. velocity, —▲—: Chevy pickup, —♦—: Mustang, ▬ ▬: Cadillac (0 A), and —□—: ECD.

The damping performance pattern for the ECD is highly affected by the skin effect, which causes the damping to decrease at higher frequencies. Fig. 3-41 demonstrates the force-velocity curves for dampers. In compression, all dampers have the same force-velocity characteristics, except for the Cadillac MR-fluid damper. For the MR-fluid damper, the damping force increases with the applied voltage, resulting in a low damping force in the off-mode. For semi-active dampers, damping performance in the off-mode portrays the fail-safety of the suspension system, and the damper is required to provide an acceptable damping performance in the off-mode. The poor damping characteristic in the off-mode is one of the MR-fluid damper's drawbacks.

In the compression mode, the ECD exhibits a higher damping force rather than other passive oil dampers. On the other hand, in extension, the ECD displays a lower force level compared with that of other passive dampers, although its damping force is still higher than that of the MR-fluid damper in the off-mode.

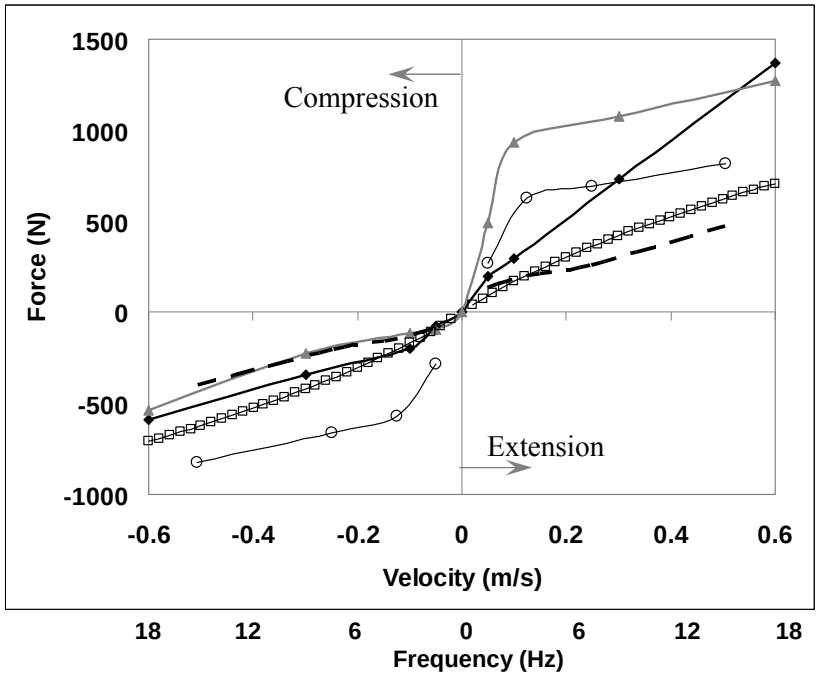

Fig. 3-41 Force-velocity curves for different dampers, —▲—: Chevy pickup, —♦—: Mustang, — —: Cadillac (0 A), —○—: Cadillac (1.5 A), and —□—: ECD.

The force-velocity curves reveal that although the ECD force level is not so appealing in extension mode, compared with other passive dampers, it is still practical in case for light-weight vehicles. At this stage, the performance and cost of the proposed ECD is restricted by the current magnet technology. However, with advancements in magnet and conductor material technologies, the proposed system has the potential for significant improvements. The proposed ECD design will be implemented in the final hybrid damper design as a source of passive damping, discussed in Chapter 5.

3.4.1 Demagnetization Effect and Reliability

The ECD fail-safely issue is one of the crucial factors for its vehicle application feasibility, and is highly influenced by the demagnetization of the PMs in their operating life. Factors that affect the magnet stability include time, temperature, adverse fields, shock, and stress. The effect of time on modern PMs is minimal. Rare earth magnets are not vulnerable to the time factor due to their high

coercivities. Over 100,000 hours, theses losses are in the range of essentially zero for NdFeB magnets used in this study.

The temperature rise estimated in Section 3.2.5 demonstrates that the temperature rise is well below the Curie temperature (310^{oC} for NdFeB) that causes the irreversible losses in magnetization of PMs. Also, the reversible loss due to the temperature rise is so small that can be ignored. For example, for the NdFeB magnets in this study, the magnetization change is less than 3% for temperature rise of 50^{oC}.

External magnetic fields in repulsion mode produce a demagnetizing effect on each other. Rare earth magnets with coercive forces exceeding 15 kOe are not likely to affect in this manner. The external magnetic field that should be applied to fully demagnetize a magnet depends on the coercive magnetic field (H_c), remanent magnetization (M_r), and the shape of the magnet. For the proposed magnets' shape (cylindrical shape) the demagnetization field is equal to the remanent magnetization, so the required external magnetic field for demagnetization is obtained (Furlani, 2001) as

$$H_{ext} = H_c - M_r \tag{3-38}$$

For the rare earth magnets in this paper with $M_r = 1.03e6$ A/m, and $H_c = 1.4e6$ A/m, the required external field is equal to 3.7e5 A/m, corresponds to a magnetic flux density equal to 0.47 T, which is beyond the effect of the adjacent magnet in the proposed configuration (where the maximum axial flux density is less than 0.4 T). Finally, the effect of shock and stress below the destructive limits are very minor on rare earth magnets. However, in the proposed configuration, these effects are inconsequential due to the non-contact nature of the ECD.

In addition, the leakage flux from the damper causes a magnetic flux density in the order of 0.5 G in a 10 cm distance from the ECD, which is in the order of the earth magnetic field and has a negligible effect on the electric sensors and instruments in the vicinity of the damper. In conclusion, utilizing the rare earth PMs in the proposed ECD ensures the damper reliability and durability.

3.5 Conclusions

The eddy current damping effect is studied in some detail and utilized in development of a novel Eddy Current Damper (ECD) for vehicle suspension applications. The idea was to develop a passive

damping component for the final hybrid design. However, the ECD as stand-alone passive damping unit is characterized and its performance is studied in this chapter.

This chapter comprises four main sections. In the first section, a passive Magnetic Spring-Damper (MSD) system is developed by using the eddy current damping effect. The proposed MSD utilizes two Permanent Magnets (PMs) and a stationary conductive aluminum plate. A theoretical model of the proposed system is constructed by using the transformer eddy current contribution and the image method for the motional eddy current estimation. The magnetic flux, interaction force of the magnets, and eddy current damping force are analytically calculated and validated by Finite Element (FE) and experimental results. Finally, the dynamic damping characterization of the system is derived by using the differential Bouc-Wen model. The novel MSD described in this chapter is a non-contact device with adjustable damping characteristics. The damping characteristic of the proposed system can be easily changed by either re-positioning the conductor or choosing the appropriate conductor size and the air-gap distance between the magnets.

The development of the MSD in the first section offers an in-depth understanding of the eddy current damping effect, leading to a new optimized ECD topology, which is studied in the second section of this chapter. A prototype ECD is developed, the proposed ECD geometry is selected, and experiments done to verify the analytical model for the magnetic flux density and the force model. In addition, the frequency and the transient time behavior of the proposed ECD in a 1DOF vibration isolation system is investigated. It is shown both analytically and experimentally that the damping characteristics of a 1DOF isolation system can be improved more than eight-fold by, adding eddy current damping to the system. The heat transfer analysis is also performed to ensure that the damper does not overheat and to study the temperature effect on the PMs demagnetization. It is demonstrated that a damping coefficient as high as 53 Ns/m is achievable with the developed ECD prototype.

In the third section of Chapter 3, the design is modified, a real-size ECD for the vehicle suspension application is characterized, and the feasibility of using a passive ECD in vehicle suspension is studied. The final optimization procedure involves both analytical and finite element methods for damping performance estimation.

Finally, after the full-size ECD is designed based on the derived model, its performance is compared with the performances of the commercial passive dampers in Section 3.4. In addition, the

demagnetization effect and the magnets stability due to different factors, such as temperature and time, are studied to ensure the ECD fail-safety and reliability.

The ECD proposed in this chapter is oil-free and non-contact, offering high reliability and durability with its simplified design. Unlike other common dampers, the proposed ECD does not cause stiffness to be added to the vibration isolation system due to its non-contact nature. Although the weight and cost of the ECD as a stand-alone passive damper is not very appealing, compared with commercial passive dampers, the performance of the newly developed ECD in vehicle suspension applications is still attractive, especially as a potential passive damping source in the hybrid damper design. The performance of the proposed ECD can be significantly improved by using high-quality, low-weight PMs, and conductors with higher conductivity.

Chapter 4

Electromagnetic Damper Concept Development

After investigating a passive damping component for the hybrid damper in the previous chapter, the next step involves the development of an active actuator module, providing enough active damping force for the hybrid design. To this end, an electromagnetic linear actuator is proposed that has an energy harvesting capability. This chapter describes the design, modeling, and Finite Element (FE) analysis of the proposed linear actuator. The performance of the linear actuator is also investigated as a stand-alone Electromagnetic Damper (ED) in an active suspension system.

As shown in Fig. 4-1, the conceived ED consists of two main parts: a fixed stator and a moveable slider. In the stator, windings (and potentially position and temperature sensors) are integrated into a metal cylinder. On the other hand, the mover (slider) utilizes Permanent Magnets (PMs) that are screwed to an aluminum rod via iron spacers (pole pieces).

The proposed regenerative damper converts the vibrations of the body mass into a useful electrical energy, compensating the high energy consumption in active suspensions. The damper is also cost-effective, consisting of several PMs in combination with electromagnets as major components and a straightforward fabrication. This cost-effective, regenerative ED is based on the concept of a tubular, linear, brushless dc motor, and can be used in passive, semi-active, and active operating modes. In the passive/semi-active modes, the ED operates as a generator, converting the vibration of the vehicle body to electrical energy, where the motional electromotive force (emf) is induced in the coils due to the relative motion of the mover and stator. The generated emf creates an opposing force that is proportional to the velocity of the mover, causing a viscous damping effect. On the other hand, in the active-mode, the coils are energized so that the ED can operate as an actuator.

The ED design is started with the optimal topology selection, and continues with a prototype ED design procedure to achieve the maximum thrust force density, utilizing analytical models derived from magnetic circuit principles. Next, after a prototype ED is fabricated, experiments are carried out in the passive mode to verify the accuracy of the numerical model. The prototype design ultimately

leads to a real-size ED design in the last section, where the analytical models are utilized to estimate the maximum thrust force capacity of the ED. In addition, finite element analysis is used to enhance the accuracy of the modeling so that the performance of the real-size ED can be estimated with higher accuracy.

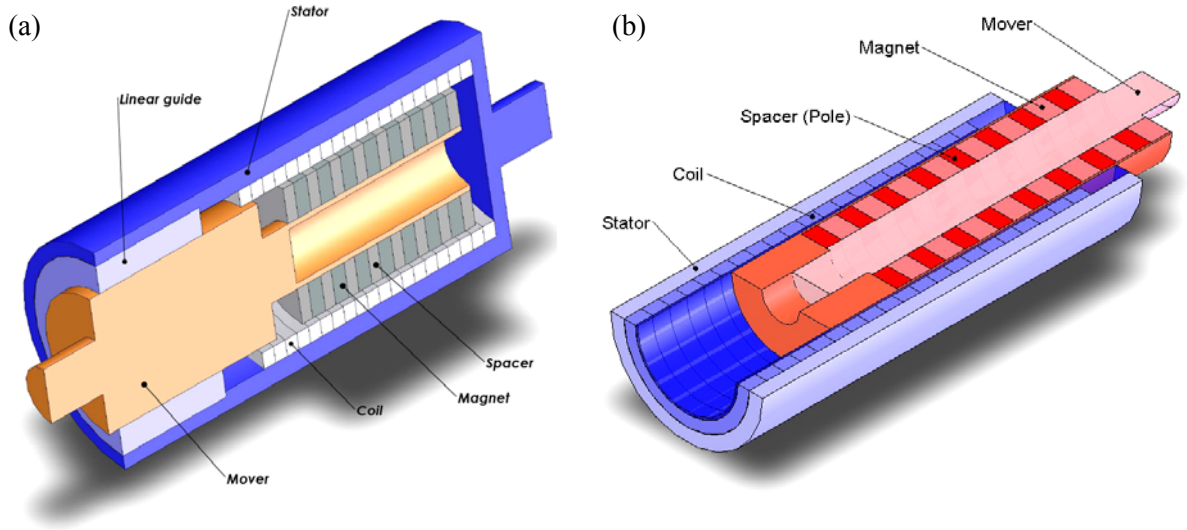

Fig. 4-1 Schematic views of the proposed electromagnetic damper with two different configurations. (a): Annularly-shaped magnets supported by a non-magnetic rod, and (b): magnets fastened together in a non-magnetic tube.

4.1 General Topology Selection

Among possible choices of active ED implementation there are hydraulic and electromagnetic actuators. High reliability and dynamic performance, together with lower volume, weight, and cost of electromagnetic actuators compared to their hydraulic competitors, justify the generalized use of electromagnetic actuators. Besides, it is verified that the hydraulic/pneumatic solutions are very expensive, heavy, and have high energy consumption, while the electromagnetic actuators have the advantage of suspension energy recovery (Martins *et al.*, 2006).

Some authors have proposed electromagnetic systems for automobile suspensions based on a rotational actuator (Murty, 1989) and (Kruckemeyer *et al.*, 1987), while the rotational actuators require a gearbox and complex mechanisms to convert the rotational into linear movement. However, the use of a linear motor simplifies the mechanical design and eliminates the complex process of linear-to-rotary motion conversion. Using linear motors is an effective way to address the request for

a superior actuator with higher speed, accuracy, and reliability. Here is a list of the fundamental benefits, arising from the use of direct thrust linear motors:

- Simple mechanical design with the minimum number of moving parts
- Direct thrust motors highly eliminate the backlash and wear
- Fast response-time (<10 ms)
- High acceleration with high motor force/weight ratio

Besides, for the specific case of tubular linear motors, as the PMs in the mover are completely encircled by the stator coils, the design is extremely efficient. They have also high duty cycle capability because of their intrinsic thermal efficiency and all-round heat dissipation.

All the designs that have been put forward for linear motors divide into high-acceleration and low-acceleration motors. High-acceleration linear motors (utilizing linear induction design) are quite short, and are designed to accelerate an object to a very high speed, while low-acceleration ones with linear synchronous design are suitable for high speed, high power applications. Linear synchronous deigns, with an active winding adjacent to an array of alternate-pole magnets, are selected for their advantages in terms of accurate speed/position control, high speed/power performance, and the fact that the speed is independent of the load.

Generally, the preferred linear motor topology depends on the required application. There are various configurations proposed for tubular linear permanent magnet machines: internal and external magnet topologies, with different magnets arrangements, both could be either moving magnet or moving coil. In all these topologies, the mover (armature) could be either air- or iron-cored, where it could be either slotted or slotless. Selecting the proper motor topology is a compromise between different design requirements. For example, slotted stators usually cause a higher thrust force, but may also produce an undesirable tooth ripple cogging force. Slotless stator cores, on the other hand, eliminate the ripple cogging effect, improving the dynamic performance and servo characteristics at the expense of force density reduction.

From several linear motor topologies, the tubular slotless core with a moving magnet design is chosen in which the ring-shaped PMs are axially-magnetized and fastened together in the mover. Although the slotted stator core designs are superior to the slotless designs in terms of the generated damping force, to avoid cogging force complexities the slotless approach is selected for proof of concept purposes. The assembly comprises a tubular design, as shown in Fig. 4-1, which has less

leakage flux compared to the flat design, and is vastly better in utilizing the magnetic flux, leading to a higher induced emf (in the generator mode) and a higher thrust force (in the actuator mode). Axially-magnetized PMs in the mover result in a higher force-to-volume ratio rather than radially-magnetized ones.

As shown in Fig. 4-1, there are two options respecting the manufacturing issues. Fig. 4-1(a) depicts the annularly shaped magnets, supported by a non-ferromagnetic rod, while Fig. 4-1(b) shows another design with magnets fastened together in a non-magnetic tube, which is sliding on another tube shielding the stator coils. The latter configuration limits the minimum size of the effective air-gap to the sum of those two tubes' thicknesses; however, it is easier in terms of manufacturing while saving the weight and volume, as the former design requires additional linear guides. The latter configuration (as shown in Fig. 4-1(b)) is selected for ease of manufacturing and to reduce the total weight, volume and cost.

4.2 Magnetic Circuit Design

The goal is to design the geometry of the proposed ED to improve the damping performance according to the volume restriction. Therefore, the design parameters are the dimensions of the magnets and coils. An analytical analysis, based on the principles of magnetic circuits, is applied to define a relationship between the design parameters and the damper performance. Fig. 4-2 portrays the lumped model of the proposed electromagnetic shock absorber and the equivalent magnetic circuit. The direction of the flux density is also shown in the figure.

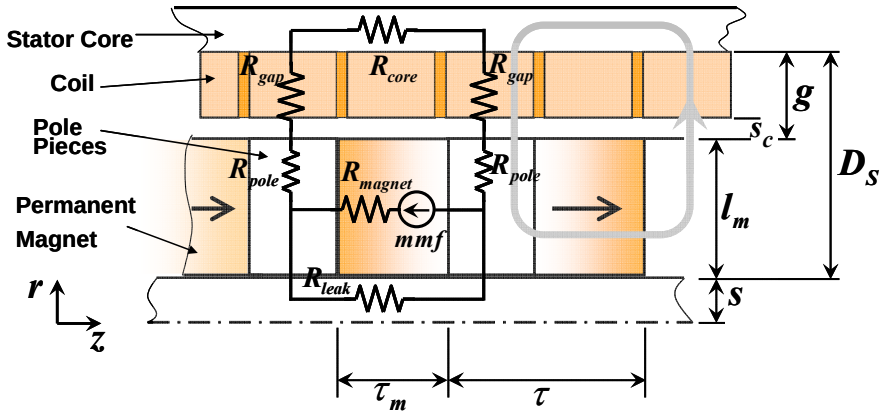

Fig. 4-2 Configuration of the linear interior PM motor and the equivalent magnetic circuit.

The analysis is performed for only one pole pair. It is assumed that the iron core has an infinite magnetic permeability, so its saturation and reluctance are neglected. Also, it is assumed that there is no leakage flux in the connecting rod diameter (2*s*).

The magnetic circuit is solved by intersecting Ampere's Law and the PM's characteristic curve (A.10)

$$\left(R_{mag}+2R_{gap}\right)\phi_g = H_c\tau_m = \frac{B_{rem}}{\mu_{rec}}\tau_m, \tag{4-1}$$

where H_c, B_{rem}, μ_{rec} are the coercive magnetic field intensity, remanent flux density, and recoil permeability of the magnets, respectively, and ϕ_g is the air-gap magnetic flux. The magnet and gap reluctances are

$$\begin{aligned} R_{mag} &= \frac{\tau_m}{\mu_{rec}\pi\left((l_m+s)^2-s^2\right)}, \\ R_{gap} &= \frac{g}{\mu_0\pi 2(l_m+s+g/2)\left(\frac{\tau-\tau_m}{2}\right)}. \end{aligned} \tag{4-2}$$

Since the leakage flux is negligible, *i.e.*, $B_g A_g = B_m A_m$, (4-3) gives the PMs' thickness in terms of the air-gap flux density as follows:

$$\tau_m = \frac{2gB_{rem}B_g}{\mu_0 H_c\left(B_{rem}-B_g\left(\frac{A_g}{A_m}\right)\right)}. \tag{4-3}$$

The air-gap magnetic flux density is mathematically expressed as

$$B_g = \frac{B_{rem}\tau_m\mu_0 H_c}{\left(2gB_{rem}+\tau_m\mu_0 H_c\frac{A_g}{A_m}\right)}, \tag{4-4}$$

where the lateral area of the pole and cross section area of the magnet are

$$A_g = 2\pi(s+l_m+g/2)\frac{\tau-\tau_m}{2} \tag{4-5}$$

and

$$A_m = \pi\left((l_m + s)^2 - s^2\right).$$

The first step is to optimize the size of the magnets to obtain the maximum magnetic flux and thrust force for the given external and internal dimensions.

For a single pole pair with pole pitch τ, as shown in Fig. 4-2, the magnetic flux in the gap for different amounts of τ / τ_m is plotted in Fig. 4-3.

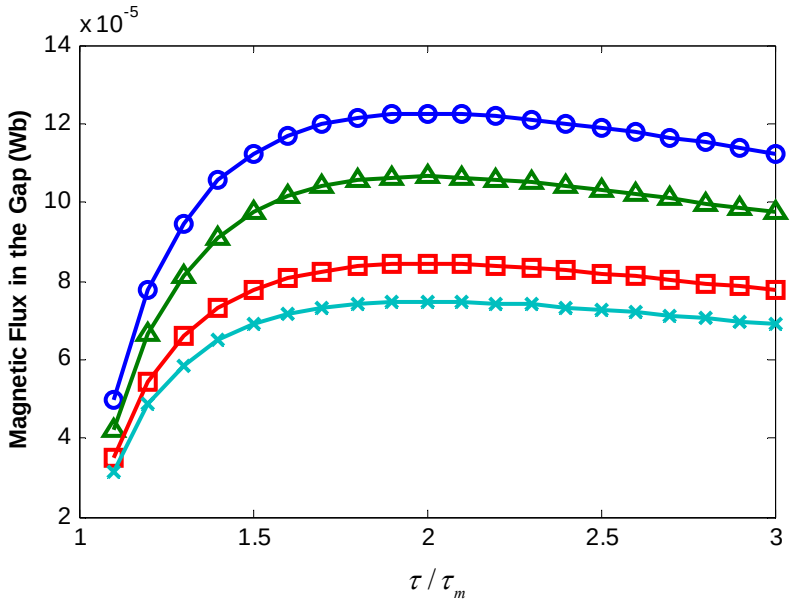

Fig. 4-3 Magnetic flux vs. normalized magnet thickness for different *s*, l_m, and *g* values. —o— : *s*=6.25, l_m=6.25, *g*=4, —Δ— : *s*=6.25, l_m=6.25, *g*=5, —□— : *s*=6.25, l_m=4.3, *g*=5, —×— : *s*=5, l_m=4.3, *g*=5.

As shown in Fig. 4-3, the maximum flux in the gap occurs at τ/τ_m between 1.5 and 2 regardless of the values of s, l_m, and g. Thus, the optimum ratio of τ/τ_m is selected to be 1.8.

For the proposed ED in the passive operating mode, where stator coils are short-circuited, the damping coefficient produced in a single stator coil is calculated by

$$C = \frac{2\pi\sigma\left(B_{rem}\tau_m\mu_0 H_c\right)^2 (\tau - \tau_m)(g - s_c)(l_m + s + g/2)}{\left(2B_{rem}g + \tau_m\mu_0 H_c A_g / A_m\right)^2}. \quad (4\text{-}6)$$

The variation of the single coil damping coefficient is plotted in terms of the normalized magnet's length for the different D_s values in Fig. 4-4. Here, the external applied current density is assumed to be zero. There appears to be an optimal value for the l_m / D_s ratio, which is around 0.8. Fig. 4-4 is plotted assuming a constant value for D_s. By increasing the magnets' length, the coils' thickness is reduced.

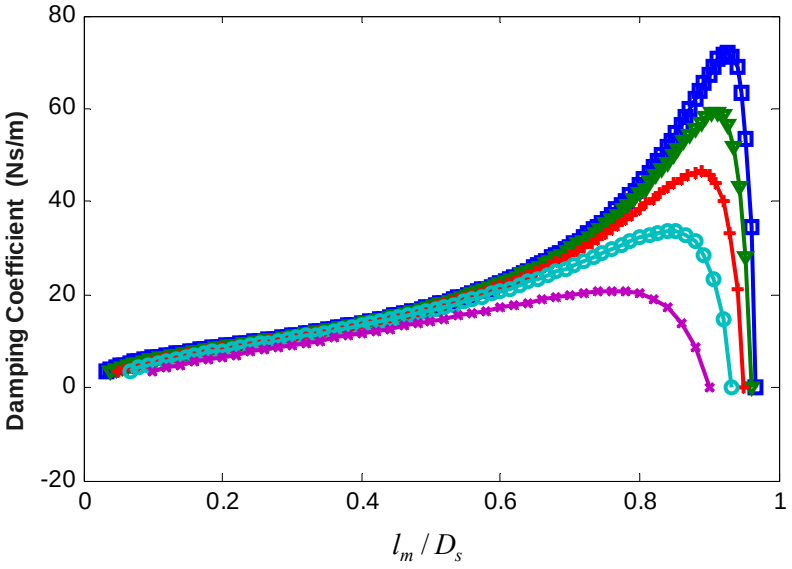

Fig. 4-4 Damping coefficient vs. normalized magnet length for different D_s values. —□—: D_s=30 mm, —∇— : D_s=25 mm, —+— : D_s=20 mm, —○— : D_s=15 mm, —×— : D_s=10 mm.

Another design parameter is the mover (slider) shaft radius (s). By assuming a constant external diameter, the mover shaft's radius must be selected to be as small as possible (Bianchi *et al.*, 2001); the shaft radius is set to 6.25 mm for the prototype.

The mover pole pitch (τ) and the coils' external radius (D_s+s) are set equal to 9 mm and 10.25 mm, as design restrictions for the prototype. The air-gap thickness as a critical design parameter is also set to 1 mm due to manufacturing restrictions. By considering the obtained results in Fig. 4-3 and Fig. 4-4, the following normalized ratios are selected to find the PM dimensions.

$$\begin{aligned} \tau / \tau_m &= 1.8, \\ l_m / D_s &= 0.6. \end{aligned} \tag{4-7}$$

The air-gap flux density is found to be 0.611 T, from (4-4), and the damping coefficient per pole is calculated as 17.74 Ns/m, from (4-6), for the ED operating in the passive mode, when the coils are short-circuited. The number of poles and magnets are selected as 8 and 7, respectively. Finally, 15 coils with a width of 4.5 mm are embedded in the stator core to obtain the similar pitch for the poles and coils. Final specifications of the ED prototype are summarized in Table 4-1, and its overall physical dimensions are shown in Fig. 4-5.

Table 4-1 Specifications of the electromagnetic damper prototype.

Item /Symbol	Value/Unit
Mover	
Number of poles p	8
Pole pitch τ	9 mm
Magnets thickness τ_m	5 mm
Magnets outside diameter $2(l_m + s)$	25 mm
Rod diameter $2s$	12.5 mm
Maximum stroke	40 mm
Mover weight	0.28 kg

Item /Symbol	Value/Unit
Stator	
Number of coils	15
Number of turns per coil	86-26AWG
Winding factor	0.8
Coil thickness	3 mm
Coil width	4.5 mm
Air-gap thickness s_c	1 mm
Stator weight	0.47 kg

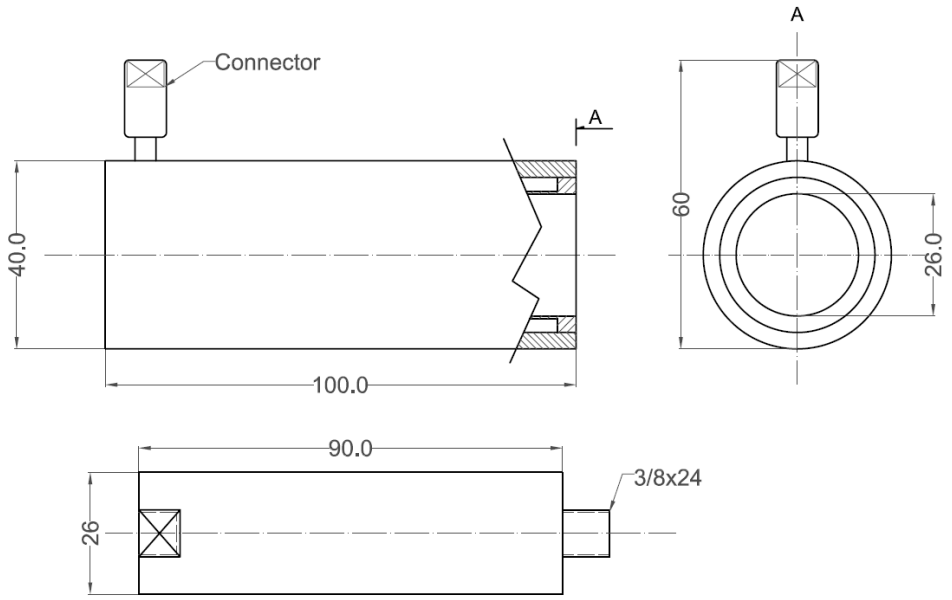

Fig. 4-5 Overall physical dimensions of the developed ED prototype.

The induced emf in the i^{th} phase depends on the flux linkage in the phase due to the magnets (λ_{PM}), and is

$$E = \frac{d\lambda_{PM}}{dt} = \frac{d\lambda_{PM}}{dz}\frac{dz}{dt}, \tag{4-8}$$

where

$$\lambda_{PM} = N\phi_g \cos((\pi/\tau)z). \tag{4-9}$$

N is the number of turns in the phase (Rhinefrank *et al.*, 2006). Therefore, for the first phase, (4-8) is simplified to

$$E_1 = \frac{d\lambda_{PM}}{dt} = -N\phi_g \frac{\pi}{\tau}\sin\left(\frac{\pi}{\tau}z\right)\frac{dz}{dt}. \tag{4-10}$$

Note that the induced emf in the second phase is shifted by 90°. The induced emf, obtained in (4-10), is verified with the FE, as well as the experimental results in Section 4.4.

4.3 Finite Element Modeling

Another approach for the modeling and simulation of the proposed ED is numerical modeling, primarily FE method. Comsol 3.4 is used for this purpose, and a 2D parametric model is generated and solved dynamically to model the 3D axial symmetry geometry of the ED. Since the generated model is parametric, it is possible to change the geometry of the problem quite easily and observe the variation of the damper characteristics.

Fig. 4-6 depicts the simple 2D axial-symmetric model of the proposed ED. The stator coils are stationary, whereas the slider moves in the axial direction with the frequency and amplitude equal to 10 Hz and 4 mm, respectively. The magnetic flux density streamlines and the induced current density, caused by relative motion of the magnetic flux and the coils, are plotted in this figure. The external currents applied to the coils are set to zero in this case.

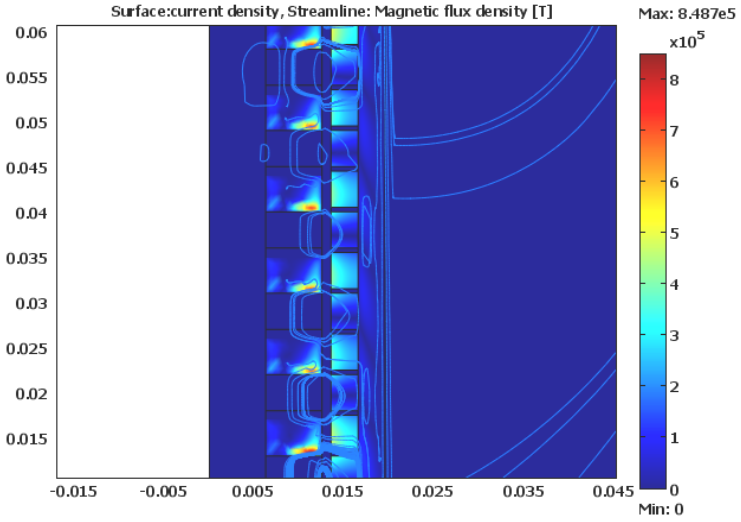

Fig. 4-6 Magnetic field streamlines of a 2D generated model using Comsol 3.3 for τ=1.8 τ_m.

Fig. 4-7 reflects the agreement of the numerical and analytical results for air-gap flux density and for the different τ / τ_m values. The error is less than 8% for this ratio. With a constant τ, increasing τ_m reduces the pole size and increases the air-gap flux density.

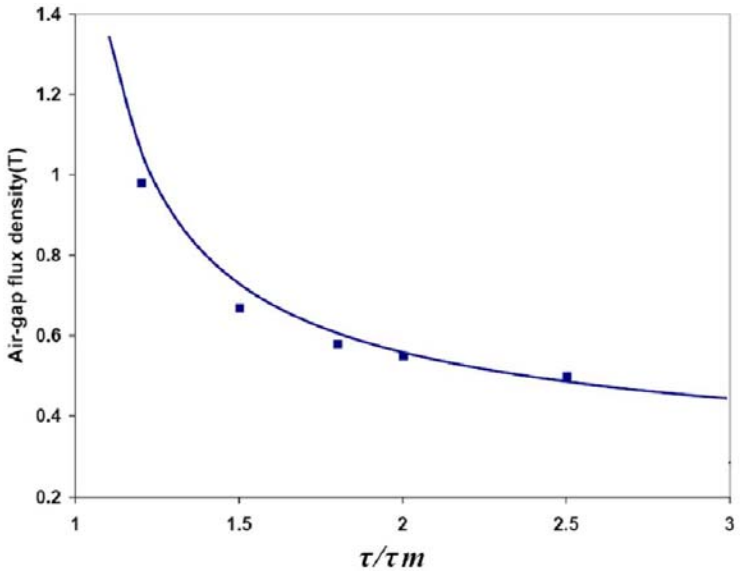

Fig. 4-7 Comparison of the analytical and FE results for the air-gap magnetic flux density. ——: Analytical, ■ :Comsol 3.4.

4.4 Prototyping and Experimental Analysis

A prototype ED is fabricated and experiments conducted to verify the accuracy of the numerical model. The fabricated prototype, consisting of the mover, stator coils and core, are illustrated separately in Fig. 4-8(a). Fig. 4-8(b) shows the fabricated prototype in the test-bed. The experimental test-bed consists of an LMS722 electromagnetic shaker, which is controlled by an accelerometer sensor feedback. An A/D board captures the data from the load-cell and the stator coils. The stator is connected to the fix load-cell while the mover is attached to the shaker. The measurements are taken at the University of Waterloo.

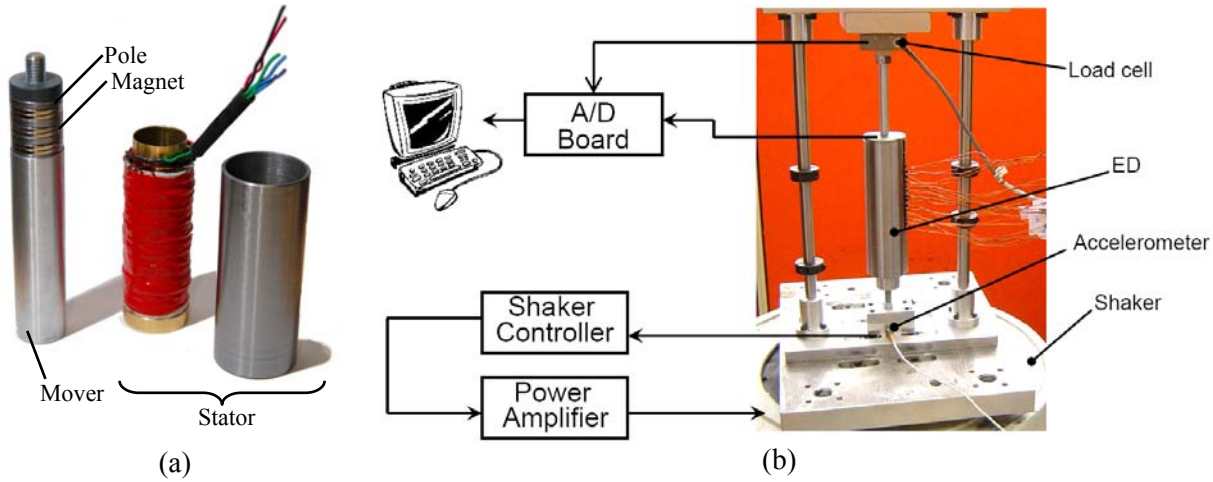

Fig. 4-8 (a) Fabricated prototype for proof of concept and (b) experimental test setup.

By selecting the amplitude and frequency of the mover vibration to be 4 mm and 25 Hz, respectively, the induced emf in the coils are measured experimentally and calculated with Comsol software. The induced emf (voltage) is plotted for each coil in Fig. 4-9 (the coil numbers are counted sequentially). There appears to be two bipolar phases for the current induction. The RMS value of the power loss per coil is measured to be 0.7 W at 0.62 m/s, such that the total power dissipation is equal to 10.5W.

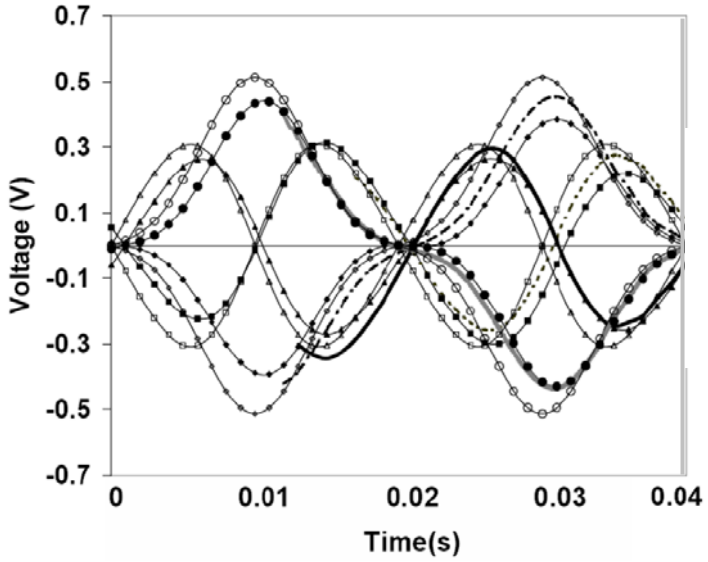

Fig. 4-9 Induced emf in each stator coil. —■—: Phase A+ (experimental), —◆—: Phase B+ (experimental),—▲—: Phase A- (experimental), —●—: Phase B- (experimental),▬ ▬: Phase A+ (FE),▬ ▪: Phase B+ (FE),▬▬: Phase A- (FE),▬▬: Phase B- (FE), —□—: Phase A+ (analytical),—○—: Phase B+ (analytical), —△—: Phase A- (analytical), —O—: Phase B- (analytical)

The analytical results in Fig. 4-9 are obtained from (4-10). It should be noted that the lag of the measured voltage with respect to the induced emf, is compensated in this figure.

4.5 Real-size Electromagnetic Damper Design

Considering a full-scale active electromagnetic damper as a stand-alone damper for automobile suspension application, the design procedure is presented in this section. As discussed in Chapter 2, the peak thrust force of 1300 N is required for the real-size electromagnetic damper to be used in an active suspension system. The general required geometry of the damper is also listed in Table 2-5. For a real-size ED, the tubular interior PM motor with moving magnets and slotless stator core configuration is selected for the initial design. Of the various design topologies of linear motors, the tubular PM configurations are particularly attractive because of their high thrust force density and high efficiency (Wang *et al.*, 2004). Fig. 4-10 shows the schematic view of the real-size damper configuration.

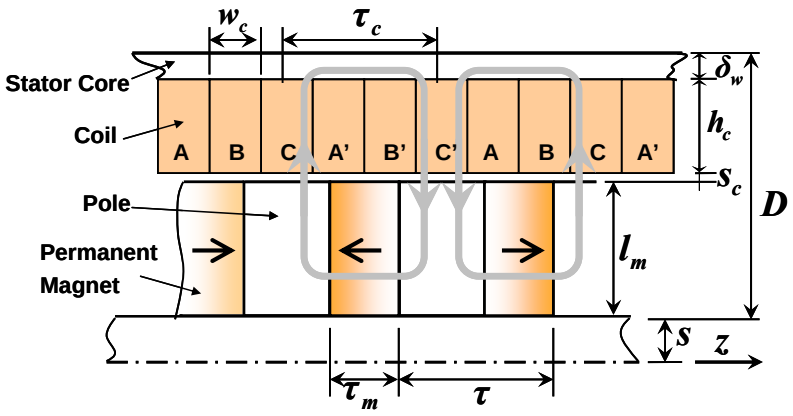

Fig. 4-10 Sketch of the slotless, tubular, linear, interior PM motor.

The ED operates in two major categories, depending on the road conditions: regenerative, and active. In regenerative mode, the electromagnetic component acts as a linear generator, harvesting the vehicle vibration energy and introducing additional passive damping to the suspension system. In contrast, the electrical energy is consumed in the active mode to actuate the system with an active force. The ED performance in those operating modes will be discussed in the following sections.

4.5.1 Regenerative Modes (Passive/semi-active)

In this section, the equivalent damping coefficient introduced in the regenerative mode is estimated, and the regenerated power is related to the disturbance input. The equivalent electrical circuit for each individual coil is shown in Fig. 4-11, where r_{int} and L_{int} are the resistance and inductance of the coil, and R_{ext} as the external resistance of the battery, characterizes the energy regeneration. The induced electromotive force in the coil is represented by E. Neglecting the coil's inductance, the maximum damping is achieved when the regenerative energy is zero (R_{ext}=0) *i.e.* the stator coils are short-circuited. In addition, the maximum energy regeneration occurs as the external resistance is set equal to the internal resistance. In the regenerative mode, the damper can be used in a passive or semi-active manner. In the passive mode, the external resistance is constant, causing a constant damping coefficient. In contrast, the damping coefficient in the semi-active mode can be increased/decreased relative to the passive mode, thereby decreasing/increasing the external resistance of the stator coils.

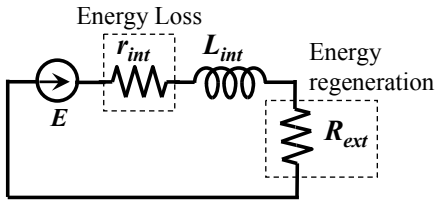

Fig. 4-11 Equivalent electrical circuit for each stator coil.

The voltage induced in each coil is proportional to the velocity (Rhinefrank *et al.*, 2006) and is derived from (4-10) as

$$E = \frac{d\lambda_{PM}}{dt} = -N\phi_g \frac{\pi}{\tau} \sin\left(\frac{\pi}{\tau} z + \theta\right) \frac{dz}{dt} \tag{4-11}$$

where θ is obtained with respect to the current phase shift in different phases. The total power loss for each coil (due to internal and external resistances) is obtained as

$$P = N_c \int_0^T E(t) I(t) dt = N_c \int_0^T \frac{E^2(t)}{R_{ext} + r_{\text{int}}} dt \tag{4-12}$$

where N_c and T are the number of coils, and the period of the oscillating voltage, respectively. The maximum power loss (that corresponds to the maximum achievable passive damping effect) is obtained by computing (4-12), considering short-circuited coils (R_{ext}=0). On the other hand, the maximum power regeneration is obtained from the same equation, substituting R_{ext}=r_{int}.

The total opposing force per coil in the generator case is calculated by

$$F = -N\phi_g \frac{\pi}{\tau} \hat{I} \cos\varphi \cos\left(\frac{\pi}{\tau} z + \theta\right) \tag{4-13}$$

where $\hat{I}$ and φ are the peak current and phase angle between the voltage and current in the coil, respectively (Rhinefranket *et al*., 2006).

4.5.2 Active Mode

In the active mode, the ED acts as a motor. The motor operates through the activation of the stator coils in a proper manner. Neglecting the flux-density reaction produced by the current with respect to the magnets flux, the peak value of the electric loading K_{sp} (the maximum current density distribution along the motor length) is obtained by

$$K_{sp} = \frac{N_c \lambda_c N}{p\tau} \hat{I}\,, \tag{4-14}$$

where N_c, p, and λ_c are number of coils, number of poles, and winding factor, respectively. The electric loading is restricted by either the magnetic limit or the thermal limit (Bianchi *et al.*, 2001):

• **Magnetic Limit**: The stator winding currents cause a reaction flux density that affects the PMs. The flux density variation in PMs is $\pm\Delta B_m$, and it is calculated by

$$\Delta B_m = \frac{16}{\pi^3} \frac{K_{sp}\tau}{\left(\left(2l_m + 2s\right)^2 - \left(2s\right)^2\right)\left(4R_{gap} + R_{mag}\right)}, \tag{4-15}$$

where R_{gap} and R_{mag} are the air-gap and magnet reluctances, respectively. The minimum magnetic flux density in the PM must be higher than a certain amount to avoid an irreversible demagnetization (Bianchi *et al.*, 2001). The electric loading can be calculated due to this magnetic limit.

• **Thermal Limit**: The winding temperature rise should be considered as another limit on the electric loading. This limit is more restrictive than the magnetic limit in most cases (Bianchi *et al.*, 2003). The copper losses (P_{Cu}) are computed by the thermal analysis and given by

$$P_{Cu} = N_c \frac{\pi N^2 (D + l_m + 2s)}{\sigma \lambda S_{cu}} \left[\frac{p\tau K_{sp}}{N_c \lambda_c N}\right]^2 = \frac{\pi p^2 \tau^2 (D + l_m + 2s)}{\sigma N_c \lambda_c^3 S_{cu}} {K_{sp}}^2, \tag{4-16}$$

where S_{cu} is the stator coils' cross-section area. The generated heat is transferred through the external surface ($A_e = 2\pi(D+s)p\tau$). The winding temperature rise θ_w is related to P_{Cu} by

$$P_{Cu} = h\theta_w (2\pi(D+s)p\tau)\,, \tag{4-17}$$

where h is the overall heat transfer coefficient. Eq. (4-17) is rewritten in terms of the thermal resistances between the coil and stator core (R_w), and between the stator core and the external air (R_e) as

$$P_{Cu} = \frac{\theta_w}{R_w + R_e} = \frac{\theta_w}{\frac{\ln[(D+s-\delta_w)/(l_m+s+g)]}{K 2\pi p \tau} + \frac{1}{h_N A_e}}, \tag{4-18}$$

where K and h_N are the thermal conductivity of iron and the natural-convection heat transfer coefficient. Two values of the electric loading K_{sp} are calculated from (4-15) (setting ΔB=0.7 T) and (4-16) (considering the maximum winding temperature rise $\theta_w = 125^{\circ C}$), and the lowest one is considered. The maximum force developed by the electromagnetic damper is obtained by computing

$$F = 4p(l_m + s + g)\tau K_{sp} B_g \sin\left(\frac{\pi}{2}\frac{(\tau - \tau m)}{\tau}\right), \tag{4-19}$$

where B_g is the air-gap flux density (Bianchi *et al.*, 2001).

4.5.3 Initial Design Procedure

For the electromagnetic damper to generate a peak active force of 1300 N (as derived in Section 2.4), a number of geometrical dimensions have to be selected and optimized to achieve the required active force with the lowest damper weight and volume.

Following the same procedure described in Section 4.1, the ratio of PMs' thickness τ_m to the pole pitch τ is set equal to 0.5 (Bianchi *et al.* (2001) have suggested this ratio to be around 0.55). Setting the pole pitch, mover's rod and air-gap sizes constant and equal to τ=24 mm, s=5 mm, and s_c=0.5 mm, respectively, other geometry dimensions such as: l_m, D, h_c, and δ_w are obtained, following the subsequent procedure. The two most important non-dimensional geometry factors that have to be optimized are the l_m / D and δ_w / h_c. Having these two ratios determined, all geometry factors will be obtained with respect to the D value, which is set based on the damper's outer diameter restrictions. For different combination of those two ratios, finite element simulations are done in the Comsol 3.4 environment to find the average radial flux density over each coil; this is accomplished by integrating

the radial flux density over the coils' surface and then dividing it by the coils' surface area. It should be mentioned that the use of average flux density (obtained from finite element analysis) enhances the modeling accuracy because the iron permeability, leakage flux, and ending effects are all considered in the calculations.

Exploiting the average value of the radial flux density and assuming a constant value for the number of poles, the peak electric loading (K_{sp}) is obtained from either the thermal limit (4-16), or the magnetic limit (4-15) (the one with the lower K_{sp} value). Thus, the peak force is estimated using (4-19). The results for the peak motor force are divided by the motor weight and listed in Table 4-2 for different l_m / D ratios. These results are also plotted in Fig. 4-12 illustrating the behavior of the motor in terms of peak force/weight ratio for different combinations of l_m / D and δ_w / h_c. It should be mentioned that the results in Table 4-2 are independent of the number of poles selected.

Table 4-2 Mean radial flux density and force/weight ratio for different geometrical dimensions.

h_c	7 (mm)	6 (mm)	5 (mm)	4 (mm)	3 (mm)	2 (mm)	1 (mm)
δ_w	2.5 (mm)	3.5 (mm)	4.5 (mm)	5.5 (mm)	6.5 (mm)	7.5 (mm)	8.5 (mm)
B_{r_ave} (l_m/D=0.8)	0.68 (T)	0.76 (T)	0.87 (T)	1.01 (T)	1.2 (T)	1.46 (T)	1.87 (T)
B_{r_ave} (l_m/D=0.75)	0.62 (T)	0.69 (T)	0.8 (T)	0.92 (T)	1.07 (T)	1.29 (T)	1.6 (T)
B_{r_ave} (l_m/D=0.66)	0.52 (T)	0.6 (T)	0.67 (T)	0.77 (T)	0.89 (T)	1.05 (T)	1.3 (T)
Peak_force/weight (l_m/D=0.8)	79.2 (N/kg)	81.8 (N/kg)	85.7 (N/kg)	88.9 (N/kg)	90.9 (N/kg)	89.6 (N/kg)	81.1 (N/kg)
Peak_force/weight (l_m/D=0.75)	89.6 (N/kg)	92.4 (N/kg)	97.6 (N/kg)	100.4 (N/kg)	100.8 (N/kg)	98.4 (N/kg)	87.3 (N/kg)
Peak_force/weight (l_m/D=0.66)	85.9 (N/kg)	89.6 (N/kg)	92.9 (N/kg)	95.4 (N/kg)	92.6 (N/kg)	92.6 (N/kg)	82.9 (N/kg)

As shown in Fig. 4-12, the optimum value of the δ_w / h_c ratio is around 2 (other values are suggested by other authors such as 0.67 by Bianchi *et al.* (2001)). Also, the l_m / D ratio (one of the key ratios in linear motor design) is found to be optimal at 0.75. Setting the external diameter of the damper as 120 mm, the D value is obtained as 55 mm, and so other parameters are consequently obtained. Designing for a three-phase electromagnetic actuator, and setting the same coil's pitch, τ_s, as the pole's pitch,

the coils' width is obtained as $w_c = 8\,\text{mm}$. The final design details of the electromagnetic damper are listed in Table 4-3. Also, for the final design, the air-gap radial flux density distribution over the mover length is plotted in Fig. 4-13.

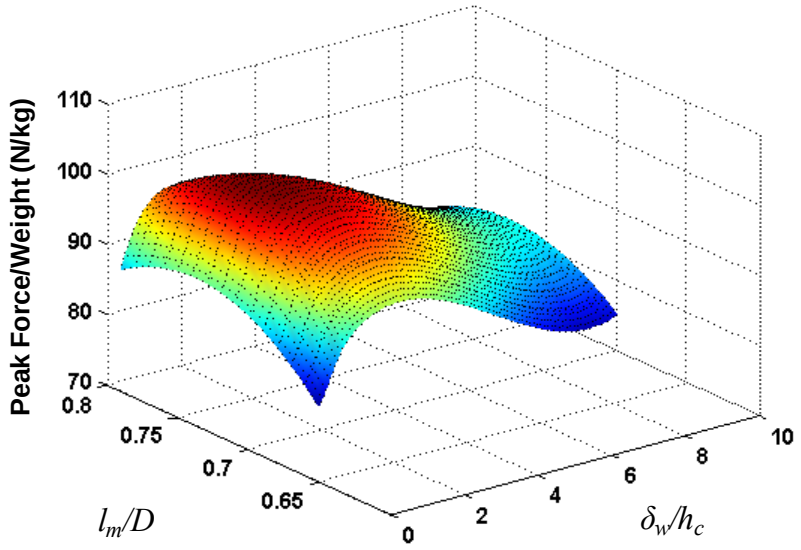

Fig. 4-12 Peak motor force/weight for different l_m/D and δ_w/h_c values.

Table 4-3 Specifications of the real-size electromagnetic damper.

Item /Symbol	Value/Unit
Mover	
Number of poles p	12
Pole pitch τ	24 mm
Magnets thickness τ_m	12 mm
Magnets outside diameter $2(l_m + s)$	90 mm
Rod diameter $2s$	10 mm
Rod material	Al alloy
Mover weight	8 kg
Magnets material	Nd-Fe-B B_r=1.17T

Item /Symbol	Value/Unit
Stator	
Number of coils N_c	3×12
Number of turns per coil N	230-26AWG
Winding factor	0.8
Coil thickness h_c	4.5 mm
Coil width w_c	8 mm
Air-gap thickness s_c	0.5 mm
Stator weight	3.8 kg
Stator material	low Carbon Steel (A36)

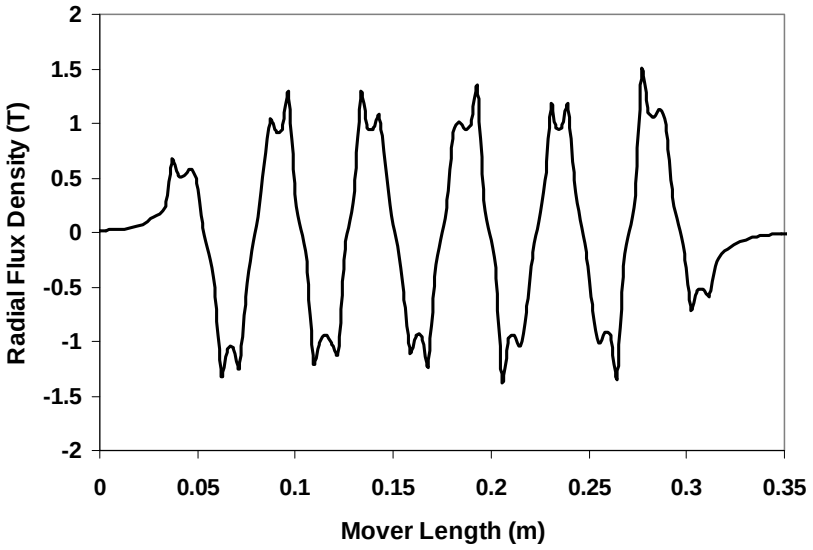

Fig. 4-13 Air-gap radial flux density distribution along the mover's length.

The overall length, external diameter, and weight of the electromagnetic damper are obtained as 350 mm, 120 mm, and 11.8 kg (excluding the driver, amplifier and other electronic equipments), respectively.

The designed electromagnetic damper, *as a generator*, with the specification given in Table 4-3, has a maximum damping coefficient equal to 9000 Ns/m (in case all coils are short-circuited and there is no power generation). The maximum damping coefficient caused by eddy current loss in the stator iron core (the damping coefficient in the off mode) is calculated equal to 550 Ns/m, which is well below the range of acceptable damping coefficient. Assuming the disturbance input of 11 mm at 10 Hz (the resonant frequency of unsprung-mass) the maximum power loss in the coils (that corresponds to the maximum achievable passive damping effect, when R_{ext}=0) is calculated as 1.3 kW per damper by computing (4-12). The maximum power regeneration (R_{ext}=r_{int}) is also calculated as 320 W from (4-12) for each damper.

In the *active mode*, the peak electric loading for the ED with the proposed dimensions is obtained from (4-16) equal to $K_{sp} = 2.4\times10^4$ A/m, resulting in a peak current of $\hat{I} = 1\,\text{A}$ in the stator coils. While the average radial flux density over the stator coils are 0.94 T, the maximum achievable force for the ED in the active-mode $F = 1200\,\text{N}$ is obtained from (4-19), requiring 370 W of electrical power for each ED.

4.5.4 Electrical and Mechanical Time-constants

The electrical and mechanical time-constants of a moving magnet type linear motor is studied by Mizuno *et al.* (2000). Electrical time-constant is simply obtained from the electrical resistance R and inductance L of each stator coil as

$$\tau_e = L / R \,. \tag{4-20}$$

The method proposed by Wheeler (1942) could be used for inductance calculation of circular coils, and is particularly useful when analytical expression is needed. The following equation is proposed for inductance estimation of a finite length solenoid with a mean radius of a and width w_c.

$$L \approx \frac{10\pi.\mu_0.N^2a^2}{9a+10w_c}, \tag{4-21}$$

where N and μ_o are the number of turns and the permeability of free space, respectively. Considering the stator coils information in Table 4-3, the inductance L is obtained as 9.2 mH, leading to an electrical time-constant of $\tau_e \simeq 1$ ms (R=9.3 Ω).

Yajima *et al.* (2000) have defined the mechanical time-constant (τ_m) as the time when the mover velocity reaches 63% of its final state, and proposed the following simplified equation:

$$\tau_m = \frac{mR}{K_f^2}, \tag{4-22}$$

where m is sum of the mover and load masses, and K_f is the thrust constant (N/A). For the moving magnet design, the thrust constant K_f is obtained from

$$K_f = \frac{\phi_m}{\tau}(p+1)N, \tag{4-23}$$

where ϕ_m is the magnetic flux due to the PMs, p is the number of poles and τ is the pole pitch. For the proposed real-size ED, the mechanical time-constant is obtained from (4-22) as ~3 ms with the overall m=50 kg.

4.5.5 Potential Design Modifications

There are a number of potential design modifications that cause design compromises; these will be discussed in greater detail in this section.

4.5.5.1 Halbach Array Configuration for the Mover

As described in Section 3.3, the Halbach array is the most efficient magnet arrangement that augments the magnetic field on one side of the array while eliminating the flux leakage from the inner (rod) side. Utilizing the Halbach arrangement for the magnets in the mover requires the use of radially-magnetized PMs, which are costly and rare.

Following the same procedure described in Section 4.5.3, and estimating the radial flux density from the finite element simulation, reveals that the force/weight ratio is increased 2.5% by using the Halbach magnets arrangement, and the maximum thrust fore of 1230 N is achievable. Fig. 4-14 depicts the air-gap flux density distribution for the two cases. Considering the cost issue, the use of the Halbach arrangement is not appealing for the initial design modification.

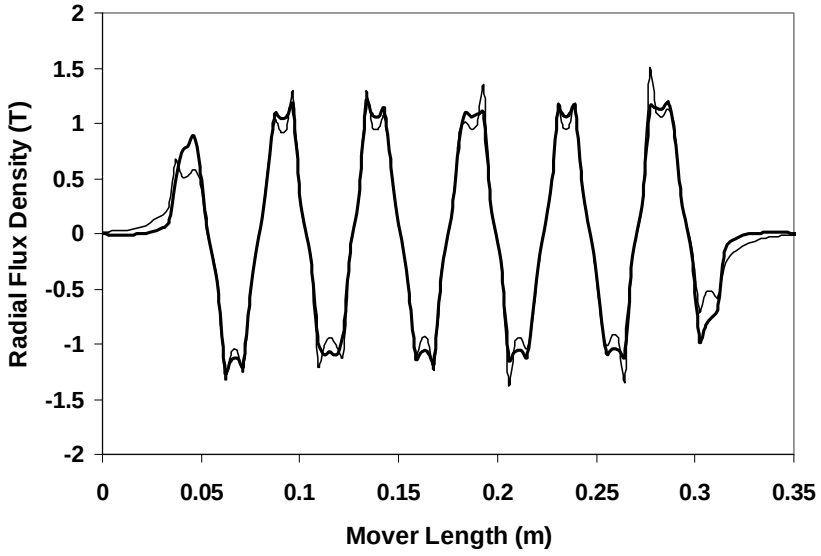

Fig. 4-14 Air-gap radial flux density distribution comparison for: ——: Halbach array and ——: initial design, axially-magnetized arrangement.

4.5.5.2 Disk Shaped Magnets vs. Annular Shaped Ones in the Mover

Another modification is to utilize disk shaped PMs, which are supported by a nonmagnetic tube, instead of the described annular shaped magnets, which are supported by a non-ferromagnetic rod. As mentioned previously, the latter design eliminates the difficulties involved in the thin tube manufacturing and reduces the volume of PM material, while the former design saves more overall volume and weight, omitting the linear guides.

Having done the finite element simulation for both configurations, it is revealed that the force/weight ratio of the disk-shaped configuration is slightly reduced compared to that of the annular-shaped design, despite the fact that it requires ~1.6% more PM material while the force is increased ~1.1%. It should be mentioned that this is not a general conclusion for the two configuration comparisons. Nevertheless, some authors suggest using the ring-shaped configuration rather than its disk-shaped counterpart (Wang *et al.*, 2004).

4.5.5.3 Slotless vs. Slotted Configuration

Among potential design modifications to the current design is switching to the slotted stator core configuration instead of the current slotless design. Bianchi *et al.*, (2001) have observed that the force/weight ratio could be increased up to ~20% (depending on the l_m/D ratio), using the slotted stator design. Generally, they have demonstrated that for large external diameters (larger than 50 mm), the higher force/weight ratio is achieved with slotted motor, while for smaller external diameters, the slotless solution is preferred. Together with higher force density, in the case of the slotted stator configuration, the design would be more complex; other issues and factors also come into play. The iron saturation effect should be considered, with the effect of limiting the highest achievable magnetic flux density. In addition, the ripple forces are very high, especially for high magnet's thickness (τ_m). The ripple/cogging force is produced by the interaction between the magnets and the slotted iron structure as well as the finite length of the stator. The force attempts to maintain the alignment between the magnets and teeth. The cogging force exists even if there is no current flowing in the coils (Nor *et al.*, 2004). The cogging force produces a pulsating force ripple that causes step-like obstruction (Arof *et al.*, 2004). In order to reduce the ripple forces, some strategies have been adopted in motor design, such as PM shifting/skewing, causing the mean force to

reduce. The pole-shifting is achieved by replacing the iron poles with the same width, and iron poles with different widths, causing an asymmetrical configuration (Bianchi *et al.*, 2003).

4.6 Conclusions

In this chapter, the concept of the Electromagnetic Damper (ED) is introduced and the design procedure for an active stand-alone ED for an active suspension system is presented in this chapter. Among various potential technologies and topologies, the linear motor concept is chosen. Several design approaches are considered, and a tubular, interior, slotless PM motor is selected to achieve higher efficiency and simpler manufacturing. An analytical approach based on magnetic circuit principles, is employed for the initial design of a prototype ED, and non-dimensional, geometrical design parameters are optimized to obtain the highest damping coefficient in the passive mode. Next, the Finite Element (FE) approach is used to validate the analytical method, which confirms the consistent results for the air-gap magnetic flux density. After a prototype ED is fabricated, experiments are carried out to verify the numerical model for the induced emf in each stator coil.

Finally, an active full-scale ED for an automotive suspension application is designed, and the maximum achievable damping coefficient and force in the semi-active and active modes are estimated. The key non-dimensional parameters for the design of the ED are described to achieve the highest force/weight ratio. FE analysis is coupled with analytical models to estimate/simulate the real-size damper performance. The design procedure presented in Section 4.4, is based on an analytical model, while the FE technique is utilized at some stages to guarantee the modeling accuracy, enhancing the simulation. A good agreement between the results of the analytical model with data obtained from FE analysis is recognized, comparing the magnetic field quantities. The final specifications of the designed ED are listed in Table 4-4. According to the required specifications listed in Table 2-5, the geometry and force requirements are satisfied with the proposed design. Also, the mechanical time-constant around 3 ms is much less than that of semi-active dampers (~15-25 ms). However, the weight of the designed ED is much higher than that of the off-the-shelf, semi-active and passive dampers (almost three times higher than semi-active MR dampers in the market).

The ED developed in this chapter operates in passive, semi-active, and active modes. The stator coils are short-circuited in passive mode. The damping coefficient could be controlled rapidly and

reliably by regulating the induced current in the stator coils. The coils are energized in the active mode to achieve an active suspension system.

Table 4-4 Final Specifications of the designed ED.

Quantity	Value (Unit)
Peak Force	1200 N
Overall Length	350 mm
Max. Diameter	120 mm
Weight	11.8 kg
Max. Stroke	160 mm

Together with the superb performance of active suspension (described in Section 2.3), there are still some issues that have to be overcome. The proposed active ED, with specifications listed in Table 4-4, has high energy consumption (370 W for one unit, maximum force), it is not fail-safe in case of power outage, and is very heavy. Therefore, the next challenge would be addressing these drawbacks through the introduction of hybrid dampers in the next chapter.

Chapter 5

Hybrid Damper Design

5.1 Conceptual Design

After having investigated the electromagnetic and eddy current damping concepts, the feasibility of adding passive damping to an active electromagnetic damper in a hybrid active suspension is studied in this chapter. Fig. 5-1 shows the block diagram of a hybrid electromagnetic single-wheel suspension system. The electromagnetic actuator and the passive damper form the hybrid electromagnetic unit. The electromagnetic portion of the system is the only source of variable damping. The passive damping, caused by hydraulic/eddy current forces, provides the required level of damping. This is to ensure that, in the event of an electrical failure, a minimum level of damping is available from the passive portion of the system. The active electromagnetic actuator operates in passive/active modes, allowing partial energy recovery from the vehicle vibration. This configuration allows the use of a smaller and lighter electromagnetic actuator, retaining the performance level of active suspension systems.

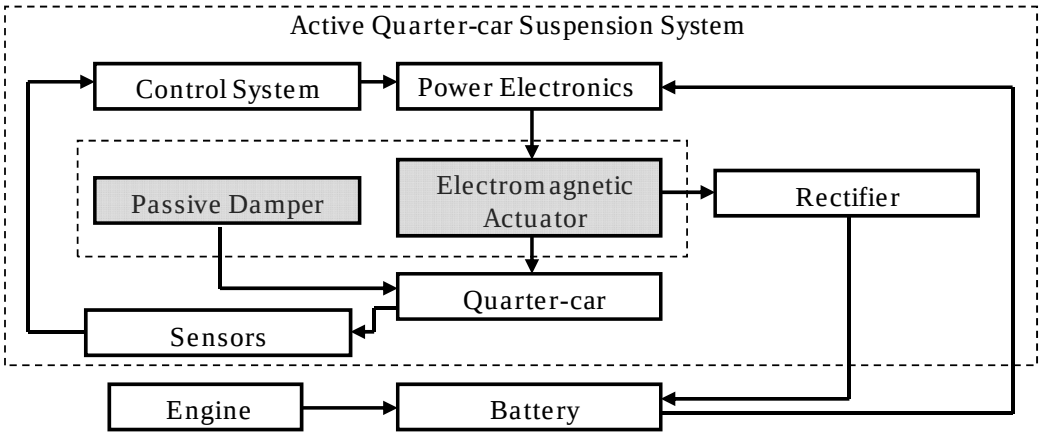

Fig. 5-1 Block diagram of a hybrid electromagnetic suspension system for a quarter-car.

After driving the damper design requirements in Chapter 2, two configurations are proposed for the hybrid damper design in this chapter. The first configuration utilizes hydraulic forces to provide the essential passive damping, while the second design operates based on the eddy current damping phenomenon. As mentioned previously, the passive damping in hybrid dampers makes the suspension system, fail-proof, reduces the amount of energy consumption in an active suspension system, and allows for a lighter and less expensive active suspension system.

5.1.1 Configuration One: Mono-tube Electromagnetic/Hydraulic

Modern hydraulic dampers consist of both twin-tube and mono-tube types. Mono-tube shock absorbers consist of a single cylinder filled with oil, and a piston with an orifice moving through the cylinder. Fig. 5-2 depicts the first proposed configuration as the electromagnetic/hydraulic hybrid damper.

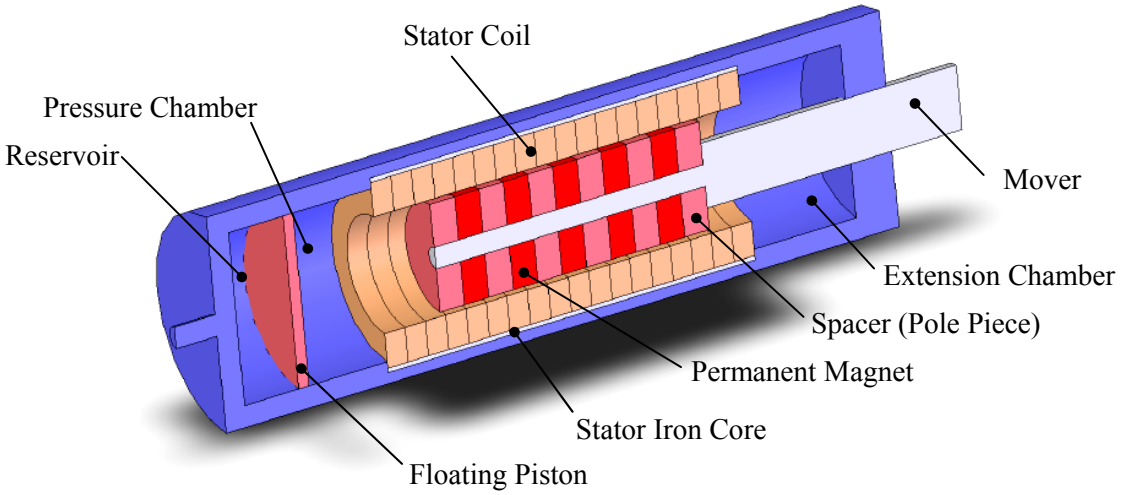

Fig. 5-2 Schematic view of the mono-tube hybrid electromagnetic/hydraulic damper.

The electromagnetic subsystem comprises a linear tubular permanent magnet motor with moving magnets. The moving magnets attached to the rod and their gap with the stator coils form the piston and its orifice in the hydraulic subsystem. The fluid movement causes a pressure drop between the compression chamber and the extension chamber, resulting in a drag force to be exerted through the rod. Pressurized gas is included in the damper, either in an emulsion with the oil or separated from the oil with a floating piston in a compressible accumulator-like chamber. The gas chamber allows the

volume of the piston rod to enter the damper without causing a hydraulic lock. The gas also adds a spring effect to the force generated by the damper and maintains the damper at its extended length when no force is applied (Gillespie, 2006).

Mono-tube dampers are typically simpler for manufacturing compared to the twin-tube ones, but require higher gas pressures to operate properly. Although twin-tube dampers are more complex, they operate with lower gas pressure and are not as susceptible to damage. The electromagnetic and hydraulic subsystems of the hybrid damper are discussed in Sections 5.2 and 5.3, respectively.

5.1.2 Configuration Two: Electromagnetic/Eddy Current

Another alternative configuration for the hybrid damper is shown in Fig. 5-3, utilizing the eddy current damping effect to provide the required passive damping effect.

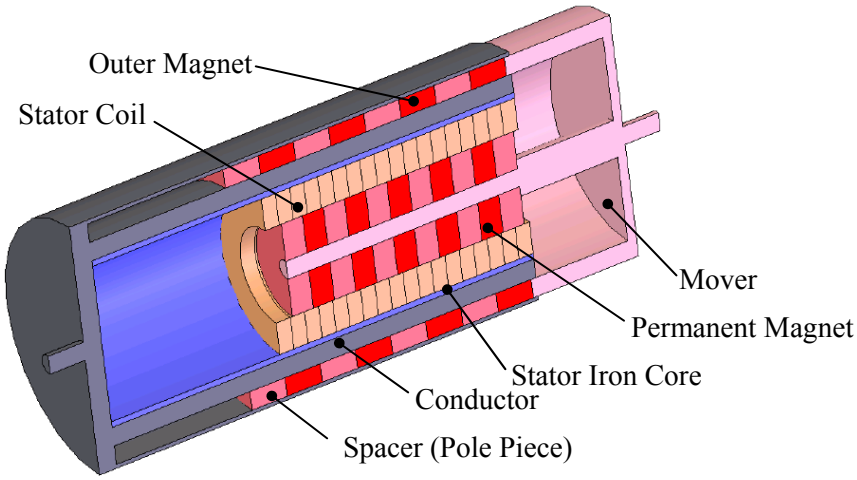

Fig. 5-3 Schematic view of the hybrid electromagnetic/eddy damper.

As illustrated in Fig. 5-3, the damper consists of an inner linear tubular electromagnetic motor as the active part of the damper and a source of the variable damping. The motor's stator tube is encircled by a conductor tube. There is another outer Permanent Magnet (PM) annular part that moves relative to the aforementioned conductor tube, generating eddy currents in the conductor. The induced eddy currents generate a repulsive damping force proportional to the relative velocity of the conductor and magnets, causing a passive viscous damping effect.

The hybrid damper design continues with an electromagnetic analysis, followed by the design of electromagnetic subsystem dimensions. Then, a general methodology for the hydraulic damper design is discussed, following by the final design of the first hybrid damper. Finally, the eddy current damping effect in the second hybrid damper configuration is investigated, and its final design is presented based on the aforementioned design requirements.

5.2 Active Electromagnetic Subsystem

5.2.1 Initial Sizing

The design procedure for the active electromagnetic subsystem of the hybrid damper is similar to the method described in Section 4.5.3. Following the aforementioned proposed topology, the linear interior PM motor with slotless stator core and the same arrangement for magnets in the mover is selected. Similarly, Fig. 4-10 illustrates the active electromagnetic subsystem of the hybrid damper. As the electromagnetic portion of both hybrid damper configurations is similar, a general approach for the design is proposed. Again, the goal is to design the geometry of the electromagnetic part of the hybrid damper, achieving the required active force (~350 N) based on the assigned volume restriction. The following sets of non-dimension ratios are derived in Section 4.5.3 and used to estimate the overall dimensions of the magnets and coils:

$$\begin{aligned} \tau_m / \tau &= 0.5, \\ l_m / D &= 0.75, \\ \delta_w / h_c &= 1.7. \end{aligned} \tag{5-1}$$

As mentioned before, the axially-magnetized PMs in the mover are utilized, achieving a higher thrust force density and higher efficiency than other candidate topologies. This topology also has advantages for ease and cost of manufacturing. Based on the external diameter restriction, and manufacturing limits for air-gap, the following sizes are sets: D=40 mm, s_c=0.5 mm, s=5 mm, and τ=24 mm. The magnets, coils and stator core dimensions are obtained from (5-1) and are listed in Table 5-1. Also, for a three-phase electromagnetic actuator, coil's pitch τ_s is set equal to the pole's pitch, and so the coils' width are obtained as w_c=8 mm.

As described in Section 4.5.3, the average radial flux density over stator coils is obtained from a finite element simulation. Then, this number, together with the peak electric loading (K_{sp}) from (4-16)

is implemented in (4-19) to find the peak force. Therefore, for a certain required peak force ~350 N (as listed in Table 2-4) the required number of poles is four.

Table 5-1 Specification of the proposed electromagnetic damper.

Item /Symbol	Value/Unit
Mover	
Number of poles p	4
Pole pitch τ	24 mm
Magnets thickness τ_m	12 mm
Magnets outside diameter $2(l_m + s)$	70 mm
Rod diameter $2s$	10 mm
Rod material	Al alloy
Mover weight	1.4 kg
Magnets material	Nd-Fe-B B_r=1.17T

Item /Symbol	Value/Unit
Stator	
Min. number of coils N_c	3×4
Number of turns per coil N	180-26AWG
Winding factor	0.8
Coil thickness h_c	3.5 mm
Coil width w_c	8 mm
Air-gap thickness s_c	0.5 mm
Stator weight	2 kg
Stator material	low Carbon Steel (A36)

Table 5-2 represents the overall dimensions of the active part in hybrid dampers. It is seen that the active subsystem is feasible based on the aforementioned requirements.

Table 5-2 Typical dimension of the electromagnetic subsystem for hybrid dampers.

Quantity	Value
Max. diameter 2(D+s)	90 mm
Mover length L_{am}	96 mm
Total weight	3.4 kg
Peak force	320 N

As stated previously, the electromagnetic subsystem can operate in two basic categories: regenerative mode and active mode. In regenerative mode, with the specification given in Table 5-2, the maximum damping coefficient equal 2100 Ns/m (in case all coils are short-circuited, and there is no power generation) can be achieved. The maximum damping coefficient caused by eddy current loss in the stator iron core is calculated equal to 180 Ns/m. Assuming a disturbance input of 11 mm at 10 Hz (resonant frequency of unsprung-mass) the maximum power loss in the coils (corresponds to

R_{ext}=0) is calculated as 0.65 kW per damper by computing (4-12). The maximum power regeneration (R_{ext}=r_{int}) is also calculated as 160 W from (4-12) for each damper.

In the active mode, the peak electric loading for the active part of the hybrid damper is obtained from (4-16) equal to $K_{sp} = 2.1\times10^4$ A/m, resulting in a peak current of $\hat{I} = 1.1$ A in the stator coils. While the average radial flux density over the stator coils are 1.1 T, the maximum achievable force in the active-mode $F = 320$ N is obtained from (4-19), requiring 95 W of electrical power for each damper.

5.3 Fluid Analysis

5.3.1 General Design Method

In this section, a general approach for the design of an oil damper is proposed. The goal is to express the fluid behavior in an oil damper in terms of parameters and equations that address general damping performance in order to achieve the damper design requirements.

It is possible to achieve a wide range of force-velocity curves by selecting the valve parameters. Generally, a reducing damping coefficient with speed is preferred. Fig. 5-4 depicts a general damper configuration, consisting of a reservoir and the main body. The reservoir accommodates volume changes due to the rod movement and might be designed in alternative ways, such as around the main body in case of a twin-tube damper.

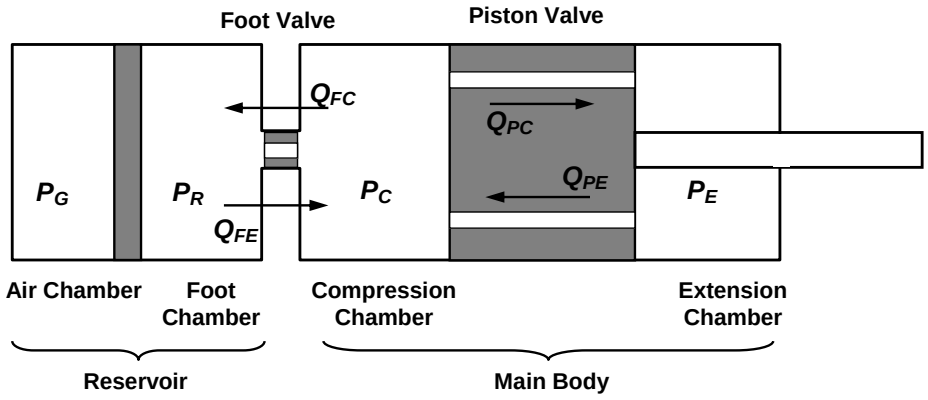

Fig. 5-4 General damper configuration (Dixon, 1999).

The main body consists of a piston separating the compression and extension chambers. The piston/mover utilizes two valves - one controlling the flow through the compression, and the other one working in extension.

As the damper is compressed, the piston is displaced by distance x to the left, and the volume taken up by the rod causes the compression of the gas in the reservoir. Assuming an incompressible fluid, the volumetric flow rate moves through the foot valve, Q_{FC}, and through the piston valve, Q_{PC}, during the compression are obtained from (5-2), where A_R, A_P, and V_C are cross-section areas of rod and piston and compression velocity, respectively. It should be mentioned that the absolute value is used for all the parameters in this section. Similar equations are derived during the extension stage in (5-2).

$$Compression\begin{cases} Q_{FC} = A_R V_C \\ Q_{PC} = (A_P - A_R)V_C \end{cases} \qquad Extension\begin{cases} Q_{FE} = A_R V_E \\ Q_{PE} = (A_P - A_R)V_E \end{cases} \tag{5-2}$$

Considering linear valves, the pressure-drops across the foot, $P_{FC,}$ and piston, $P_{PC,}$ valves during compression are obtained in (5-3), where C_{FC} and C_{PC} are discharge coefficients of the foot and piston valves during the compression. Similarly, the pressure-drops across the foot and piston valves in extension are presented in (5-3).

$$Compression\begin{cases} P_{FC} = C_{FC}Q_{FC} \\ P_{PC} = C_{PC}Q_{PC} \end{cases} \qquad Extension\begin{cases} P_{FE} = C_{FE}Q_{FE} \\ P_{PE} = C_{PE}Q_{PE} \end{cases} \tag{5-3}$$

So, in compression/extension, the compression and extension chamber pressures, P_C and P_E are derived in (5-4) as:

$$Compression\begin{cases} P_C = P_R + P_{FC} \\ P_E = P_C - P_{PC} \end{cases} \qquad Extension\begin{cases} P_C = P_R - P_{FE} \\ P_E = P_C + P_{PE} \end{cases} \tag{5-4}$$

Regarding the free body diagram of the piston in the compression stage, as shown in Fig. 5-5, the total force along the x direction is

$$\sum F_x = F_{ext} - P_C A_P + P_E(A_P - A_R) + F_f = m_P \ddot{x}\,. \tag{5-5}$$

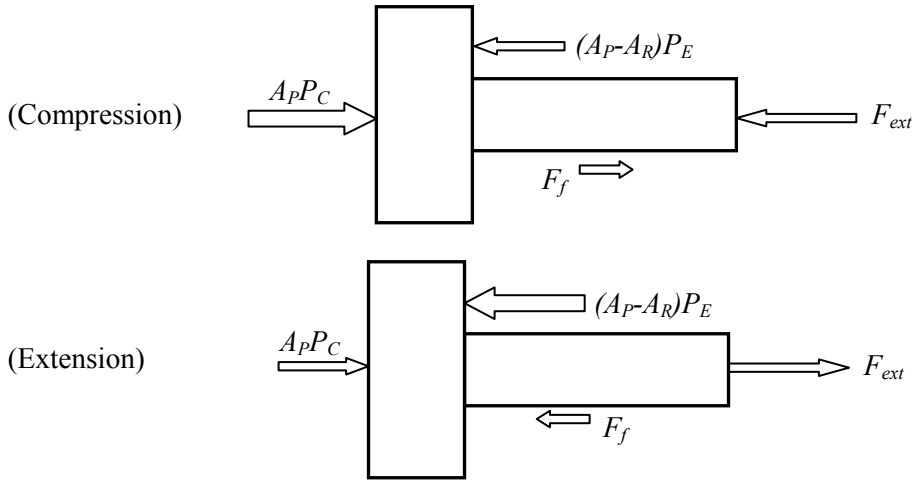

Fig. 5-5 Piston free body diagram in compression/extension.

Considering the piston mass ~3kg from the electromagnetic active part design in Section 5.2, and an average stroke of 11 mm at 10 Hz (giving an acceleration of ~43 m/s^2), the acceleration force is calculated in the order of 100 N and is negligible compared to the damping force about 2 KN. The friction force F_f is difficult to calculate and depends on the pressure forces and the sealing condition. However, although the friction force is difficult to calculate, it does not give an objectionable characteristic (Dixon, 1999) and neglected in the design. Consequently, during the compression stage the force on the piston due to the fluid pressure, F_{PC} is

$$F_{PC} = P_C A_P - P_E (A_P - A_R) = P_R A_R + \left[C_{FC} A_R^2 + C_{PC} (A_P - A_R)^2 \right] V_C \,. \tag{5-6}$$

A Similar expression is obtained for the extension stage

$$F_{PE} = -P_R A_R + \left[C_{FE} A_R^2 + C_{PE} (A_P - A_R)^2 \right] V_E \,. \tag{5-7}$$

It is seen that the linear valve assumption (linear $P(Q)$) results in a linear damping force–velocity behavior, where the reservoir pressure acting on the rod area provides a static force, independent of velocity. The force-velocity curve was mentioned as the most important damper requirement in the previous section. The force-velocity curve is obtained from the valve characteristics on the basis of steady-state analysis (Dixon, 1999). Dampers are required to exhibit asymmetric characteristics in compression-extension cycles. So, different coefficients are used for modeling the damper behavior.

$$F_C = F_S + C_C V_C,$$
$$F_E = F_S + C_E V_E. \tag{5-8}$$

where, the average damping coefficient C_D is the mean value of the compression damping coefficient C_C, and the extension damping coefficient C_E. The compression/extension ratio, R_{CE} is

$$R_{CE} = \frac{C_C}{C_E}. \tag{5-9}$$

The static force (*Fs*) should be overcome as the damper's rod is moved in and out from the central position. Although the main damper forces are velocity dependent, there are some static stiffness characteristics that have to be considered. The static force *Fs* results from the static compression chamber pressure times the rod area (Dixon, 1999):

$$F_S = P_C A_R. \tag{5-10}$$

Rod insertion causes an increase in internal pressure and so static stiffness occurs. This static force depends on rod area, stroke, and internal pressure, and is not a constant value: it is likely to increase ~20% over the whole stroke. However, the resultant stiffness will be a small percentage of the suspension spring stiffness, and might be ignored in the modeling (Dixon, 1999). Although the damper exhibits greater damping than the damping provided by the valves and fluid friction alone, because of the additional frictions in the damper, the correlation between the valve coefficients and the required damping coefficient can be expressed assuming linear behavior.

In Extension, assuming a small foot valve discharge coefficient in extension, (5-7) is simplified as

$$F_{PE} = -P_R A_R + C_{PE}(A_P - A_R)^2 V_E. \tag{5-11}$$

So, the extension damping coefficient is

$$C_E = \frac{dF_{PE}}{dV_E} = C_{PE}(A_P - A_R)^2, \tag{5-12}$$

and the piston valve discharge coefficient in extension, C_{PE}, can be derived from the extension damping coefficient requirement using

$$C_{PE} = \frac{C_E}{(A_P - A_R)^2}. \tag{5-13}$$

In compression, the compression damping coefficient is obtained in a similar way from (5-6)

$$C_C = \frac{dF_{PC}}{dV_C} = C_{FC} A_R^2 + C_{PC}(A_P - A_R)^2 . \tag{5-14}$$

In conclusion, Eqs. (5-13) and (5-14) can be used to derive the initial design for the piston/foot valves in a general hydraulic damper design. In the following sections, after reviewing the mechanical design criteria, design procedure for the two proposed hybrid damper configurations will be presented.

5.3.2 Stress Analysis

Two key parameters in stress analysis of the proposed hybrid dampers are the rod diameter and the wall thickness of the outer tube (in the electromagnetic/hydraulic design). The two major load-carrying components of the system are the cylinder and the piston. The following sections describe the general method for the mechanical design of the piston and cylinder.

5.3.2.1 Sizing of Cylinder Thickness

The primary indicator in the design of a cylindrical barrel with internal pressure is the hoop stress. The maximum hoop stress produced by the hydraulic pressure p is obtained from the material tensile strength S, and the factor of safety n as:

$$\sigma_H = \frac{P_H r_{bore}}{\delta_c} = \frac{S}{n}, \tag{5-15}$$

where r_{bore} is the cylinder bore radius, and δ_c is the thickness of the cylinder. For the hydraulic damper design in continuous severe application, a safety factor 4 is proposed (Majumdar, 2001). For a regular hydraulic damper internal-pressure of no more than 2 MPa (Dixon, 1999), and a bore radius of $r_{bore} \simeq (D+s) - \delta_c$, the thickness δ_c=2 mm is required, with the selection of the stainless steel (grade 304 with yield strength of 200 MPa), maintaining a factor of safety n=4.5.

5.3.2.2 Piston Stress Analysis

The piston rod is another key component in damper design that is exposed to bending, tensile and compressive forces. The rod material is selected from high strength materials that are finished and

hardened, resisting the corrosion. If the rod's length exceeds 10 times its diameter, it is considered as a column under compression and should be designed for buckling. In this case, the piston rod diameter is related to the critical buckling load F_c from the Euler's formula

$$F_c = \frac{\pi^2 E I_m}{L_k^2} = \frac{\pi^3 E d^4}{64 L_k^2}, \tag{5-16}$$

where L_k is the free buckling length, I_m is the moment of inertia, and E is the Modulus of elasticity. The factor of safety, n, of three is considered for this case (Majumdar, 2001), and the critical piston rod's free length is obtained from

$$L_k = \pi \sqrt{\frac{E I_m}{F_c n}}. \tag{5-17}$$

On the other hand, if the piston rod is stressed as a rod (and not as a column), the rod cross-section area can be simply obtained relative to the max compressive or tensile load, F_{max}, for a completely reversed sinusoidal loading cycle in the fatigue analysis

$$d = \sqrt{\frac{4 F_{\max} n}{\pi S_e}}, \tag{5-18}$$

where S_e is the endurance limit.

Stainless steel (grade 304) is selected as the piston's material. This is selected to prevent corrosion of the piston during use. The endurance limit is calculated as S_e=175 MPa, applying the required endurance modification factors. With a compressive force of 2000 N and a factor of safety of 4, the minimum rod diameter is found to be d_{min}=7.5 mm.

5.4 Mono-tube Hybrid Damper Design

Fig. 5-6 illustrates the overall dimensions of the mono-tube electromagnetic/hydraulic damper. In a mono-tube damper, the foot valve is omitted and a free piston is run in a series with the main piston. The total number of poles in the active electromagnetic motor part and the pole pitch are obtained in Section 5.2 as 4 and 24 mm, providing the essential active force. The minimum required L_{am} is then set equal to 96 mm, as listed in Table 5-2.

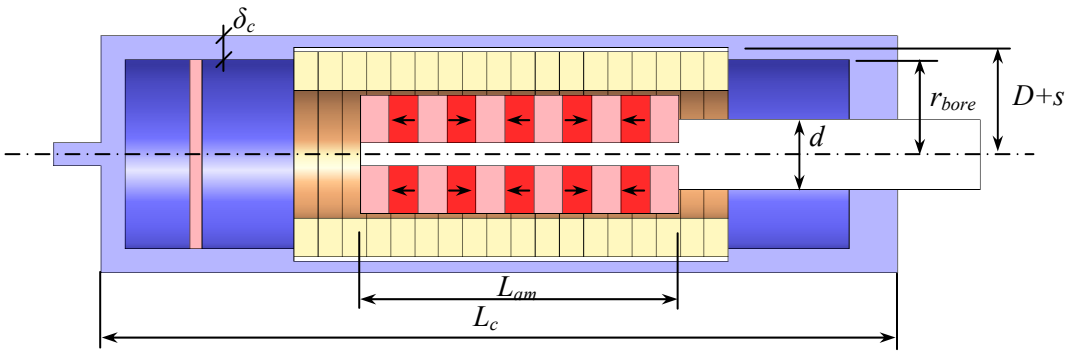

Fig. 5-6 Overall dimension of the mono-tube hybrid electromagnetic/hydraulic damper.

The main object in this section is to find the drag force on the mover (due to its movement in the viscous fluid) and its correlation with the design parameters, so that the gap effect (between the magnets and coils) is modeled as an orifice. There are different forms of parasitic drag forces involved, such as *form drag* and *skin friction* due to the passage of the mover through the viscous fluid.

Form drag arises due to the flow separation and its attendant vortices at the mover endings. It is highly influenced by the form and shape of the mover and rises with the square of speed. This effect causes the pressure loss in the order of 100 Pa across the mover, due to low mover speed range (<1.2 m/s), which is negligible compared to the required pressure drop (~100 kPa).

Skin friction (viscous loss) on the other hand, arises from the friction of the fluid with the moving object skin. For the moving object through a fluid at relatively slow speeds, the force of drag is proportional to velocity, but opposite in direction. As it will be shown, the viscous loss is the dominant drag force in the proposed hybrid damper configuration. Considering the damper configuration, as shown in Fig. 5-6, the gap between the magnets and coils behave as an orifice, causing a viscous loss across the mover.

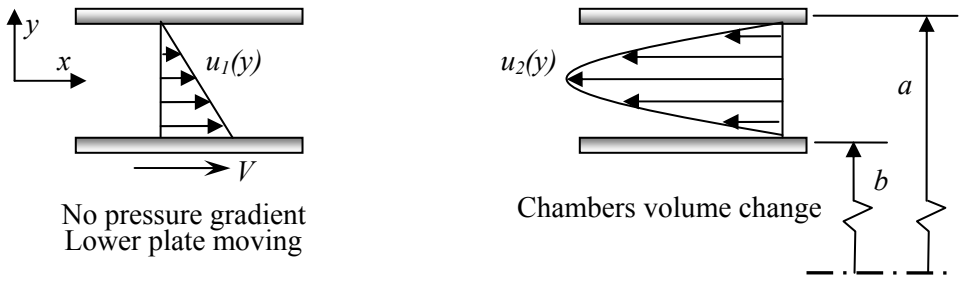

Fig. 5-7 Viscous flow in the gap (modeled as two parallel plates).

As the gap clearance is small compared to the diameter (~1%), it could be modeled as the flow between two parallel plates. Assume the mover shifts to the right (extension stage) with the velocity of $V=V_E$. Considering an incompressible viscous flow between parallel plates at a no-slip condition at the walls, the total fluid velocity is the superposition of the flow due to the lower plate movement (to the right), and the volume change in compression/extension chamber (to the left), as shown in Fig. 5-7. The average value of the fluid velocity in compression/extension stages is obtained as:

$$u_{ave} = u_{2_{ave}} - u_{1_{ave}} = \frac{(A_p - A_R)}{Ag} V - \frac{1}{2} V = K_v V \,, \tag{5-19}$$

where $A_g = 2\pi(s + l_m)s_c$ is the cross-section area of the gap. It should be mentioned that the K_v value is assumed constant and equal for both compression/extension stages (for a steady-state study). In practice, due to the gas compressibility, the K_v is smaller in the compression stage compared to the extension stage. Now, considering a fully developed flow through a concentric annulus, the pressure drop across the two compression and extension chambers are obtained as:

$$P_{PE} = P_{PC} = f \frac{L_{am}}{D_h} \rho \frac{u_{ave}^2}{2}, \tag{5-20}$$

where ρ is the fluid density. The friction factor f for a laminar flow in a concentric annulus is of the form (White, 2003)

$$f = \frac{64\xi}{\mathrm{Re}_{D_h}} \qquad \xi = \frac{(a-b)^2(a^2-b^2)}{a^4 - b^4 - (a^2-b^2)^2 / \ln(a/b)} \tag{5-21}$$

Also, the hydraulic diameter for an annulus is

$$D_h = 2(a-b)\,, \tag{5-22}$$

and its corresponding Reynolds is of the form

$$\mathrm{Re}_{D_h} = \frac{\rho u_{ave} D_h}{\mu}, \tag{5-23}$$

where μ is the fluid viscosity. Substituting the Reynolds number into (5-21), and finally f into (5-20), the pressure drops are obtained as

$$P_{PE} = P_{PC} = \left(\frac{32\mu\xi L_{am} K_v}{D_h^2} \right) V \,. \tag{5-24}$$

It is revealed from Eq. (5-24) that the pressure drop is a linear function of the velocity.

The general hydraulic formulation derived in section 5.3.1 should be updated for this case study, starting with (5-2) as

$$Q_{PC} = Q_{PE} = (K_v A_g) V \,. \tag{5-25}$$

The slight difference between (5-25) and (5-2) is due to the effect of u_1 velocity ($0.5 A_g V$). Setting Q_{FE} and Q_{FC} equal to zero, the two force equations of (5-6) and (5-7) are modified to

$$\begin{aligned} F_{PC} &= P_G A_R + \left[C_{PC} K_v A_g (A_p - A_R) \right] V_C, \\ F_{PE} &= -P_G A_R + \left[C_{PE} K_v A_g (A_p - A_R) \right] V_E. \end{aligned} \tag{5-26}$$

From (5-24) the equivalent orifice discharge coefficient for the viscous loss in the gap is obtained as

$$C_{PE} = C_{PC} = \left(\frac{32\mu\xi L_{am}}{D_h^2 A_g} \right). \tag{5-27}$$

Consequently, (5-12) and (5-14) are simplified to

$$C_E = C_C = K_v C_{PC} A_g (A_P - A_R) \,. \tag{5-28}$$

The same result is obtained by comparing (5-26) with (5-8). Combining these pressure drop equations with (5-3) and then (5-28), the final result for the damping coefficients in compression/extension are derived as a function of A_R.

$$C_E = C_C = \frac{32\mu\xi L_{am} K_v (A_P - A_R)}{D_h^2} \,, \tag{5-29}$$

It is revealed that the damping coefficient is increased when the piston rod diameter is decreased. As some parameters, such as the piston and gap areas, ξ, and D_h are already set, the damping coefficients could be adjusted to some extent, based on the mover length, rod diameter, and fluid viscosity adjustments.

The required damping coefficients in compression C_C, and extension C_E are obtained based on the average passive damping coefficient (from Table 2-4) equal to ~1400 Ns/m. The piston and gap areas are obtained from the electromagnetic active part design equal to 3.84e-3 and 1.1e-3 m^2, respectively. Then, setting the mover length equal to 96 mm (from Table 5-2), the rod diameter ($d_{\min} < d < 2(s + l_m + s_c)$) and the fluid viscosity are selected to achieve the desired damping coefficient. Minimum rod diameter is restricted to the d_{min}, calculated by stress analysis in (5-18). The oil viscosity is reduced with temperature and should be selected based on the average working temperature. The proposed specifications for the electromagnetic/hydraulic damper are listed in Table 5-3.

Table 5-3 Specification of the first proposed configuration for the hybrid damper.

Quantity	Value (Unit)
Fluid viscosity μ	20 mPa.s (@60^{oC} for SAE20)
Fluid density ρ	800 kg/m^3
Mover length L_{am}	96 mm
Rod diameter d	55 mm
Initial gas pressure	1300 kPa
Outer cylinder thickness	2 mm
Overall length L_c	300 mm
External diameter	94 mm
Overall weight	3.4+1.8=5.2 kg

With the final design specifications, listed in Table 5-3, the damping coefficients C_C and C_E are obtained from (5-29) equal to 1700 Ns/m. Although similar compression and extension damping coefficients are achieved based on the derived equations, the damping coefficient in the compression mode will be slightly reduced based on the reservoir gas compressibility, especially in the case of a sudden stroke. The static force of F_s=100 N is also exerted on the piston due to the initial gas pressure in (5-26), adding to the system stiffness.

The maximum Reynolds number in extension and compression due to the maximum velocity of 1.2 m/s is obtained from (5-23) equal to 500, which is below the critical transition value of 2300 for the laminar regime. Therefore, the assumption of laminar flow has been a valid assumption. In addition,

with the rod material selected as stainless steel 304 and the rod diameter of 55 mm, the free length of the rod is much smaller than the critical free buckling length of 11 m, obtained from (5-17).

5.5 Eddy Current Hybrid Damper Design

As described in Chapter 3, the circulating eddies of current in a conductor that is exposed to a varying magnetic field can provide a strong damping/braking effect. This effect initiates the idea of using eddy current damping as the passive damping component of the second hybrid damper design. The conceived configuration for an electromagnetic/eddy hybrid damper utilizes an outer conductor tube as a source of eddy currents, and an outer array of axially-magnetized, ring-shaped magnets, separated by iron pole pieces connected to the mover. The relative movement of the magnets and the conductor causes the conductor to undergo motional eddy currents. They create electromagnets with magnetic fields that oppose the change in an external magnetic field, causing a repulsive damping force proportional to the relative velocity of the field and conductor.

Fig. 5-8 shows the detail configuration of the electromagnetic/eddy hybrid damper. The goal is to find the dimension and material properties of the added outer conductor tube as well as PMs to achieve the desired passive damping coefficient ~1400 Ns/m.

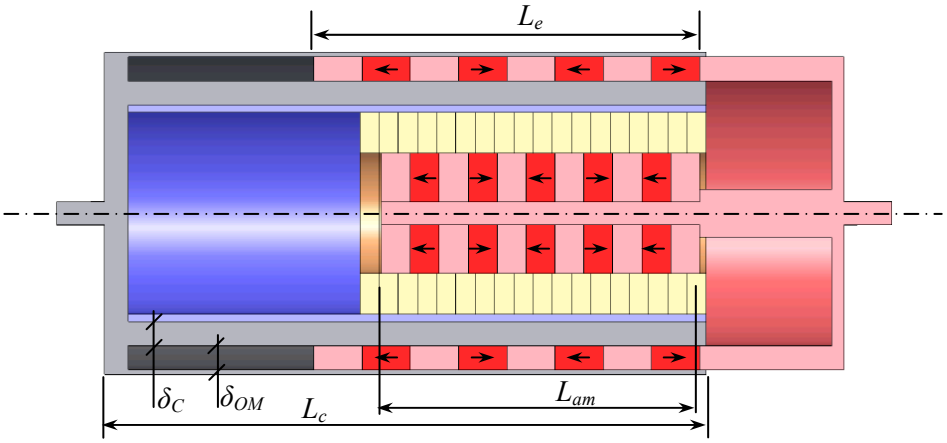

Fig. 5-8 Overall Dimension of the electromagnetic/eddy hybrid damper.

According to the Lorentz force law, the relative movement of the magnets and the conductor causes the eddy currents to induce in the conductor, which consequently produces a magnetic flux that opposes the external magnetic flux density, resulting in a damping force per each pole piece.

$$C_{eddy} = \int_{\Gamma} \sigma B_r^2 d\Gamma \,, \tag{5-30}$$

where Γ, σ, and B_r are the conductor's volume, conductivity, and the radial magnetic flux density, respectively.

There are two sources of eddy current generation: the outer conductor tube and the stator iron core. The polarity of the outer magnets array is chosen in such a way that the radial magnetic flux from the inner magnets add to that of the outer magnets in the gap between two magnet tubes. So, as the first assumption, the outer magnets number of poles, pole pitch τ and lengths τ_m are set equal to that of the inner magnets. Aluminum is selected as the initial choice for the conductor tube's material due to its light weight and high conductivity. The conductor's material selection is a trade-off between the achievable damping coefficient and the added weight to the damper. However, the ratio of the material conductivity to density is a good selecting factor for the initial material selection.

The damping coefficient generated by eddy currents can be calculated from (5-30), while the radial magnetic flux density is calculated and integrated over the conductor volume, using FE software (Comsol 3.4). Utilizing FE analysis for magnetic flux calculations causes the iron permeability, leakage flux, and ending effects to be considered in the estimation. Fig. 5-9 illustrates the magnetic flux density streamlines of a 2D axisymmetric model of the hybrid damper in Comsol 3.4. The FE simulation demonstrates a maximum of 65 Ns/m (9%) difference with analytical calculations in damping coefficient estimation.

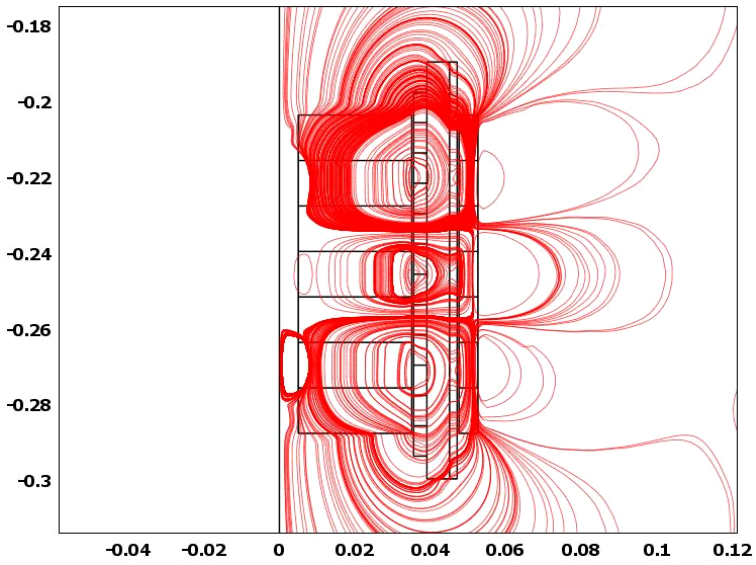

Fig. 5-9 Magnetic flux density streamlines of a 2D simulation of the second hybrid damper.

The damping coefficient and the weight added to the hybrid damper due to the eddy current effect for different conductor and PM thicknesses are listed in Table 3-5. Damping coefficients are listed as the sum of the conductor and stator core iron portions.

Table 5-4 Damping coefficient and weight added to the damper due to the eddy current effect for different conductor and PM thicknesses.

	δ_C=0 mm	δ_C=2 mm	δ_C=5 mm	δ_C=7 mm	δ_C=10 mm
δ_{OM}=5 mm	443 Ns/m (0.7 kg)	215+330 Ns/m (0.87 kg)	244+267 Ns/m (1.2 kg)	229+244 Ns/m (1.4 kg)	205+223 Ns/m (1.77 kg)
δ_{OM}=7 mm	613 Ns/m (1 kg)	379+404 Ns/m (1.2 kg)	409+301 Ns/m (1.53 kg)	378+267 Ns/m (1.76 kg)	334+237 Ns/m (2.12 kg)
δ_{OM}=10 mm	935 Ns/m (1.46 kg)	670+520 Ns/m (1.7 kg)	673+350 Ns/m (2.04 kg)	611+300 Ns/m (2.3 kg)	532+256 Ns/m (2.7 kg)
δ_{OM}=12 mm	1193 Ns/m (1.8 kg)	890+600 Ns/m (2.03 kg)	852+379 Ns/m (2.4 kg)	765+318 Ns/m (2.66 kg)	660+267 Ns/m (3.07 kg)

In order to obtain optimum conductor and outer magnets thicknesses, the generated damping coefficient for different magnet thicknesses is plotted vs. the conductor thickness in Fig. 5-10. It is revealed that the maximum damping coefficient is obtained at conductor thickness δ_C equal to 2 mm, regardless of he outer magnets' thickness δ_{OM}.

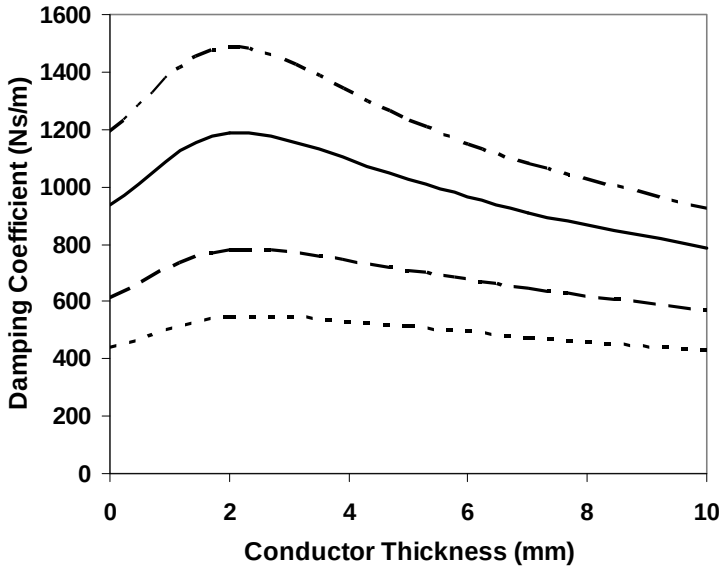

Fig. 5-10 Damping Coefficient vs. aluminum conductor thickness for different outer magnets thicknesses. —·—: $\delta_{OM} = 12mm$, ——: $\delta_{OM} = 10mm$, — —: $\delta_{OM} = 7mm$, ▪▪▪: $\delta_{OM} = 5mm$.

As the added weight due to the eddy current passive subsystem is of high importance in the design procedure, the ratio of the damping coefficient vs. the added weight to the system is also plotted in Fig. 5-11, confirming similar optimum thickness for the conductor.

As illustrated in Fig. 5-11, the damping coefficient density slightly increases with the outer magnets' thickness. Although the outer magnets' thickness should be selected based on the required damping coefficient, its optimum value (resulting in a higher damping coefficient density) is obtained ~15 mm (for aluminum) as shown in Fig. 5-12. Another important conclusion from this figure is that the conductor material effect is influenced by the geometry of outer magnets. It is revealed that the optimum magnet thickness depends on the selected conductor material. For instance, comparing the two materials of aluminum and copper, both with high conductivity/density ratio, it is shown that with a magnet thickness δ_{OM} higher than ~10mm, copper is more appealing due to its higher generation of damping force density.

Based on the required passive damping coefficient for the hybrid damper design (~1400 Ns/m), the two potential conductor choices are mentioned in Table 5-5. Consequently, the copper conductor with outer magnet thickness δ_{OM} equal to 10 mm is selected, improving the damping coefficient and the damping coefficient/weight density 5% and 2%, respectively.

Table 5-5 Two option for the conductor material and size.

Material	Outer Magnets' Thickness	Damping coefficient	Weight
Aluminum	12	1490	2.03
Copper	10	1570	2.08

With the final designed conductor and outer magnets, a 1570 Ns/m passive damping coefficient is provided at the cost of adding 2.1 kg of additional weight. As a result, the final dimensions of the hybrid electromagnetic/hydraulic damper is obtained and listed in Table 5-6.

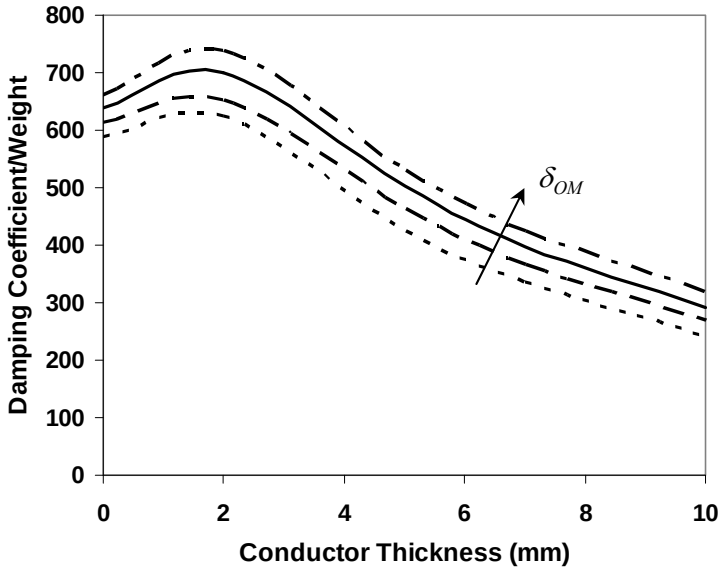

Fig. 5-11 Damping coefficient/weight vs. aluminum conductor thickness for different outer magnet thicknesses. —▪—: $\delta_{OM} = 12mm$, ——: $\delta_{OM} = 10mm$, — —: $\delta_{OM} = 7mm$, ▪▪▪: $\delta_{OM} = 5mm$.

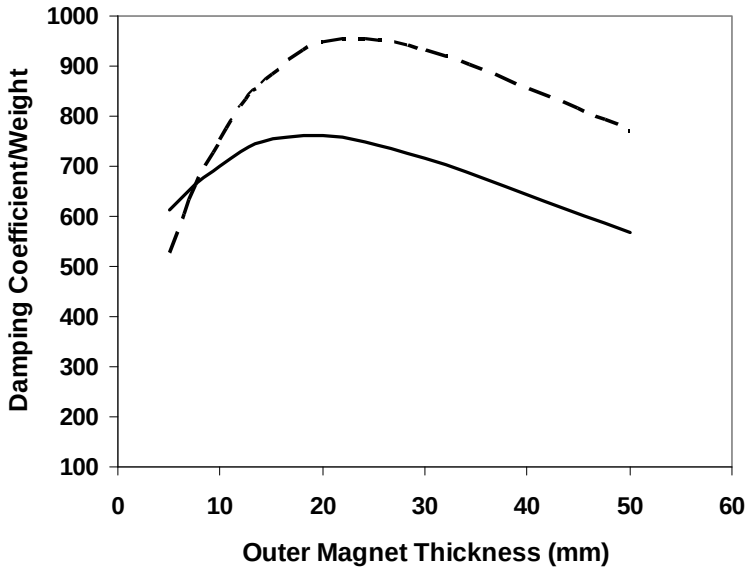

Fig. 5-12 Damping coefficient/weight vs. outer magnet thickness ($\delta_c = 2\,mm$) for — —: Copper and ——: aluminum.

Table 5-6 Final dimensions of the hybrid electromagnetic/hybrid damper.

Outer magnets array	
Number of poles p	4
Pole pitch τ	24 mm
Magnet thickness τ_m	12 mm
Magnet outside diameter	114 mm
Thickness δ_{OM}	10 mm
Total length L_e	96 mm
Outer magnets' weight	1.52 kg
Magnets' material	Nd-Fe-B, B_r=1.17 T
Conductor	
Conductor's material	Copper
Conductivity	5.9e7 S/m
Density	8.9e3 kg/m^3
Thickness δ_C	2 mm
Conductor weight	0.56 kg

It should be mentioned that adding outer PMs increases the magnetic flux density passing through the stator coils, enhancing the performance of the active subsystem. Comparing the hybrid damper with and without outer magnets shows a 0.004 T (2%) increase in maximum flux density in the stator coils, which is not significant, and can be neglected.

The final design specifications of the electromagnetic/eddy hybrid damper are listed in Table 5-7. The obtained specifications will be compared to that of the other electromagnetic/hydraulic damper in the next section.

Table 5-7 Overall Specifications of the proposed electromagnetic/eddy hybrid damper.

Quantity	Value
Passive damping coefficient	1570 Ns/m
External diameter	115 mm
Total length	260 mm
Total weight	3.4+2.1=5.5 kg

5.6 Final Comparison of Hybrid Dampers and Conclusions

After the active Electromagnetic Damper (ED) is proposed and designed in Chapter 4, the new idea of adding passive damping to the ED is presented and developed in this chapter. It is explained how the hydraulic/eddy current forces can provide a minimum required passive damping to ensure a smaller, lighter, and more reliable active damper with less power consumption. The feasibility of the hybrid damper concept is studied, starting with selecting appropriate hybrid damper topologies, followed by initial sizing of the electromagnetic subsystem. Two different topologies are proposed and designed based on the derived design requirements in Chapter 2. The first proposed hybrid damper configuration utilizes hydraulic damping effect, while the second one uses the eddy current damping phenomenon.

Both hybrid damper designs shared similar active component, which is designed in Section 5.2.1, providing the minimum active force required for hybrid dampers. It is shown that as the required active force is reduced from 1300 N in fully active case to 350 N in the hybrid system, the power consumption is reduced 74% in the hybrid damper compared to that of active ED. This corresponds to

a 71% reduction in the weight of the active unit. The final design specifications for those two hybrid dampers are presented and compared to that of the ED damper in Table 5-8.

For the first hybrid damper design, in which the hydraulic forces are utilized to provide the required passive damping, a general hydraulic damper design method is presented and then narrowed down to the specific case of the electromagnetic/hydraulic damper design. It is demonstrated that a significant passive damping of ~1700 Ns/m can be provided, by the addition of the viscous fluid to the active damper, which guarantees a fail-safe damper in case of electronic failure. In addition, the hydraulic system has the benefit of adding a cooling system to the damper. Among different dampers listed in Table 5-8, it has the lowest weight. The damper also exhibits a similar damping behavior in extension/compression stages, while the damping coefficient in compression is slightly lower due to the reservoir gas compressibility. Comparing this damper with the active ED, it is revealed that the weight and power consumption of the designed hybrid damper is reduced by 56% and 74%, respectively.

Table 5-8 Final comparison of the two hybrid damper configurations and the active ED.

Specification	Hybrid (Hydraulic)	Hybrid (Eddy current)	Active ED	Design criteria
Total weight	5.2 kg	5.5 kg	11.8 kg	<7 kg
Total length	300 mm	260 mm	350 mm	<600 mm
External diameter	94 mm	115 mm	120 mm	<150 mm
Passive damping Coeff.	1700 Ns/m	1570 Ns/m	550 Ns/m	~1400 Ns/m
Peak active force	320 N	320 N	1200 N	1300 & 350 N
Required power (4 unit)	380 W	380 W	1480 W	

For the second electromagnetic/eddy hybrid damper, the dimensions of the added conductor and magnets are selected to minimize the weight added to the system while maintaining the required passive damping. It is shown that a 1570 Ns/m passive damping is achieved with the introduction of the eddy current damping effect to the hybrid system at the cost of adding 2.1 kg of additional weight. Comparing this design with the former proposed hybrid damper, its weight is increased by 5% and its overall length is reduced 13%, while they have a similar damping performance.

An overall comparison of the active electromagnetic damper with the proposed hybrid dampers in this section reveals that the latter has 74% less power consumption and ~55% less weight, while maintaining the active damping performance advantages.

Chapter 6

Summary of Results and Future Work

The contents of this thesis are driven by the introduction and development of novel hybrid dampers for automotive active suspension applications. Spanning mechanical/electromagnetic design, finite element simulation, fabrication and testing, this thesis began with an introduction and literature survey on the existing automobile suspension systems as well as shock absorbers technologies, and ended with a fairly successful hybrid damper design for active suspension systems. The content of this thesis could be divided into three major categories: 1) Introduction of the eddy current damping effect for the automotive suspension application, 2) Design and development of an active electromagnetic damper, and 3) Conceptual design and modeling of the new generation of hybrid dampers.

After a brief introduction on automotive suspension systems in the first chapter, the damper design requirements and design criteria are stated in the second chapter. This includes the assessment of the high-end semi-active, off-the-shelf dampers through conducting experimental analysis. Then, the active suspension systems are studied, using a tubular linear PM motor as an actuator. An experimental comparison in terms of control effort and damper performance has been conducted between the active and semi-active control strategies, revealing that to achieve a similar performance at the resonant frequency of the system, 35% lower damping force is required in case of using active skyhook strategy compared to the semi-active one. Finally, in the second chapter, the damping requirements and dimension restrictions are established for the final hybrid damper design.

For the very first time, in this thesis, the eddy current damping concept is introduced for the automotive suspension applications. The idea was to develop a passive damping component for the final hybrid design. However, the Eddy Current Damper (ECD) as a stand-alone passive damping unit is characterized and its performance is studied. A prototype ECD is fabricated and experiments are conducted to investigate the frequency/time response behavior of the damper in a 1DOF vibration isolation system. It is shown both analytically and experimentally that the damping characteristics of

the system can be improved more than eight-fold by adding eddy current damping to the system. In addition, the demagnetization effect and the magnets stability due to different factors, such as temperature and time, are studied to ensure the ECD fail-safety and reliability. Finally, a full-size ECD is designed based on the derived model, and its performance is compared with the performances of the commercial passive dampers. It is revealed that the ECD is three times heavier and costs more than twice as much as commercial passive dampers. However, it is still practical in the case of lightweight vehicles.

The presence of an active actuator component in the final hybrid damper necessitates the development of an active electromagnetic actuator. A customizable linear motor is utilized as the base idea of the active Electromagnetic Damper (ED). A general methodology for the active electromagnetic damper design is introduced, and an analytical approach, based on the magnetic circuit principles, is employed to address the achievable damping force with non-dimensional geometry design parameters. Finally, an active full-scale ED for an automotive suspension application is designed, and the maximum achievable damping coefficient and force in the semi-active and active-modes are estimated. The final full-scale ED, with its 11.8 kg weight and 350 mm overall length, is capable of providing 1200 N of thrust force (requiring 370 W).

Upon the design of an active ED, a new idea of adding passive damping to the ED is presented and developed. Coupling the performance of the active suspension system with the reliability of passive ones is manifest by the introduction of the new hybrid damper generation. This study indicates that the coupling of active/passive systems benefits the power consumption issue in active systems, while saving cost and weight. Two potential hybrid damper designs corresponding to two passive damping sources are proposed. Hydraulic and eddy current damping forces are employed for the first and second hybrid damper designs, respectively. A general hydraulic damper design frame is developed and the stress analysis is considered as the starting point for the electromagnetic/hydraulic damper design. The designed damper is analyzed under the steady-state conditions to determine the correlation between the damper performance and design parameters. It is demonstrated that a passive damping of ~1700 Ns/m can be achieved by the addition of the viscous fluid to the active damper, which guarantees a fail-safe damper in case of power failure. For the second hybrid damper design, the geometry of the proposed damper topology is optimized to achieve the required passive damping from the minimum added weight to the system. It is demonstrated that more than 1500 Ns/m damping coefficient is obtainable by utilizing the eddy current damping effect and the addition of the 2.1 kg of

weight to the system. Comparing the fully-active ED with the newly proposed hybrid damper designs implies that weight and power consumption of the ED could be reduced more than 50% and 70%, respectively, by converting it into a hybrid damper.

Overall, this research project advances the state of knowledge in electromagnetic suspension systems, contributing to related areas such as the eddy current damping phenomenon and its application in automotive suspension systems, linear motor design optimization, and the introduction of a new concept of hybrid damper design with the two proposed hybrid damper configurations. So far, this research has resulted in the following academic publications:

J1- Babak Ebrahimi, Mir Behrad Khamesee, Farid Golnaraghi, A novel eddy current damper: theory and experiment, *Journal of Physics D: Applied Physics*, 42 (7), 2009

J2- Babak Ebrahimi, Mir Behrad Khamesee, Farid Golnaraghi, Eddy-Current applicability in automobile suspension: scaled-down design and evaluation, *Smart Materials and Structures*, 18(1), 2009, 12p

J3- Babak Ebrahimi, Mir Behrad Khamesee, Farid Golnaraghi, Permanent magnet configuration in design of an eddy current damper, *Journal of Microsystem Technologies,* DOI: 10.1007/s00542-008-0731-z, 2008

J4- Babak Ebrahimi, Mir Behrad Khamesee, Farid Golnaraghi, Design and modelling of a magnetic shock absorber based on eddy current damping effect, *Journal of Sound and Vibration*, 315 (4), 2008 pp. 875-889

J5- Babak Ebrahimi, Hamidreza Bolandhemmat, Farid Golnaraghi, Mir Behrad Khamesee, A hybrid electromagnetic shock absorber for active vehicle suspension systems, *Vehicle System Dynamics* (Submitted)

C6- Babak Ebrahimi, Mir Behrad Khamesee, Farid Golnaraghi, Design of an electromagnetic shock absorber, *Proceedings of ASME International Mechanical Engineering Congress and Exposition, IMECE 2007*, Seattle, USA, November 2007, pp. 2009-2014.

C7- Babak Ebrahimi, Mir Behrad Khamesee, Farid Golnaraghi, Design and modelling of a novel electromagnetic damper, *Proceedings of ISPS 2008, 18th ASME Annual Conference on Information Storage and Processing Systems*, Santa Clara, California, USA, June 2008 (Best Track Paper Award)

C8- Babak Ebrahimi, Mir Behrad Khamesee, Farid Golnaraghi, Development of a novel eddy current damper, *Proceedings of ISPS 2008, 18th ASME Annual Conference on Information Storage and Processing Systems*, Santa Clara, California, USA, June 2008

C9- Babak Ebrahimi, Mir Behrad Khamesee, Farid Golnaraghi, Feasibility study of an electromagnetic shock absorber with position sensing capability, *The 34th Annual Conference of the IEEE Industrial Electronics Society, IECON'08*, Orlando, Florida, USA, November 2008, pp. 2988-2991.

C10- Babak Ebrahimi, Mir Behrad Khamesee, Farid Golnaraghi, Design of a hybrid electromagnetic/hydraulic damper for automotive suspension systems, *IEEE International Conference on Mechatronics and Automation, ICMA '09*, Changchun, Jilin, China, August 2009

6.1 Future work

Based on the completed work on active electromagnetic dampers, the following research is recommended for future study.

- In practice it was seen that the use of reservoir gas chamber in the first hybrid damper design causes the asymmetric behavior in compression/extension, which was not discussed in depth in this thesis. It is suggested that a fluid analysis is performed to model this effect so the characteristics of the reservoir chamber will be designed in a such way that the damper potentially exhibits the desired asymmetric damping behavior in compression/extension stages.
- The passive damping performance of the electromagnetic/hybrid damper design is highly influenced by the fluid viscosity and so with the operating temperature. At the same time, the viscous fluid acts as a cooling system for the stator coils. As a part of future work, the effect of the moving fluid in the steady-state working temperature of the system could be analyzed. Although the operating temperature is influenced by the operating and road conditions as well as the environmental temperature, the hydraulic hybrid damper design could be modified based on a more accurate operating temperature.
- The design and modeling of other hybrid damper configurations is another key future work suggestion. For example, the first hydraulic hybrid damper design could be potentially modified to a twin-tube electromagnetic/hybrid damper, where the reservoir is concentrically placed around

the main cylinder. This causes the damper to operate with lower initial reservoir gas pressure, while the damper is less susceptible to damage caused by impact.

- Another recommendation is to develop an industrial version of the developed hybrid damper designs. The electromagnetic/hydraulic hybrid damper concept could be implemented as a modular component to be added to the off-the-shelf passive dampers.
- Development of the controller and driver for the final hybrid damper designs is another important aspect of the future work. A force-mode servo controller, including a power module for driving the motor, should be designed.
- As briefly mentioned in this thesis, the damper's response-time is an important factor in practical implementation of the damper and its controller module in a vehicle suspension system. The response time behavior should be investigated, considering different parameters that can affect the response time, such as: mover velocity, stroke, and the operating current. The associated control strategy could then be potentially modified to accommodate the effect of the response time.
- Real-time testing of the developed damper designs and the control strategies on an actual vehicle suspension system and testing on the standard test tracks are recommended.
- The redesign of the hydraulic part of the first hybrid damper configuration should also be considered. A more complex, transient fluid analysis could likewise be considered to investigate other involving factors such as impact and cavitation effects.

Finally, future work should include a revisit of the hybrid damper design, with the goal of minimizing the weight and size, and enhancing the damping performance.

The presented study is part of a growing body of research in this area. The major research groups with similar subject matter are: Suda *et al.* (Japan), Martins *et al.* (Portugal), Gupta *et al.* (USA), Alen *et al.* (USA), and Graves *et al*. (Australia) as well as a number of pioneer companies such as Bose Corporation (USA) and Michelin (USA). It is hoped that the presented research in this thesis ultimately lead to the realization of a superior damper technology.

Appendix A

Review of Electromagnetism

A.1 Maxwell's Equations

Electromagnetic fields are governed by Maxwell's equations, where $\boldsymbol{H}$ (magnetic field intensity (A/m)), $\boldsymbol{B}$ (magnetic flux density (T)), $\boldsymbol{E}$ (Electric field intensity (V/m)), and $\boldsymbol{D}$ (Electric flux density (C/m3)) are the fields. $\boldsymbol{J}(A/m^2)$ and $\rho(C/m^3)$ are the source terms.

$$\nabla \times \boldsymbol{H} = \boldsymbol{J} + \frac{\partial \boldsymbol{D}}{\partial t}, \tag{A-1}$$

$$\nabla \cdot \boldsymbol{B} = 0, \tag{A-2}$$

$$\nabla \times \boldsymbol{E} = -\frac{\partial \boldsymbol{B}}{\partial t}, \tag{A-3}$$

$$\nabla \cdot \boldsymbol{D} = \rho. \tag{A-4}$$

This system of equations, which are not all independent, represents a system of 12 unknown field components. For a complete theory of field equations, the additional constitutive equations must be added to Maxwell's equations as follows:

$$\boldsymbol{B} = \mu_0(\boldsymbol{H} + \boldsymbol{M}), \tag{A-5}$$

$$\boldsymbol{D} = \varepsilon_0 \boldsymbol{E} + \boldsymbol{P}, \tag{A-6}$$

and

$$\boldsymbol{J} = \sigma \boldsymbol{E}, \tag{A-7}$$

where $\boldsymbol{M}$ (A/m) is the magnetization, $\boldsymbol{P}$ (C/m^2) is the polarization, $\mu_0 = 4\pi \times 10^7$ (Tm/A), $\varepsilon_0 = 8.854 \times 10^{-12}$ (F/m), and σ (A/Vm) are the permeability, permittivity, and conductivity, respectively.

Maxwell's equations can be expressed in the integral form by taking the surface integral of the curl Eqs. (A-1) and (A-3), then, applying Stokes' theorem to the left-hand side. Also, the divergence Eqs. (A-2) and (A-4) are integrated, and then the divergence theorem is applied to the left-hand side.

$$\oint_C \boldsymbol{H} \cdot d\boldsymbol{l} = \int_S (\boldsymbol{J} + \frac{\partial \boldsymbol{D}}{\partial t}) \cdot d\boldsymbol{s}\,, \tag{A-8}$$

$$\oint_C \boldsymbol{E} \cdot d\boldsymbol{l} = -\int_S (\frac{\partial \boldsymbol{B}}{\partial t}) \cdot d\boldsymbol{s}\,, \tag{A-9}$$

$$\oint_S \boldsymbol{B} \cdot d\boldsymbol{s} = 0\,, \tag{A-10}$$

$$\oint_S \boldsymbol{D} \cdot d\boldsymbol{s} = \int_\Gamma \rho d\Gamma\,. \tag{A-11}$$

(A-8) is the general form of Ampere's law, (A-9) is Faraday's law, which states that the ***E***-field is generated by a time varying magnetic field, and (A-10) states that the outward flux over a closed surface is zero, *i.e*., there are no magnetic monopoles (isolated sinks or sources). The last equation is called Gauss's law, and it states that the total outward electric flux over a closed surface equals the free charges enclosed by the surface.

A.2 Potentials

A vector potential and a scalar potential are vector fields, whose curl and negative gradient are a given vector field, respectively. Typically, it is more convenient to obtain the fields by using potential functions. Vector (***A***) and scalar potentials (φ) are used to convert Maxwell's four coupled, first-order equations into two uncoupled second-order equations. The vector potential ***A*** is defined by (A-2) as follows:

$$\nabla \cdot \boldsymbol{B} = 0 \Rightarrow \boldsymbol{B} = \nabla \times \boldsymbol{A}\,. \tag{A-12}$$

The scalar potential φ is defined by (A-3) as

$$\nabla \times \left(\boldsymbol{E} + \frac{\partial \boldsymbol{A}}{\partial t} \right) = 0 \Rightarrow \boldsymbol{E} + \frac{\partial \boldsymbol{A}}{\partial t} = -\nabla \varphi\,. \tag{A-13}$$

By substituting (A-12) and (A-13) into the remaining two Maxwell equations,

$$\nabla^2 \boldsymbol{A} - \nabla(\nabla \cdot \boldsymbol{A} + \mu\varepsilon \frac{\partial \varphi}{\partial t}) - \mu\varepsilon \frac{\partial^2 \boldsymbol{A}}{\partial t^2} = -\mu \boldsymbol{J},$$
$$\nabla^2 \varphi + \frac{\partial(\nabla \cdot \boldsymbol{A})}{\partial t} = -\frac{\rho}{\varepsilon}. \tag{A-14}$$

By imposing the Lorenz gauge condition ($\nabla \cdot \boldsymbol{A} = -\mu\varepsilon \frac{\partial \varphi}{\partial t}$), the two final second-order equations are

$$\nabla^2 \boldsymbol{A} - \mu\varepsilon \frac{\partial^2 \boldsymbol{A}}{\partial t^2} = -\mu \boldsymbol{J},$$
$$\nabla^2 \varphi - \mu\varepsilon \frac{\partial^2 \varphi}{\partial t^2} = -\frac{\rho}{\varepsilon}. \tag{A-15}$$

Maxwell's equations span the entire electromagnetic applications, which are categorized as high frequency, quasi-static, and static. The quasi-static theory governs a wide range of applications, including electromechanical devices and eddy current phenomena.

In the quasi-static approximation, the displacement current term $\partial \boldsymbol{D} / \partial t$ is ignored in (A-1). The potential equations are reduced to Poisson's equations,

$$\nabla^2 \boldsymbol{A} = -\mu \boldsymbol{J},$$
$$\nabla^2 \varphi = -\frac{\rho}{\varepsilon}. \tag{A-16}$$

In free space, the solution to (A-16) is expressed by using Green's function $G(\boldsymbol{x}, \boldsymbol{x}') = -(1/4\pi)(1/|\boldsymbol{x} - \boldsymbol{x}'|)$ for operator ∇^2:

$$\boldsymbol{A}(\boldsymbol{x}, t) = \frac{\mu_0}{4\pi} \int_\Gamma \frac{\boldsymbol{J}(\boldsymbol{x}', t)}{|\boldsymbol{x} - \boldsymbol{x}'|} d\Gamma' \tag{A-17}$$

and

$$\varphi(\boldsymbol{x}, t) = \frac{1}{4\pi\varepsilon_0} \int_\Gamma \frac{\rho(\boldsymbol{x}', t)}{|\boldsymbol{x} - \boldsymbol{x}'|} d\Gamma', \tag{A-18}$$

where x is the observation point, and $\boldsymbol{x}'$ is the source point.

The static-field theory is also applied to a variety of applications such as permanent magnet structures, and direct current devices. In the static-field theory, both time-dependent terms are ignored ($\partial \boldsymbol{D}/\partial t = \partial \boldsymbol{B}/\partial t = 0$). The solutions of the potential equations are similar to those in the quasi-static case, unless the scalar and vector potentials are not time dependent.

A.3 Magnetic Field Analysis

Once $\boldsymbol{A}$ is determined by calculating (A-17), the magnetic flux density $\boldsymbol{B}$ can be computed by using $\boldsymbol{B} = \nabla \times \boldsymbol{A}$, and

$$\boldsymbol{B}(\boldsymbol{x},t) = \frac{\mu}{4\pi}\int \frac{\boldsymbol{J}(\boldsymbol{x}',t)\times(\boldsymbol{x}-\boldsymbol{x}')}{\left|\boldsymbol{x}-\boldsymbol{x}'\right|^3} d\Gamma' . \tag{A-19}$$

For a thin filament (wire), $\boldsymbol{J}d\Gamma' \to I d\boldsymbol{l}'$, and (A-19) converted to the Biot-Savart law

$$\boldsymbol{B}(\boldsymbol{x},t) = \frac{\mu I}{4\pi}\oint_C \frac{d\boldsymbol{l}'\times(\boldsymbol{x}-\boldsymbol{x}')}{\left|\boldsymbol{x}-\boldsymbol{x}'\right|^3} . \tag{A-20}$$

For surface currents, $\boldsymbol{J}d\Gamma' \to \boldsymbol{j}ds'$, (A-19) becomes

$$\boldsymbol{B}(\boldsymbol{x},t) = \frac{\mu}{4\pi}\int \frac{\boldsymbol{j}(\boldsymbol{x}',t)\times(\boldsymbol{x}-\boldsymbol{x}')}{\left|\boldsymbol{x}-\boldsymbol{x}'\right|^3} ds' , \tag{A-21}$$

where $\boldsymbol{j}$ (A/m) is the surface current density.

There are a number of approaches for calculating the magnetic field of a permanent magnet. The simplest approach is the dipole moment model that is appropriate for the field calculation at long distances from the magnet, compared with the magnet diameter. The charge method and the current method model the magnet with a distribution of the charge and current, respectively.

A.4 Magnetic Dipole Moment Method

In this method, the permanent magnet is modeled by a single current carrying loop, as shown in Fig. A- 1.

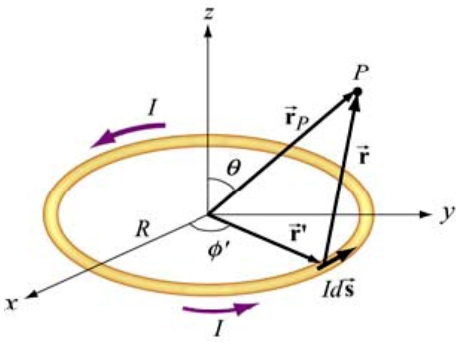

Fig. A- 1 A single current carrying loop.

By applying the Biot-Savart law (A-20) by $d\boldsymbol{l}' = Rd\phi'\hat{\phi}$, $\boldsymbol{x} - \boldsymbol{x}' = z\hat{\boldsymbol{z}} - R\hat{\boldsymbol{r}}$ and $|\boldsymbol{x} - \boldsymbol{x}'| = \sqrt{R^2 + z^2}$, the magnetic flux along the axis of the current loop results in

$$\boldsymbol{B}(z) = \frac{\mu_0 IR^2}{4\pi}\int_0^{2\pi} \frac{d\phi'}{(R^2 + z^2)^{3/2}}\hat{\boldsymbol{z}}, \tag{A-22}$$

which is reduced to

$$\boldsymbol{B}(z) = \frac{\mu_0 \boldsymbol{m}}{2\pi(R^2 + z^2)^{3/2}}, \tag{A-23}$$

where $\boldsymbol{m} = I\pi R^2\hat{\boldsymbol{z}}$ is the magnetic dipole moment of the loop. As it will be seen in the next section, the equivalent dipole moment for a magnet is $\boldsymbol{m} = Ml\pi R^2\hat{\boldsymbol{z}}$, when a constant magnetization in the *z* direction is assumed. *R* and *l* represent the radius and length of the magnet.

A.5 The Current Model (Magnetic Flux Calculation)

In the current model, the magnet is expressed as the distribution of the equivalent current, which is used as a source term in the magnetostatic field equations. By substituting (A-12) into (A-1), and imposing the Coulomb Gauge ($\nabla.\boldsymbol{A} = 0$),

$$\nabla^2\boldsymbol{A} = -\mu_0(\boldsymbol{J} + \nabla\times\boldsymbol{M}). \tag{A-24}$$

(A-24) causes the definition of the magnetic volume current density $\boldsymbol{J}_m \equiv \nabla \times \boldsymbol{M}$. If the magnetization $\boldsymbol{M}$ is restricted to a volume Γ, and falls to zero outside of Γ, (A-19) is reduced to

$$\boldsymbol{B}(\boldsymbol{x}) = \frac{\mu}{4\pi}\int \frac{\boldsymbol{J}_m(\boldsymbol{x}')\times(\boldsymbol{x}-\boldsymbol{x}')}{|\boldsymbol{x}-\boldsymbol{x}'|^3} d\Gamma' + \frac{\mu}{4\pi}\int \frac{\boldsymbol{j}_m(\boldsymbol{x}')\times(\boldsymbol{x}-\boldsymbol{x}')}{|\boldsymbol{x}-\boldsymbol{x}'|^3} ds', \tag{A-25}$$

where $\boldsymbol{J}_m$ and $\boldsymbol{j}_m$ are equivalent volume and surface current densities and defined by:

$$\begin{aligned} \boldsymbol{J}_m &= \nabla \times \boldsymbol{M} \ \ (A/m^2)\ \textit{Volume current density}, \\ \boldsymbol{j}_m &= \boldsymbol{M} \times \hat{\boldsymbol{n}} \ \ (A/m)\ \ \textit{Surface current density}, \end{aligned} \tag{A-26}$$

where $\hat{\boldsymbol{n}}$ is the outward unit normal to the surface.

By assuming that a cylindrical magnet is polarized along its *z*-axis with a uniform magnetization *i.e.* $\boldsymbol{M} = M_s \hat{\boldsymbol{z}}$, as shown in Fig. A- 2, the volume and surface current densities are

$$\begin{aligned} \mathbf{J}_m &= 0, \\ \mathbf{j}_m &= M\hat{\boldsymbol{\varphi}}. \end{aligned} \tag{A-27}$$

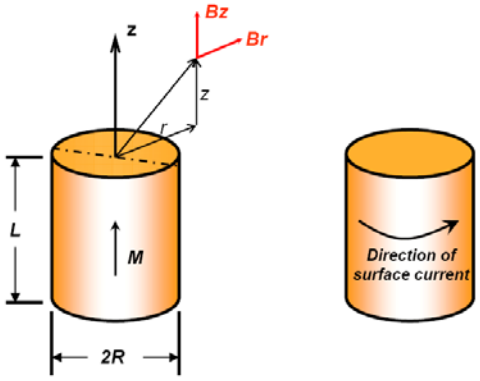

Fig. A- 2 Permanent magnet and its equivalent surface current density.

A.6 Charge Model (Magnetic Flux Calculation)

The charge model is another method for permanent magnet simulation. In this model, the magnet is expressed with a distribution of the equivalent, imaginary magnetic charges.

By using the magnetostatic field equation $\nabla \times \boldsymbol{H} = \boldsymbol{0}$, the scalar potential φ_m is

$$\boldsymbol{H} = -\nabla \varphi_{\boldsymbol{m}} . \tag{A-28}$$

By substituting (A-28) and the constitutive relation (A-5) into (A-2), the Poisson equation is

$$\nabla^2 \varphi_m = \nabla \cdot \boldsymbol{M} . \tag{A-29}$$

By using the same approach as in the current model, the solution to (A-29) is computed by

$$\varphi_m(\boldsymbol{x}) = -\frac{1}{4\pi}\int \frac{\nabla'.\boldsymbol{M}(\boldsymbol{x}')}{|\boldsymbol{x}-\boldsymbol{x}'|} d\Gamma' + \frac{1}{4\pi}\int \frac{\boldsymbol{M}(\boldsymbol{x}').\hat{\boldsymbol{n}}}{|\boldsymbol{x}-\boldsymbol{x}'|} ds' . \tag{A-30}$$

The form of (A-30) results in the following definitions:

$$\begin{aligned} \rho_m &= -\nabla \cdot \boldsymbol{M} \ (A/m^2) \quad \textit{Volume charge density}, \\ \sigma_m &= \boldsymbol{M} \cdot \hat{\boldsymbol{n}} \ (A/m) \qquad \textit{Surface charge density}. \end{aligned} \tag{A-31}$$

According to the definition of the magnetic scalar potential, the magnetic flux density is obtained as follows:

$$\boldsymbol{B}(\boldsymbol{x}) = \frac{\mu}{4\pi}\int \frac{\rho_m(\boldsymbol{x}')(\boldsymbol{x}-\boldsymbol{x}')}{|\boldsymbol{x}-\boldsymbol{x}'|^3} d\Gamma' + \frac{\mu}{4\pi}\int \frac{\sigma_m(\boldsymbol{x}')(\boldsymbol{x}-\boldsymbol{x}')}{|\boldsymbol{x}-\boldsymbol{x}'|^3} ds' . \tag{A-32}$$

The magnetic flux density, due to a permanent magnet with the magnetization of $\boldsymbol{M}$ in a space with a permeability of μ is obtained from (A-32) by first evaluating the volume and surface charge densities.

A.7 Magnetic Force Calculation

A particle of charge q is experiencing a Lorentz force, as it moves through an external magnetic field such that

$$\boldsymbol{F} = q(\boldsymbol{v} \times \boldsymbol{B}_{ext}) . \tag{A-33}$$

Consider a volume current density $\boldsymbol{J} = \rho_u \boldsymbol{v}$, where ρ_u is the charges per unit volume. The force per unit volume is expressed by

$$\boldsymbol{f} = \boldsymbol{J} \times \boldsymbol{B}_{ext}\,, \tag{A-34}$$

and so the total force on a conductor with current density $\boldsymbol{J}$ is calculated by integrating $\boldsymbol{f}$ over the conductor volume. For a thin wire, the total force is reduced to

$$\boldsymbol{F} = I \int d\boldsymbol{l} \times \boldsymbol{B}_{ext}\,. \tag{A-35}$$

To calculate the interaction force between two magnets, the Lorentz force law can be combined with the current/charge method. The interaction force of two magnets is discussed in the following sections in more detail.

A.8 Current Model (Magnetic Force Calculation)

The current model can be used to reduce the magnet to a distribution of the equivalent volume and surface current densities, as defined in(A-26). Then, the Lorentz law is employed to calculate the interaction force.

Consider the two current carrying loops in Fig. 3-2; the force that current loop 2 undergoes in the presence of current loop 1 is calculated by substituting the Biot-Savart law (A-20) into the Lorentz force law (A-35) such that

$$\boldsymbol{F}_{21} = \frac{\mu_0}{4\pi} \int_{c2} I_2 d\boldsymbol{L}_2 \times \int_{c1} \frac{I_1 d\boldsymbol{L}_1 \times \boldsymbol{R}_{21}}{R_{21}^3}\,. \tag{A-36}$$

This equation is also called Ampere's force law. $\boldsymbol{R}$ is the distance vector between the two elements. The right integral is the magnetic flux density, produced by current-carrying conductor 1 at the location of element 2.

The following geometry vectors are obtained from Fig. 3-2:

$$\begin{aligned}
&\boldsymbol{R}_{21} = (-R_1 \cos\theta_1 + R_2 \cos\theta_2)\hat{\boldsymbol{i}} + (-R_1 \sin\theta_1 + R_2 \sin\theta_2)\hat{\boldsymbol{j}} + z_d \hat{\boldsymbol{k}}\,,\\
&R_{21} = \sqrt{R_2^2 + R_1^2 - 2R_1 R_2 \cos(\theta_2 - \theta_1) + {z_d}^2}\,,\\
&d\boldsymbol{L}_k = R_k d\theta_k \hat{\boldsymbol{\theta}} = -R_k \sin\theta_k d\theta_k \hat{\boldsymbol{i}} + R_k \cos\theta_k d\theta_k \hat{\boldsymbol{j}}. \quad (k = 1, 2)
\end{aligned} \tag{A-37}$$

By substituting (A-37) into(A-36), the vertical component of the interaction force between the two current-carrying loops with the opposite current direction is reduced to

$$F_z(z_d) = \frac{\mu_0 I_1 I_2 R^2}{4\pi} \int_0^{2\pi} \int_0^{2\pi} \frac{-z_d \cos(\theta_2 - \theta_1)\, d\theta_1\, d\theta_2}{(2R^2 - 2R^2 \cos(\theta_2 - \theta_1) + z_d^2)^{3/2}}, \tag{A-38}$$

where z_d is the distance between the two loops. By using the same current method as that for the permanent magnet modeling, the vertical component of the interaction force between two adjacent magnets with the opposite magnetization direction is obtained by integrating (A-38) along the magnet lengths as follows:

$$F_z = \frac{\mu_0 I_1 I_2 R^2}{4\pi L^2} \int_{g/2}^{g/2+L} \int_{-L-g/2}^{-g/2} \int_0^{2\pi} \int_0^{2\pi} \frac{-\left[z_d - z' - z''\right] \cos(\theta_2 - \theta_1)\, d\theta_1\, d\theta_2 dz' dz''}{(2R^2 - 2R^2 \cos(\theta_2 - \theta_1) + \left[z_d - z' - z''\right]^2)^{3/2}}. \tag{A-39}$$

A.9 Charge Model (Magnetic Force Calculation)

The charge model can be used for calculating the force on a magnet in an external field. The force expression is obtained from the following equation:

$$\boldsymbol{F} = \int_{\Gamma} \rho_m \boldsymbol{B}_{ext} d\Gamma + \int_S \sigma_m \boldsymbol{B}_{ext} ds\,. \tag{A-40}$$

The volume and surface charge densities should be evaluated, given a magnet with magnetization ***M***, and substituted into (A-40) to determine the acting force on a magnet.

Consider two thin cylindrical magnets ($R << L$), as shown in Fig. A- 3.

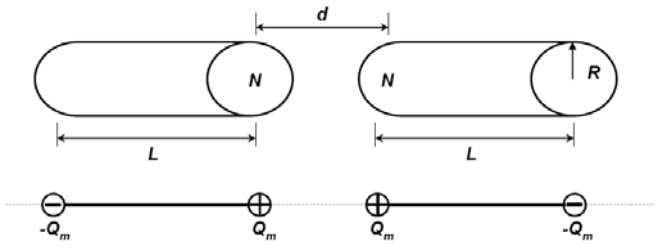

Fig. A- 3 Two cylindrical magnets and equivalent charge model.

The charge at the endings is given by

$$Q_m = \sigma_m \Delta \boldsymbol{A} = \pm M_s \pi R^2 .$$

The force between two discrete point charges $Q_m(x_1)$ at x_1 and $Q_m(x_2)$ at x_2 is obtained by substituting (A-32) into (A-40) as follows:

$$\boldsymbol{F}_{12} = \frac{\mu_0}{4\pi} \frac{Q_m(\boldsymbol{x}_1) Q_m(\boldsymbol{x}_2)(\boldsymbol{x}_1 - \boldsymbol{x}_2)}{\left|\boldsymbol{x}_1 - \boldsymbol{x}_2\right|^3} . \tag{A-41}$$

Therefore, the force acting on the magnets is

$$F(d) = \frac{\mu_0 Q_m^2}{4\pi} \left\{ \frac{1}{d^2} - \frac{2}{(L+d)^2} + \frac{1}{(2L+d)^2} \right\}. \tag{A-42}$$

A.10 Magnetic Circuit Analysis

A magnetic circuit is a closed path of magnetic flux, and contains ferromagnetic materials and field sources such as permanent magnets and coils. The basis of magnetic circuit analysis is based on (A-8) and (A-10). Consider a circuit with *m* segments with different permeabilities; Ampere's law is reduced to

$$\oint \boldsymbol{H} \cdot d\boldsymbol{l} = \sum_{i=1}^{m} H_i l_i = nI \tag{A-43}$$

or

$$\sum_{i=1}^{m} \Re_i \Phi_i = \sum_{k=1}^{N} \mathfrak{M}(k) , \tag{A-44}$$

where $\Re_i = l_i / \mu_i A_i$ is the reluctance of the i^{th} element, A_i is the cross-section area of element, Φ_i is magnetic flux in the element, and $\mathfrak{M}(k)$ is known as the magnetomotive force (mmf) for the k^{th} source (when there are *N* sources). $\mathfrak{M} = ni$ for a *n*-turn coil, and $\mathfrak{M} = H_c l_m$ for a magnet with length l_m and coercivity H_c. The second equation is obtained from (A-10), and states that the algebraic sum of the magnetic flux, flowing into a circuit node is zero such that

$$\int \boldsymbol{B} \cdot d\boldsymbol{s} = 0 \Rightarrow \sum_i \Phi_i = 0 \,. \tag{A-45}$$

Permanent magnets are also used as sources in circuits, but they are different from current sources: the mmf force of magnets is not known a priori, unlike the mmf for the current sources, and is a function of the circuit itself. Fig. A- 4 shows a magnetic circuit, including a permanent magnet, an air-gap, and an iron core. The iron-core permeability is assumed infinite, regarding its high relative permeability.

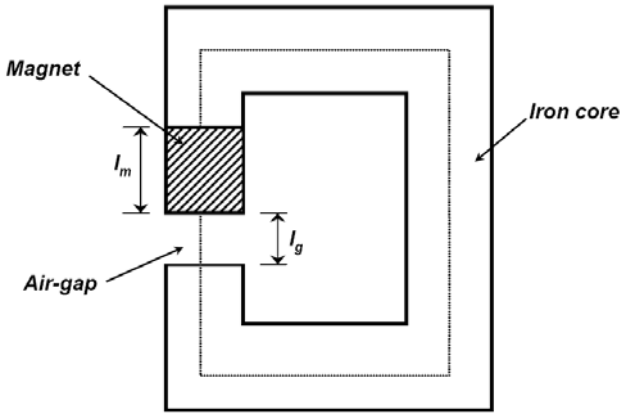

Fig. A- 4 A magnetic circuit including a permanent magnet.

By applying (A-43) to a path around the circuit,

$$H_g l_g + H_m l_m = 0 \,, \tag{A-46}$$

where H_m and H_l are fields in the magnet and gap, respectively. (A-46) is modified in terms of magnetic flux density in the gap, therefore,

$$\left(\frac{B_g}{\mu_0}\right) l_g + H_m l_m = 0 \,. \tag{A-47}$$

By considering (A-45), it is concluded that B_g equals B_m (neglecting the flux leakage), and (A-47) becomes a linear equation in respect to B_m and H_m, defining the load-line. The intersection of this

line with the characteristic *B-H* curve of the permanent magnet provides the operating point of the permanent magnet, as shown in Fig. A- 5.

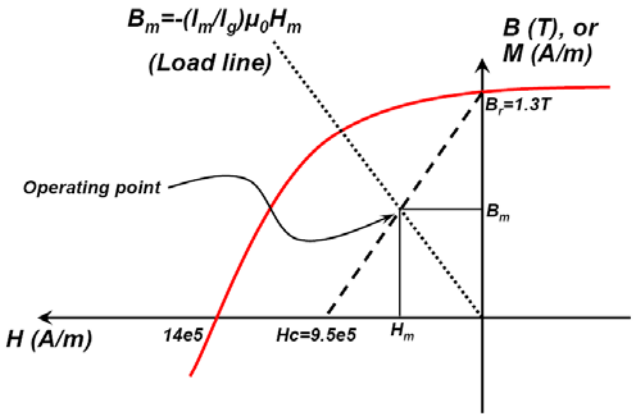

Fig. A- 5 Determination of the operating point for a permanent magnet.

The equation for the rectilinear demagnetization characteristic of a typical permanent magnet (dashed-line in Fig. A- 5) is

$$B_m = B_r + \mu_{rec} H_m , \tag{A-48}$$

where $\mu_{rec} = B_r / H_c$. This equation is modified by calculating

$$H_m = \frac{B_m}{\mu_{rec}} - H_c . \tag{A-49}$$

The intersection of the characteristic equation (A-49) with the load-line equation (A-46) results in

$$H_g l_g + \frac{B_m}{\mu_{rec}} l_m = H_c l_m \tag{A-50}$$

or

$$\Phi(\Re_g + \Re_m) = H_c l_m . \tag{A-51}$$

(A-51) is a simplification of (A-44) for the magnetic circuit in Fig. A- 4. (A-51) is used to evaluate the length of permanent magnet l_m as a function of air-gap length l_g and air-gap flux density B_g.

$$l_m = \frac{B_g B_r}{\mu_0 H_c (B_r - B_g)} l_g . \tag{A-52}$$

Appendix B

Damper Modeling

B.1 A Bi-linear Model for the Solenoid-Valve Damper

A simple bi-linear model can be fitted to the data obtained from the Volvo S60 solenoid-valve damper to achieve an experimental non-parametric model of the damper. By assuming

$$F = c_1 v + c_2 , \tag{B-1}$$

for either extension or compression, and the coefficients c_1 and c_2 are defined as

$$\begin{aligned} c_1 &= a_{11} V + a_{12} \\ c_2 &= a_{21} V + a_{22} , \end{aligned} \tag{B-2}$$

where v and V are the velocity and voltage, respectively. The least square method is used to obtain the coefficients, which are listed in Table B- 1.

Table B- 1: Bi-linear model coefficients.

	Voltage	Velocity (m/s)	a_{11}	a_{12}	a_{21}	a_{22}
Extension	$1 < V < 5$	$0.1 < v < 0.8$	127	-	68	-
Compressi	$1 < V < 5$	$-0.8 < v < -0.$	104	-	-	-

B.2 A Bi-quadratic Model for the MR Dampers

For the tested MR dampers, a bi-quadratic model is used to obtain the non-parametric, experimental model of the dampers. By assuming the force-velocity relationship is

$$F = c_1 v^2 + c_2 v + c_3 , \tag{B-3}$$

where,

$$c_i = a_{i1} I^2 + a_{i2} I + a_{i3} , \tag{B-4}$$

and I is the current applied to the damper. The bi-quadratic models coefficients are given in Table B-2.

Table B- 2 Bi-quadratic model coefficients.

$0(A) \le I \le 3.5(A)$		a_{11}	a_{12}	a_{13}	a_{21}	a_{22}	a_{23}	a_{31}	a_{32}	a_{33}
Front	Compression $-1 \le v \le -0.05$	-5178.1	14146	776.1	-1518.7	6578	189.6	-33.2	75.4	-248.8
	Extension $0.05 \le v \le 1$	5453	-14387	-449.7	-1580.9	6665.8	26.3	32.9	-93.8	90.6
Rear	Compression $-1 \le v \le -0.05$	-5180.6	13428	4413.5	-1477.2	6045.8	1198.3	-39.3	98.1	-320.6
	Extension $0.05 \le v \le 1$	4654.5	-11504	1219.8	-1388.5	5694.6	117.8	31	-88.3	137

Appendix C

Design Requirements

C.1 Passive Damper

General design requirements for a passive damper in a midsize car are listed in Table C- 1.

Table C- 1 Passive damper design parameters.

Quantity	Value
Peak passive force	2000 N
RMS force	1040 N
Passive damping coefficient	1500-2000 Ns/m
Max. weight	4 kg
Max. diameter	150 mm
Max. Length	600 mm
Stroke	160 mm

C.2 Active Damper

General design requirements for an active damper in a midsize car are listed in Table C- 2.

Table C- 2 Active damper design parameters.

Quantity	Value
Peak active force	1300 N
Max. power consumption	500 W (Each unit)
Max. weight	7 kg
Max. diameter	150 mm
Max. Length	600 mm
Stroke	160 mm

C.3 Hybrid Damper

General design requirements for a hybrid damper in a midsize car are listed in Table C- 3.

Table C- 3 Hybrid damper design parameters.

Quantity	Value
Peak active force	350 N
Peak passive force	1650 N
Passive damping coefficient	1400 Ns/m
Max. power consumption	500 W (Each unit)
Max. weight	7 kg
Max. diameter	150 mm
Max. Length	600 mm
Stroke	160 mm

Bibliography

Ahmadian M., Vahdati N., Transient dynamics of semi-active suspensions with hybrid control, *Journal of Intelligent Material Systems and Structures*, 17(2), (2006) 145–153.

Alanoly J., Sankar S., A new concept in semi-active vibration isolation, *ASME Design Engineering Technical Conference*, t86-DET-28 (1986).

Allen J. A., Design of active suspension control based upon use of tubular linear motor and quarter-car model, Msc. Thesis, *Texas A&M University*, August 2008.

Anderson E., Evert M., Gleese R., Gooding J., Pendleton S., Satellite ultra-quite technology experiment (SUIT): Electromechanical subsystems, *SPIE Conference on Industrial and Commercial Applications of Smart Structures Technologies*, 3674, (1999) 308-328.

Anon B., Mechanical vibration and shock-evaluation of human exposure to whole-body vibration, *International Organization for Standardization*, 1997, ISO 2631.

Arof H., Eid A., Nor K. M., Permanent magnet linear generator design using finite element method, *International Conference on Electrical, Electronic and Computer Engineering, ICEEC'04*, (2004) 893-896.

Arsem H. B., Electric shock absorber, *US. Patent Number 3559027* (1971).

Aspinall D. T., Oliver R. J., Vehicle riding comfort: the correlation between subjective assessments of vehicle ride and physical measurements of vehicle motion, *Motor Industry Research Association report* 1964/10.

Bae J.S., Kwak M. K., Inman D. J., Vibration suppression of cantilever beam using eddy current damper, *Journal of Sound and Vibration*, 284, (2005) 805-824.

Barak P., Passive versus active and semi-active suspension from theory to application in north American industry, *SAE Technical Paper* 922140, 1992.

Bernard, J., Shannan, J., Vanderploeg, M., Vehicle rollover on smooth surface, *SAE Technical Paper Series*, 891991, (1991).

Bianchi N., Bolognani S., Corte D. D., Tonel F., Tubular linear permanent magnet motors: An overall comparison, *IEEE Transactions on Industry Applications*, (39) 2, (2003) 466-475.

Bianchi N., Bolohnani S., Tonel F., Design criteria of a tubular linear IPM motor, *IEMDC 2001*, *IEEE International Electric Machines and Drives Conference* (Cat. No.01EX485), (2001) 1-7.

Biglarbegian M., Melek W., Golnaraghi F., A novel neuro-fuzzy controller to enhance the performance of vehicle semi-active suspension systems, *Vehicle System Dynamics*, 46(8), 2008 691–711.

Brown S., Vehicle Suspension, *US Patent Number* 6945541, (2005).

Cadwell L. H., Magnetic damping analysis of an eddy current brake using an air-track, *American Journal of Physics*, 64 (1996) 917-923.

Canova A., Vusini B., Design of axial eddy current couplers, *IEEE Transactions on Industry Applications*, 39(3), (2003) 725-733.

Carter A. K., Transient motion control of passive and semi-active damping for vehicle suspensions, *Masters Thesis*, *Virginia Tech.*, July1998.

Cengel Y., Turner R., Fundamentals of Thermal-Fluid Sciences, Second Edition, *McGraw-Hill*, 2005.

Chang S. L., Design of an active suspension with a controllable damper, *PhD Thesis, Northwestern University*, June 1998.

Craik D., Magnetism, principles and applications, *John Wiley and Sons*, West Sussex, (1995) 334-336.

Crosby, M. and Karnopp, D. C., The active damper- a new concept for shock and vibration control, *Shock and Vibration. Bulletin, Part H*, Washington, D. C. (1973).

Demic M., Lukic J., Milic Z., Some aspect of the investigation of random vibration influence on ride comfort, *Journal of Sound and Vibration*, 253(1), (2002) 109–129.

Deo H. V, Axiomatic design of customizable automotive suspension systems, *PhD. Thesis*, *Massachusetts Institute of Technology*, February 2007.

Elbuken C., Khamesee M. B., Yavuz M., Eddy current damping for magnetic levitation: downscaling from macro to micro-levitation, *Journal of Physics, D: Applied Physics,* 39 (2006) 3932-3938.

Elbuken C., Shameli E., Khamesee M. B., Modelling and analysis of eddy-current damping for high-precision magnetic levitation of a small magnet, *IEEE Transaction on Magnets*, 43(1), January 2007, 26-32.

Eslaminasab N., Development of a semi-active intelligent suspension system for heavy vehicles, *PhD. Thesis, University of Waterloo*, 2008.

Eslaminasab N., Golnaraghi F., The effect of time delay of the semi-active dampers on the performance of on-off control schemes, *Proceedings of ASME International Mechanical Engineering Congress and Exposition, IMECE2007*, Seattle, USA, November 2007.

Forbes L. K., Cozier S., Doddrell D. M., Rapid calculation of static fields produced by thick circular solenoids, *IEEE Transactions on Magnetics*, 33(5), (1997) 4405-4410.

Foshage, J., Davis, T., Sullivan, J., Hoffman, T., Das, A., Hybrid active/passive actuator for spacecraft vibration isolation and suppression, *Proceedings of SPIE on Actuator Technology and Application Conference*, 1996.

Furlani E. P., Permanent magnet and electromechanical devices, materials, analysis and applications, *Academic Press*, San Diego, (2001) 126-130.

Genta G., Delprete C., Tonoli A., Rava E., Mazzocchetti L., Analytical and experimental investigation of a magnetic radial passive damper, *Proceedings of the Third International Symposium of Magnetic Bearings*, Washington D.C., July 1992, 255-264.

Gillespie T., Development of semi-active damper for heavy off-road military vehicles, *M.Sc. Thesis, University of Waterloo*, 2006.

Goldner R. B., Zerigan P., Electromagnetic linear generator and shock absorber, *US. Patent Number 6952060* (2005).

Graves K. E., Toncich D., Iovenitti P.G., Theoretical comparison of motional and transformer EMF device damping efficiency, *Journal of Sound and Vibration,* 233, (2000) 441-453.

Griffin M. J., A comparison of standardized methods for predicting the hazards of whole-body vibration and repeated shocks, *Journal of sound and vibration*, 215 (4) (1998) 883-914.

Gupta A., Jendrzejczyk J. A., Mulcahy T. M., Hull J. R., Design of electromagnetic shock absorbers, *International Journal of Mechanics and Materials in Design*, 3(3), (2007) 285-291.

Hadley N. F., Shock absorber characteristics, *SAE Journal*, 22, Paper No. S356, (1928), 356-362.

Hagela K. H., Engelsdorf K., Mettner M., Panther M., Tran Q. N., Rubel E., Continuously adjustable shock absorbers for rapid acting ride control systems, *Proceedings of SAE, 18th FISITA Congress*, (1990) 37-46.

Hahn K. D., Johnson E. M., Brokken A., Baldwin S., Eddy current of a magnet moving through a pipe, *American Journal of Physics*, 66 (12), (1998) 1066-1076.

Heald M. A., Magnetic braking: improved theory, *American Journal of Physics,* 56(6), (1996) 521-522.

Hrovat D., Applications of optimal control to advanced automotive suspension design, *Journal of Dynamic System, Measurement, and Control*, 115, (1993) 328-342.

Hrovat, D., Survey of Advanced Suspension Development and Related Optimal Control Applications, *Automatica*, 33(10), (1997) 1781-1817.

Hu W., Wereley N. M., Hybrid magnetorheological fluid–elastomeric lag dampers for helicopter stability augmentation, *Smart Material and Structures*, 17(4), (2008) 045021.

Ihsan S. I., Faris W. F., Ahmadian M., Analysis of control policies and dynamic response of a Q-car 2-DOF semi active system, *Shock and Vibration,* 15(5), (2008) 573–582.

Ikhouane F., Vibration of the hysteresis loop with the Bouc-Wen model parameters, *Nonlinear Dynamics*, 48(4), (2007) 361-380.

James W. S., Ullery F. E., An automatic shock absorber, *SAE Trans., Society of Automotive Engineers, Warrendale, Pa*, 30(5) (1932) 185-191.

Karnopp D., Active and semi-active vibration isolation, *Journal of Mechanical Design*, *Transactions of the ASME*, 117B, (1995) 177-185.

Karnopp D., Active and semi-active vibration isolation, *Journal of Vibration and Acoustics*, 117(3B) (1995) 177-185.

Karnopp D., Active damping in road vehicle suspension systems, *Vehicle System Dynamics*, 12, (1983) 291-316.

Karnopp D., Crosby M. J., Harwood R. A., Vibration control using semi-active force generators, *Transaction of ASME, Journal of Engineering for Industry*, 96, (1974) 619-626.

Karnopp D., Design principles for vibration control system using semi-active damper, *ASME Journal of Dynamic Systems, Measurement, and Control*, 112, (1990) 448-455.

Karnopp D., Permanent magnet linear motors used as vehicle mechanical dampers for vehicle suspensions*, Journal of Vehicle System Dynamics*, 18, (1989) 187-200.

Karnopp, D., Trikha, A. K., Comparative study of optimization techniques for shock and vibration isolation, *Transaction of ASME, Journal of Engineering for Industry*, 91(4), (1969) 1128-1132.

Kendall J., Michelin re-invents the wheel, *Automotive Engineering International, SAE*, November 2008, P. 35.

Konotchick J. A., Linear motion electric power generator, *US. Patent Number 5347186* (1994).

Koo J. H., Ahmadian M., Setareh M., Experimental evaluation of Magneto-Rheological dampers for semi-active tuned vibration absorbers, *Smart Structures and Materials, Proceedings of SPIE,* 5052, 83-91.

Koo J. H., Goncalves F. D., Ahmadian M., Investigation of the response time of Magneto-Rheological fluid dampers, *Proceedings of SPIE 2004, Smart Structures and Materials/NDE, San Diego, CA*, March 2004.

Koo J.H., Goncalves F.D., Ahmadian M., A comprehensive analysis of the response time of MR dampers, *Smart Materials and Structures*, (15) 2, (2006) 351-358.

Kruckemeyer W. C., Buchanan H. C., Fannin W. V., Rotational actuator for vehicle suspension damper, *US Patent Number 4644200* (1987).

Kyongsu, Y., Jangyeol, Y., Dongshin, K., Model-based estimation of vehicle roll state for detection of impending vehicle rollover, *Proceedings of the 2007 American Control Conference, ACC 2007*, 1624-1629.

Lane R., Charles N. M., Methods for eliminating jerk and noise in semi-active suspensions, Total vehicle Ride, Handling and Advanced Suspensions, *Warrendale, PA: Society of Automotive Engineers*, 1990.

Lee C., Jee W., H∞ robust control of flexible beam vibration by using a hybrid damper, *Journal of dynamic systems, measurement, and control*, 118(3), (1996) 643 -648.

Lee K., Park K., Modelling eddy currents with boundary conditions by using Coulombs law and the method of images, *IEEE Transactions on Magnetics*, 38(2), (2002) 1333-1340.

Lee S., Park E. C. Min, K. Lee S. Chung L. Park J., Real-time hybrid shaking table testing method for the performance evaluation of a tuned liquid damper, *Journal of Sound and Vibration*, 302(3), (2007) 596 -612.

Levy B. S., Wegman D. H., Baron S. L., Sokas R. K., Occupational and environmental health: recognizing and preventing disease and injury, *Lippincott Williams and Wilkins*, 2005.

Li H., Goodall R. M., Linear and non-linear skyhook damping control laws for active railway suspensions, *Control Engineering Practice*, 7(7), (1999) 843-850.

Lin P. Y., Roschke P. N., Loh C. H., Hybrid base-isolation with magnetorheological damper and fuzzy control, *Structural Control and Health Monitoring*, 14(3), (2007) 384-405.

Lu H., J Zhu, Y. Guo, Development of a slotless tubular linear interior permanent magnet micro-motor for robotic applications, *IEEE Transactions on Magnets*, 41(10), (2005) 3988-3990.

MacLatchy C. S., Backman P., Bogan L., A quantitative magnetic braking experiment, *American Journal of Physics*, 61(12), (1993) 1096-1101.

Majumdar S. R., Oil hydraulic systems, principles and maintenance, *Mc Graw-Hill Professional*, 2001.

Margolis D. L., Tylee J. L., Hrovat D., Heave mode dynamics of a tracked air cushion vehicle with semi-active airbag secondary suspension, *ASME Journal of Dynamic Systems, Measurement, and Control*, 97(4), (1975) 399-407.

Martins I., Esteves J., da Silva F. P., Verdelho P., Electromagnetic hybrid active-passive vehicle suspension system, *IEEE Vehicular Technology Conference*, 3, (1999) 2273-2277.

Martins I., Esteves J., Marques G. D., da Silva F. P., Permanent-magnets linear actuators applicability in automobile active suspensions, *IEEE Transactions on Vehicular Technology*, 55(1), January 2006.

Merritt T. D., Pasichinskyj M. J., Linear reciprocating electrical generator, *US. Patent Number 4500827* (1985).

Milliken W. F., Active Suspension, *SAE Technical Paper No. 880799*, *Warrendale, PA: Society of Automotive Engineers*, 1988.

Mitschke M., Influence of road and vehicle dimensions on the amplitude of body motions and dynamic wheel loads, *SAE, Preprint* 310C, 1961.

Mizuno T., Iwadare M., Nanahara M., Koyama K., Anzai T., Nirei M., Yamada H., Considerations on electrical and mechanical time constants of a moving-magnet-type linear DC motor, *Sensors and Actuators,* 81, (2000) 301-304.

Moore J. J. Palazzolo A. B. Gadangi R. K. Kascak A. F. Brown G. Montague G., Hybrid friction-impact vibration damper for cryogenic rotating machinery, *Journal of propulsion and power*, 13(4), (1997), 495 -501.

Murty B. V., Electric variable damping vehicle suspension, *US. Patent Nnumber 4815575* (1989).

Nagaya K., Sugiura M., A method for obtaining a linear spring for a permanent magnet levitation system using electromagnetic control, *IEEE Transactions on Magnetics*, 13(3) (1995) 2332-2338.

Nor K. M., Arof H., Wijono, Design of a 5 kW tubular permanent magnet linear generator, *39th International Universities Power Engineering Conference, UPEC 2004*, (2004) 528-532.

Patt P. J., Design and testing of a coaxial linear magnetic spring with integral linear motor, *IEEE Transactions on Magnetics*, 21(5), (1985) 1759-1761.

Polak P., Burton R. T., Improving suspension damping, Journal of Automotive Engineering, Feb.1971, 13-17.

Pollard M. G., Active suspensions enhance ride quality, *Railway Gazzette International*, 139, (1983) 850-853.

Pollard M. G., Simons N. J. A., Passenger comfort - the role of active suspensions, *Proceedings of the Institution of Mechanical Engineers, Part D*, 198 (11), (1984), 161-175.

Preumont A. Vibration control of active structures, *Kluwer Academic Publishers Dordrecht*, e-Book ISBN: 0-306-48422-6, (2002).

Prokop G., Sharp R. S., Performance enhancemet of limited-bandwith active automotive suspensions by road preview, *IEEE Proceedings-Control Theory and Applications*, 142, (1995) 140-148.

Rakheja S., Sankar S., Vibration and shock isolation performance of a semi-active 'on-off' damper, *Journal of Vibration, Acoustics, Stress, and Reliability in Design*, 107(4), (1985) 398-403.

Rakheja S., Su H., Sankar T. S., Analysis of a passive sequential hydraulic damper for vehicle suspension, *Vehicle System Dynamics*, 19(5), (1990) 289-312.

Rhinefrank K., Agamloh E. B., Jouanne A., Wallace A., Prudell J., Kimble K., Aills J., Shmidt E., Chan P., Sweeny B., Schacher A., Novel ocean energy permanent magnet linear generator buoy, *Renewable Energy*, 31 (2006) 1279-1298.

Ryba D., Improvement in dynamic characteristics of automobile suspension systems (Part I. Two-mass systems), *Vehicle System Dynamics*, 3(1), (1974) 17-45.

Schmid M., Varga P., Analysis of vibration-isolating systems for scanning tunneling microscopes, *Ultramicroscopy*, 42-44, Part B (1992) 1610-1615.

Segal L., Xio-Peo L., Vehicular resistance to motion as influenced by road roughness, *Australian Road Research*, 12 (4) (1982), 211-222.

Sharp R. S., Crolla D. A., Road vehicle suspension system design - a review, *Vehicle System Dynamics*, 16, (1987) 167-192.

Sharp R. S., Hassan S. A, The relative performance capabilities of passive, active and semi-active car suspension systems, *Proceedings of the Institution of Mechanical Engineers, Part D*, 200(3), (1986) 219-228.

Sharp R. S., Hassan S. A., The fundamentals of passive automotive suspension system design, *Society of Environmental Engineers Conference on Dynamics in Automotive Engineering*, 1984, 104-1 15.

Shen. Y, Vehicle suspension vibration control with magnetorheological dampers, *PhD. Thesis, University of Waterloo*, 2005.

Sodano H., Bae J. S., Inman D. J., Belvin W. K., Concept and model of Eddy current damper for vibration suppression of a beam, *Journal of Sound and Vibration* 288, (2005) 1177-1196.

Sodano H., Bae J. S., Inman D. J., Belvin W. K., Improved Concept and Model of Eddy Current Damper, *Transaction of the ASME*, 128, June 2006, pp. 294-302.

Suda Y., Nakadai S., Nakano K., Study on the self powered active vibration control, *Fourth International Conference on Motion and Vibration Control* (1998) 91-96.

Suda Y., Shiiba T., A new hybrid suspension system with active control and energy regeneration, *Vehicle System Dynamics*, supplement 25, (1996) 641-654.

Suda Y., Shiiba T., Hio K., Kawamoto Y., Condo T., Yamagata H., Study on electromagnetic damper for automobiles with nonlinear damping force characteristics, *Vehicle System Dynamics*, supplement 41, (2004) 637-646.

Teshima H., Tanaka M., Miyamoto K., Nohguchi K., Hinata K., Effect of eddy current dampers on the vibration properties in superconducting levitation using melt-processed YbaCuO bulk superconductors, *Physics C*., 274, (1997) 17-23.

Thompson A. G., Optimum damping in a randomly excited non-linear suspension, *Proceedings of the Institution of Mechanical Engineers*, 184(2A), (1969) 169- 178.

Tonoli A., Dynamic Characteristics of eddy current dampers and couplers, *Journal of Sound and Vibration,* 301 (3-5), (2007) 576-591.

Vahid O., Experimental investigation of a variable damper, *Mechworks System Inc*. Document file number: 060115-1, January 2006.

Vailon, L., Petitjean, B., Frapard, B., Lebihan, D., Active isolation in space truss structures: from concept to implementation, *Smart Materials and Structures*, 8(6), (1999) 781—790.

Wang J., Howe D., Jewell G. W., Analysis and design optimization of an improved axially magnetized tubular permanent-magnet machine, *IEEE Transactions on Energy Conversion*, vol. 19 (2), June 2004.

Watakabe M., Tohdo M., Chiba O., Izumi N., Ebisawa H., Fujita T., Response control performance of a hybrid mass damper applied to a tall building, *Earthquake engineering & structural dynamics*, 30(11), (2001) 1655 -1676.

Weaver E. W., Measure of shock absorber performance, *Automotive Industry*, (1929) 870-972.

Web1, http://www.carbibles.com/suspension_bible_pg2.html, April, 2009.

Web2, http://delphi.com/manufacturers/auto/other/ride/magneride/, April, 2009.

Wen Y. K., Asce M., Method of random vibration of hysteretic system, *Journal of Engineering Mechanics Division, ASCE*, 102(2), (1976) 249-263.

Wendel G. R., Stecklein G. L., A regenerative active suspension system, *SAE Technical Paper Series*, 910659 (1991) 129-135.

Wheeler, H. A., Formulas for the skin effect, *Proceedings of the Institute of Radio Engineers*, 30(9), (1942), 412-424.

White F. M., Fluid Mechanics, *Fifth Edition, WCB McGraw Hill*, 2003.

Wiederick H. D., Gautheir N., Campbell D. A., Rochon P., Magnetic Braking: Simple Theory and Experiment, *American Journal of Physics*, 55 (6), (1987) 500-503.

Yabuta K., Hidaka K., Fukushima N., Influence of suspension friction on riding comfort, *Proceedings of 7th IAVSD Symposium on the Dynamics of Vehicles on Roads and on Railway Tracks, Cambridge UK*, 1981, 181-193.

Yajima H., Wakiwaka H., Minegishi K., Fujiwara N., Tamura K., Design of linear DC motor for high-speed positioning, Sensors and Actuators, 81 (2000) 281-284.

Yau H. T., Chen C., Electric-hydraulic actuator design for a hybrid squeeze-film damper-mounted rigid rotor system with active control, Journal of vibration and acoustics, 128(2), (2006) 176 -83.